
Search for supersymmetry in pp collisions with
all-hadronic final states using the α_T variable with
the CMS detector at the LHC

Bryn Lugh Shorney-Mathias

High Energy Physics
Blackett Laboratory
Imperial College London

Thesis submitted to Imperial College London
for the degree of Doctor of Philosophy and the Diploma of Imperial College

SPRING 2013

Abstract

A search for supersymmetry in the exclusive hadronic and missing energy channel is presented on 5 fb^{-1} of data collected using the CMS detector at the LHC. The data were produced at a center-of-mass energy of 7 TeV. The kinematic discriminator α_T is used to select signal events which are then binned in terms of the visible energy per event. The efficiency of the hadronic Level-1 triggers is measured though-out the data taking period and a scheme to reduce the effects of multiple collisions per bunch crossing on the cross section of the trigger paths is studied, implemented and tested in situ. These efficiency measurements are considered in the development of an analysis specific trigger, the performance of which is measured in situ, with the final efficiencies taken into account in the presented analysis. A data driven background estimation method is used to predict the expected yield in the signal regions from Standard Model processes. In the absence of an observed excess, limits are set to the 95% confidence level on the production cross section and masses of new particles. In the context of the Constrained Minimal Supersymmetric Model (CMSSM), squarks and gluinos with a mass of up to 1 TeV are excluded. In terms of simplified models with various light and heavy flavour final states, squarks and gluinos are excluded at a mass of $\approx 1 \text{ TeV}$ for a Lightest Supersymmetric Particle (LSP) mass of up to $\approx 500 \text{ GeV}$. Natural units ($\hbar = c = 1$) are used though-out.

Declaration

This thesis presents work from an official CMS supersymmetry search as well as the measurement of the performance of the Level-1 trigger system, performed from 2010 to 2012. The work presented in Chapters 4, 5 and 7.3 is mine unless otherwise referenced and was carried out within the context of the Imperial College London and CERN SUSY groups as a subsection of the greater CMS collaboration. Contributions from others are referenced throughout.

- Bryn Lugh Shorney-Mathias, March 2013

Preface

To see a World in a Grain of Sand
And a Heaven in a Wild Flower,
Hold Infinity in the palm of your hand
And Eternity in an hour.

- William Blake.

Acknowledgements

So the journey is coming to an end, working at CERN, analysing some of the first data produced at the LHC and recorded with the CMS detector and leaving a mark no matter how small on the scientific world is certainly the fulfilment of an ambition. However I could not have done this alone and so I would like to thank: Robert Bainbridge and Henning Flaecher for their help and direction, Alex Tapper for his guidance, supervision and finding me interesting things to work on.

I have to thank my contemporaries and friends, Martyn Jarvis, Nick Wardle, Sam Rogerson, Alex Shires, Chris Parkinson, Arlo Bryer and Alex Sparrow for many long and in-depth discussions, some of them were even relevant. The entire of the RA1 team, Edward Laird, Markus Stoye, Tanja Rommerskirchen, Burt Betchart, Darren Burton, Chris Lucas, Oliver Buchmuller and Paris Sphicas.

Lucie Gauthier, Alex Mott, Massimiliano Chiorboli and Roberto Rossin for their help and guidance with all things HLT. Jim Brooke and Greg Iles for their expertise with the Level-1 trigger.

Finally a large thanks have to go to my family for continued support and encouragement throughout, also to all of my previous teachers over the years for keeping me on the right track.

Contents

1. Introduction	10
2. Theoretical Overview	14
2.1. The Standard Model (SM)	16
2.1.1. Gauge Invariance	17
2.1.2. Electroweak symmetry and interactions	18
2.1.3. Quantum Chromo Dynamics	19
2.1.4. The Higgs and Electroweak Symmetry Breaking	19
2.2. Beyond the Standard Model.	20
2.2.1. The Constrained Minimal Super Symmetric Model	22
2.2.2. Simplified Models	23
2.3. SUSY Searches at the LHC	25
2.3.1. Parton Density Functions of the Proton	25
2.3.2. Hadronization Models	26
3. The CMS detector	27
3.1. The Silicon Tracker	28
3.2. The Electromagnetic Calorimeter (ECAL)	29
3.3. The Hadronic Calorimeter (HCAL)	30
3.4. The Superconducting Solenoid	32
3.5. The Muon system	32
3.6. The Level-1 Trigger System	33
3.7. The High Level Trigger System	34
4. Level-1 Calorimeter Trigger	35
4.1. Level-1 Trigger Jet Algorithm	36
4.2. Level-1 Trigger Performance	39
4.3. Level-1 Trigger Pile-up Mitigation	44
4.3.1. Effect on trigger efficiency	49

4.3.2. Efficiency of H_T Triggers	49
4.3.3. Efficiency of Jet Triggers	49
4.3.4. Efficiency of MultiJet Triggers	50
4.4. Summary	51
5. Reconstruction and Event selection	52
5.1. Event selection	52
5.1.1. Preselection of hadronic objects	53
5.1.2. Electrons	54
5.1.3. Muons	55
5.1.4. Photons	55
5.1.5. Resolving object overlaps	57
5.2. The α_T variable	57
5.3. Common Analysis cuts	59
5.4. High Level Triggers for the α_T analysis	62
5.4.1. Trigger efficiency measurement	63
5.5. Including B-tagging in the α_T analysis.	66
6. Background Prediction	72
6.1. Electroweak Background Prediction	73
6.1.1. The $\mu + \text{Jets}$ control sample	76
6.1.2. The $\mu\mu + \text{Jets}$ control sample	77
6.1.3. The $\gamma + \text{Jets}$ control sample	77
6.1.4. Muon control samples without an α_T cut	78
6.2. Systematic uncertainties on the Electroweak background model	81
6.3. Systematic errors and biases on the translation factors	83
6.4. Estimating the residual QCD background component.	83
6.5. Likelihood model	86
6.5.1. Signal Contamination	90
6.5.2. The total likelihood	90
6.6. Final Results	91
7. Interpretation	96
7.1. Signal Models	96
7.2. Signal Efficiency	97
7.2.1. Constrained Minimal SuperSymmetric Model (CMSSM)	97
7.2.2. Simplified Models	97

7.2.3. Signal Efficiency for the Background Selection	98
7.3. Uncertainty on Signal Efficiency	98
7.4. Choice of Parton Density Function (PDF) set at generator level	99
7.5. Effect of Jet Energy Scale Variations on Signal Efficiency	100
7.6. Systematic Uncertainty on Signal Yield from Cleaning Filters and Object Veto	102
7.7. Interpretation in terms of new physics models	102
8. Conclusion	108
A. Maximum likelihood yields	110
B. Additional information on triggers	113
C. Addition information on background estimation methods	120
C.1. Determination of k_{QCD}	120
D. Closure tests and systematic uncertainties	121
D.1. Defining muon samples without an α_T requirement	121
D.2. Closure tests for inclusive analysis	122
D.3. Closure tests for b-tag analysis	123
D.4. Closure tests concerning pile-up	124
E. Signal efficiency	127
E.1. CMSSM	127
E.2. T1	128
E.3. T2	129
E.4. T2tt	130
E.5. T2bb	131
E.6. T1tttt	132
E.7. T1bbbb	133
E.8. Signal contamination for T1tttt	134
F. Experimental uncertainties on signal efficiency times acceptance	136
F.1. Systematics due to jet energy scale uncertainties	136
F.2. Systematics due to the MHT/MET cut	137
F.3. Systematics due to the dead ECAL cut	138
F.4. Systematics due to the lepton and photon vetoes	139

Bibliography	155
---------------------	------------

Chapter 1.

Introduction

The scientific method gives us a framework from which to quantify the world around us, experiment drives theory and theory drives the search for new observables. This continual positive feedback loop has driven revolutions in both technology application and the understanding of the fundamental processes seen in nature. The result of this is the ability to describe the motion of the stars and galaxies in the night sky using General Relativity and the interactions of the fundamental particles which are described by the SM.

However our understanding is incomplete, we are currently unable to produce a combined description of gravity and the interactions of fundamental particles. If our ideal of having some unified model which describes all dynamical interactions in the universe is to be fulfilled then some model which describes both of these regimes is desired. Our current best model, the SM predicts no dark matter, which has been conclusively inferred from cosmological observations. For example the rotational curves of the M33 galaxy[1] show that the amount of visible mass is not enough to confine the stars at the edges given their velocities as shown in Figure 1.1.

So far it is unknown if we are on the correct path with our descriptions of the universe at high energies and short time scales, experimentally our theories are supported. However, as they are built on conjecture it is impossible to divine how nature works outside of our experimental range. With this in mind the Large Hadron Collider (LHC) was designed and built to test our theories and search for the missing component (the Higgs Boson) of the SM at previously unattainable energy scales.

The LHC is a particle accelerator and collider, two counter rotating beams of protons are collided at four interaction points around its circumference. At design capacity

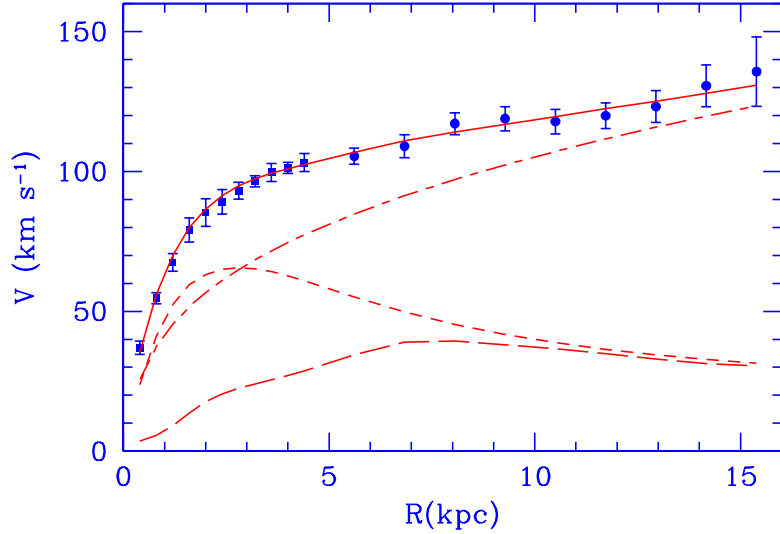


Figure 1.1.: M33 rotation curve (points) compared with the best fit model (continuous line). Where V is the radial velocity of the measured objects and R is the distance in kilo parsecs from the centre of the M33 galaxy. Also shown the halo contribution (dashed-dotted line), the stellar disk (short dashed line) and the gas contribution (long dashed line) [1].

these collisions occur every 25 ns or at a rate of 40 million times per second. The accelerator is situated in the Large Electron-Positron Collider (LEP) tunnel at CERN on the Franco-Swiss border. At 27 km in circumference it is the largest machine on Earth. It is constructed from 1624 niobium-titanium superconducting magnets, cooled to 1.8 K which produce a maximum field strength of 8.36 T, this magnetic field is used to bend the trajectories of the proton beams so they move in a circular path.

Protons are to be collided at a design centre-of-mass energy of 14 TeV, however design energy has not yet been realised, instead two runs, one at 7 TeV and the other at 8 TeV have been performed. The beams are collided to give an instantaneous luminosity of up to $1 \times 10^{34} \text{ cm}^{-2} \text{ s}^{-1}$, with a maximum instantaneous luminosity of $\approx 7 \times 10^{33} \text{ cm}^{-2} \text{ s}^{-1}$ delivered during the 2012 run. To achieve this luminosity the number of particles in each bunch must be high, this increases the likelihood that multiple interactions will happen in each bunch crossing. This is known as pile-up, this pile-up adds isotropic energy depositions to the events artificially increasing the scale. At peak instantaneous luminosity the average number of pile-up interactions is on the order of 25. Reducing the impact of the effects of pile-up is of high importance to the measurements performed at the LHC.

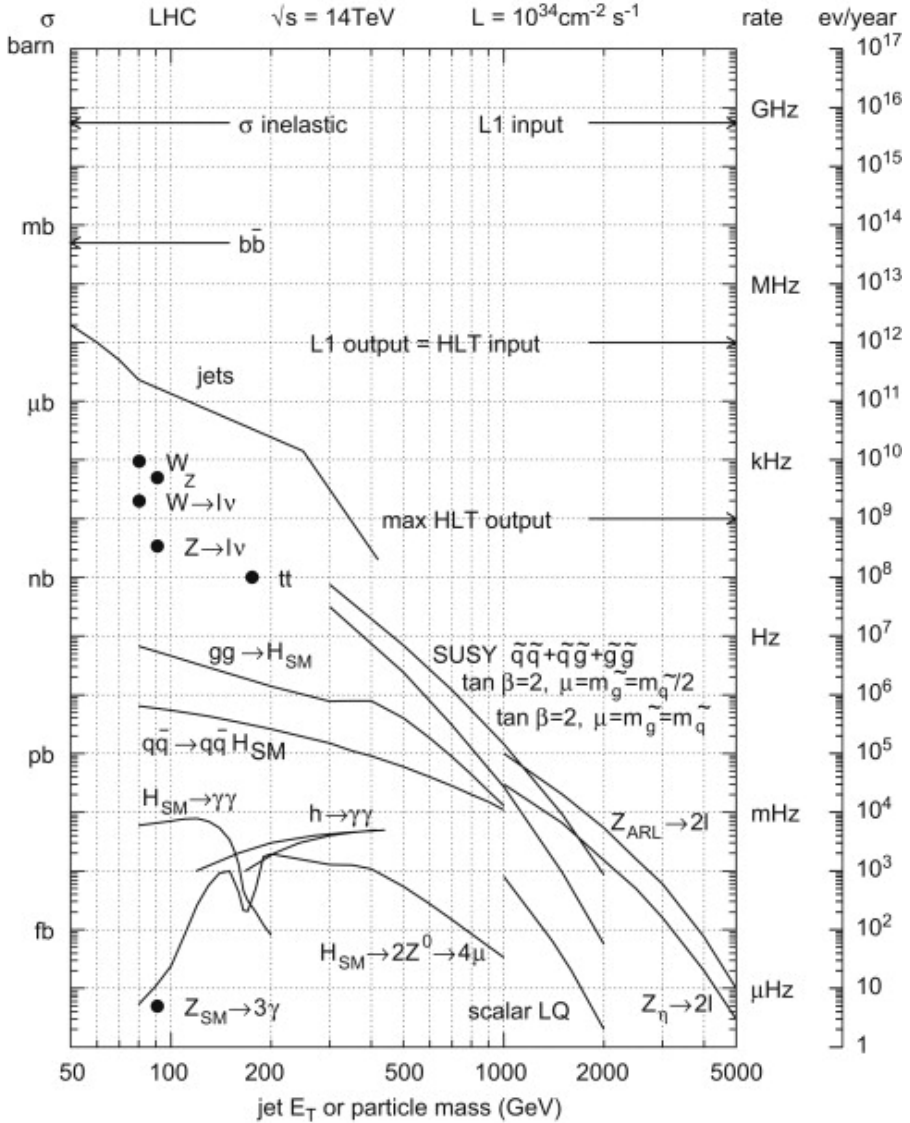


Figure 1.2.: Production cross sections at LHC design conditions for SM processes, Higgs production for various Higgs masses and SUSY production cross sections. Output rate is also shown as are the hardware limits due to the Level-1 trigger and the High Level Trigger[2].

Figure 1.2 shows the production cross sections of SM and Beyond the Standard Model (BSM) processes. To disentangle the already discovered low p_T physics from Electroweak and new unseen processes requires highly sophisticated particle detectors, four of which are employed at CERN for the LHC. These consist of two general purpose detectors: ATLAS[3] and The Compact Muon Solenoid (CMS)[4] the latter of which is described in detail in Chapter 3. The other two detectors are specialised. LHCb[5] is designed to study charge-parity violation in the b sector and perform precision

measurements of the SM. The ALICE[6] experiment is designed to study the quark-gluon plasma when the LHC is running in its secondary mode and colliding heavy ions, for example lead.

The low production cross sections for “interesting” new events mean that choosing which events to write out for later analysis and which events to reject is highly important and requires complex algorithms. This thesis covers triggering and a search for beyond the SM physics, which produces a dark matter candidate particle, using the data collected. In the absence of discovery, limits are set on the production cross section and mass scale of new physics models.

Chapter 2.

Theoretical Overview

In this chapter the SM of particle physics is outlined. The SM describes the particles and their interactions. Several limitations with this model are discussed, which motivate the need for a more complete theory. Some proposals for models beyond the SM and their theoretical motivation and possible physical realisation are discussed.

In addition the theoretical uncertainties on already known processes are discussed in terms of their effects on the level of accuracy of the simulation of both known processes and possible new models.

The particles of the SM are comprised of half integer spin matter particles, known as fermions, which exist in three families of chiral doublets for each of the leptons and quarks. The particles also have a charge conjugate partner which is their anti-particle. The force carriers comprise integer spin bosons which arise from the gauge invariance of the SM. Tables 2.1 and 2.2 list the names and observable quantities of the SM particles. The majority of observable mass in the universe consists of particles in the first generation of fermions, as the heavier generations decay via the charged weak interaction to particles in the first generation. In the next section the formalisation of the SM is described.

Name	Type	Generation	Spin	Charge (e)	Mass
Electron (e)	lepton	1	1/2	-1	511 MeV
Electron Neutrino (ν_e)	lepton	1	1/2	0	< 2.2 eV
Muon (μ)	lepton	2	1/2	-1	105.7 MeV
Muon Neutrino (ν_μ)	lepton	2	1/2	0	-
Tauon (τ)	lepton	3	1/2	-1	1.77 GeV
Tau Neutrino (ν_τ)	lepton	3	1/2	0	-
Up quark (u)	quark	1	1/2	+2/3	$2.3^{+0.7}_{-0.5}$ MeV
Down quark (d)	quark	1	1/2	-1/3	$4.8^{+0.7}_{-0.3}$ MeV
Charm quark (c)	quark	2	1/2	+2/3	1.275 ± 0.025 GeV
Strange quark (s)	quark	2	1/2	-1/3	95 ± 5 MeV
Top quark (t)	quark	3	1/2	+2/3	$173.5 \pm 0.6 \pm 0.8$ GeV
Bottom quark (b)	quark	3	1/2	-1/3	4.65 ± 0.03 GeV

Table 2.1.: The SM matter fermions, their masses, spin and charge. Values taken from [7].

Name	Spin	Charge	Mass	Force Carried
Photon (γ)	1	0	0	Electromagnetism
Gluon (g)	1	0	0	Strong Nuclear Force
W Boson (W)	1	-1	80.385 ± 0.015 GeV	Weak Nuclear Force
Z Boson (Z)	1	0	91.187 ± 0.002 GeV	Weak Nuclear Force
Higgs Boson (H)	0	0	$125.3 \pm 0.4 \pm 0.5$ GeV[8]	Fundamental Mass

Table 2.2.: The SM force carrying bosons, their masses, spins, charges and the force which they carry. Values from [7].

2.1. The SM

The SM of particle physics [9, 10, 11, 12] seeks to describe all of the observed matter particles and their interactions. The theory is a quantum field theory which is both invariant under local gauge transform and renormalisable. The theory is constructed from the unitary product group $SU(3) \otimes SU(2)_L \otimes U(1)_Y$ where $SU(3)$ describes the colour charged strong nuclear force and $SU(2)_L \otimes U(1)_Y$ describes the Electroweak interactions. The Electroweak sector contains bosons which have mass, which is contrary to what is inferred by the invariance under local gauge transform, which states that the gauge bosons should be massless. The $SU(2)_L \otimes U(1)_Y$ symmetry is thus seen to be broken. This is achieved by the addition of a scalar field with a non-zero vacuum expectation value, the extra degrees of freedom introduced by this scalar field allow the Electroweak bosons to gain mass without breaking the local gauge invariance of the Lagrangian. The method was proposed by Englert, Brout, Higgs, Guralnik, Hagen and Kibble [11, 13, 14, 15, 16, 17, 18] but is shortened to the ‘Higgs’ mechanism. The resulting mediator is known as the Higgs boson (H).

The SM matter particles have spin (1/2) and obey Fermi-Dirac statistics, they exist in three families of quark and lepton doublets. The force carrying particles have spin (1) except for the H which is predicted to have spin (0), they obey Bose-Einstein statistics and are collectively known as ‘bosons’. Figure 2.1 shows the hierarchy of the SM particles and the couplings between them.

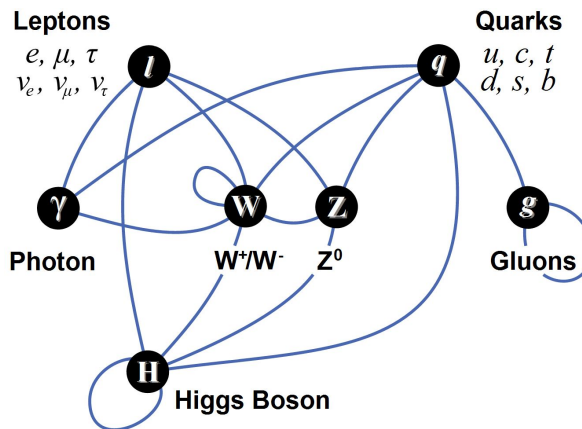


Figure 2.1.: Diagram of the SM particles, force carriers and their tree level interactions. Black circles represent particles and the blue lines represent the possible interactions.[19]

2.1.1. Gauge Invariance

Following the workings in [20], the example of adding a local gauge term to the free Dirac Lagrangian is chosen to show the effects of requiring a system to be invariant under local gauge transform. The free Dirac Lagrangian is written as

$$\mathcal{L} = i\bar{\psi}\gamma^\mu\partial_\mu\psi - m\bar{\psi}\psi, \quad (2.1)$$

under a simple global phase transform $\psi \rightarrow e^{i\theta}\psi$ and $\bar{\psi} \rightarrow e^{-i\theta}\bar{\psi}$ the exponents cancel and we are left with an invariant system. However if $\theta \rightarrow \theta(x)$ there is a θ dependent term introduced when evaluating the derivative which destroys the invariance of the system:

$$\partial_\mu(e^{i\theta}\psi) = i(\partial_\mu\theta)e^{i\theta}\psi + e^{i\theta}\partial_\mu\psi. \quad (2.2)$$

This infers that an extra term is added to the Lagrangian, i.e

$$\mathcal{L} \rightarrow \mathcal{L} - (\partial_\mu\theta)\bar{\psi}\gamma^\mu\psi \quad (2.3)$$

for convenience we set $\lambda(x) = -\frac{\theta(x)}{q}$ where q is the charge/coupling of the particle. We can re-express the Lagrangian as

$$\mathcal{L} \rightarrow \mathcal{L} + (q\bar{\psi}\gamma^\mu\psi)\partial_\mu\lambda(x) \quad (2.4)$$

when demanding that the entire Lagrangian is invariant under local transform one must add a term to cancel the additional term in Equation (2.4). We take

$$\mathcal{L} = [i\bar{\psi}\gamma^\mu\partial_\mu - m\bar{\psi}\psi] - (q\bar{\psi}\gamma^\mu\psi)\mathbf{A}_\mu \quad (2.5)$$

where \mathbf{A}_μ is some new field which transforms as

$$\mathbf{A}_\mu \rightarrow \mathbf{A}_\mu + \partial_\mu\lambda(x). \quad (2.6)$$

This property of \mathbf{A}_μ means that the Lagrangian is now invariant to the additions of a local phase or gauge. However \mathcal{L} must include a term for the free field \mathbf{A}^μ

$$\mathcal{L} = \frac{-1}{16\pi}\mathbf{F}^{\mu\nu}\mathbf{F}_{\mu\nu} + \frac{1}{8\pi}m_A^2\mathbf{A}^\nu\mathbf{A}_\nu \quad (2.7)$$

for the Lagrangian to remain invariant m_A must equal zero, $\mathbf{F}^{\mu\nu}$ is defined in Equation (2.12). The requirement that the Dirac Lagrangian be invariant under local phase or gauge transform necessitates the addition of a massless vector field \mathbf{A}_μ . The full Lagrangian is then given by

$$\mathcal{L} = [i\bar{\psi}\gamma^\mu\partial_\mu\psi - m\bar{\psi}\psi] - \left[\frac{-1}{16\pi} \mathbf{F}^{\mu\nu} \mathbf{F}_{\mu\nu} \right] - (q\bar{\psi}\gamma^\mu\psi) \mathbf{A}_\mu. \quad (2.8)$$

Equation (2.6) shows the choice of gauge, in this case the electromagnetic potential does not change the system. This addition of a local phase invariance to the free Dirac Lagrangian generates all electro dynamics.

The difference between the addition of a global phase and a local phase arises from the calculation of the derivatives of the fields

$$\partial_\mu\psi \rightarrow e^{-iq\lambda(x)} [\partial_\mu - iq(\partial_\mu\lambda(x))] \psi \quad (2.9)$$

here rather than picking up a phase factor we pick up a term involving $\partial_\mu\lambda(x)$, this can be removed by replacing ∂_μ in the full Lagrangian by the covariant derivative

$$\mathcal{D}_\mu \equiv \partial_\mu + iq\mathbf{A}_\mu \quad (2.10)$$

this replacement cancels the extra term in Equation (2.9). This substitution of \mathcal{D}_μ is an elegant method for promoting a globally invariant Lagrangian to a locally invariant one.

2.1.2. Electroweak symmetry and interactions

The example shown in Section 2.1.1 which describes the effects of requiring that the Lagrangian for a free Dirac particle be invariant under local gauge transformation infers the existence of a massless gauge field, which is responsible for the photon and electrodynamic interactions.

If we expand this so that rather than considering the Dirac equation for one free particle we consider two free particles, the requirement for invariance under local gauge transformation describes not only the interaction with the gauge field but also the inter particle interactions. In this case the covariant derivative \mathcal{D}_μ is expressed as:

$$\mathcal{D}_\mu \equiv \partial_\mu + iq\boldsymbol{\tau} \cdot \mathbf{A}_\mu \quad (2.11)$$

this promotes us to the $SU(2)_L \otimes U(1)_Y$ regime where there are a total of four gauge fields, τ represents the three Pauli matrices and \mathbf{A}_μ represents three gauge fields, these three gauge fields and the mixing with the gauge field seen in $U(1)_Y$ are responsible for the W and Z bosons and the photon. However as shown before, the requirement for the whole Lagrangian, including the terms for the free gauge fields, to be invariant under local gauge transform forces these gauge fields to be massless.

2.1.3. Quantum Chromo Dynamics

The component which describes the strong force is the $SU(3)$ term in $SU(3) \otimes SU(2)_L \otimes U(1)_Y$. A similar gauge invariance is required of the $SU(3)$ group as is required in the previous sections. However the gluon mass is measured to be zero, so this is not a broken symmetry. The eight gauge fields represent the eight colour combinations of gluons. The tensor in the Lagrangian is given by

$$F^{\mu\nu} \equiv \partial_\mu \mathbf{A}^\nu - \partial^\nu \mathbf{A}_\mu - 2q (\mathbf{A}^\mu \times \mathbf{A}^\nu) \quad (2.12)$$

where the cross product is given by

$$(\mathbf{B} \times \mathbf{C})_i = \sum_{j,k=1}^8 f_{ijk} \mathbf{B}_j \mathbf{C}_k \quad (2.13)$$

this cross product contains the self interaction of the gluon.

2.1.4. The Higgs and Electroweak Symmetry Breaking

It has been shown that the choice of representing the SM as a gauge invariant Lagrangian for the $SU(3) \otimes SU(2)_L \otimes U(1)_Y$ group product naturally gives the inter-particle couplings, interaction fields and the force carrying bosons. It has also been shown in [21] that these gauge invariant theories are renormalizable. However as shown in Section 2.1.1 the mass terms of the free fields are not locally gauge invariant, whilst this is not a problem for the photon or gluons as their masses are measured to be zero, it is a problem for the W and Z bosons which are massive [22, 23]. To break the Electroweak symmetry and give the W and Z mass, a scalar field with a non-zero vacuum expectation value is introduced into the Lagrangian[24, 25]. This field is known as the Higgs field, it breaks the symmetry of the $SU(2) \otimes U(1)$ group, introducing an extra degree of freedom which

can be used to give the bosons mass, the breaking method also predicts the recently observed [8, 26] Higgs boson.

2.2. Beyond the Standard Model.

The SM describes the fundamental particles, their interactions and the generation of fundamental mass to very high precision. However it is not a full description of the observed physics in the universe.

Firstly whilst the theory is invariant under special relativity, it is not invariant under general relativity and as such provides no description of the gravitational interactions of the fundamental particles. The combining of the theories predicts the radiation of energy though gravitational processes of the electrons orbiting an atomic nucleus, this would mean that matter is inherently unstable, which is easily shown to be false.

Secondly the observed matter anti-matter asymmetry observed is predicted by the SM. Whilst the SM does predict Charge-Parity (CP) violation, the rate predicted by the SM is not sufficient to account for the observed matter dominance in the universe.

There are also problems in the neutrino sector where the SM predicts that the neutrino is massless, however due to the observation of flavour changing the neutrino mass must be non-zero. The most glaring shortcoming other than the lack of a description of gravitational dynamics is the lack of a dark matter candidate. As shown in Figure 1.1 the amount of visible mass in galactic structures is not enough to account for the observed orbital velocities of stars at the galactic edges. I.e for these stars to be gravitationally bound there must be more mass in the galaxies than exists in the form of luminous bodies or inter-solar gas, both of which can be measured using telescopes in the viable and non visible spectrum.

Given that this matter is not observable in the viable spectrum, either directly or due to radiation produced when the particles interact when in close proximity, the matter must be weakly interacting only and stable as no decay signatures have been observed. This gives us one reason to theorise for particles that exist beyond the standard model. However there are many more reasons to predict BSM physics. A short summary of these other motivations is given below.

Given that it is expected that there is some unification scale, at which the magnitude of all the fundamental forces are equal, why is the weak force 10^{32} times stronger than

gravity? This question can be re posed as asking, why the Higgs mass is so much lighter than the plank mass? The radiative corrections with standard model only particles push the Higgs mass towards the unification scale. However as recently observed at the LHC, the mass of the Higgs boson is light[8, 26]. For this to be the case there must be a yet unobserved set of analogue particles with the spin quantum numbers mirrored between fermions and bosons when compared to those observed in the standard model particles, this is due to the spin-statistics theorem that states that bosons have a positive contribution to the Higgs mass and fermions have a negative contribution. One solution is to infer some new kind of symmetry, which predicts new particles. Due to the non zero mass of the Higgs and that these particles have not yet been observed, this symmetry must be broken[27]. However this is not the only proposed method to solve the hierarchy problem, others include the existence extra dimensions beyond the three space and one time dimension observed at the macro scale in the universe and the existence of a non zero cosmological constant.

If we take the consideration of finding a particle that satisfies the requirements of dark matter we enforce the following requirements on this particle, it needs to be heavy, stable, chargeless, colourless and interact via the weak nuclear force only. This requirement does not infer that all the particles predicted by some model satisfy these conditions, only the lightest of the family of particles need adhere to the requirements, meaning that the heavier particles can be analogues to the SM particles and the lightest particle being analogous to the neutrino. The stability can be achieved by the need for R parity conservation. R parity states that the total number of BSM particles is conserved at a vertex, much like other quantum numbers, e.g. the total number of particles and anti particles at a vertex, or the total spin. The requirement means that the BSM particles are pair produced and that the lightest BSM particle is stable.

Such particles are predicted by SUSY[28, 29, 30, 31, 32, 33, 34, 35] models, which can also include a quantised description of gravity. These models insert a further broken symmetry between bosons and fermions, i.e. for each SM boson there is a SUSY fermion and visa versa. In the case of the CMSSM it is the inclusion of gravity that breaks the SUSY symmetry giving rise to the mass difference between the super partners and their SM counterparts. The formalisation of SUSY allows a work around for the constraints imposed by the Coleman-Mandula[36] theorem, which states that the space-time and internal symmetries of a quantum field theory can only be combined trivially. This is due to the “supercharges” introduced by SUSY theories being spinor doublets rather than scalar charges. This allows for the extra symmetries introduced by such models.

2.2.1. The Constrained Minimal Super Symmetric Model

Whilst there are a plethora of SUSY models, in order to compare the CMS searches against previous and contemporary experiments the CMSSM[37] is chosen as a benchmark, however there are compelling reasons to study the CMSSM it's self. SUSY introduces 105 new parameters to the existing 19 of the SM. Sampling a space this large with sufficient coverage is prohibitive, instead the CMSSM reduces the number of free parameters to 5, these are: $\tan\beta$, where β is the ratio of the vacuum expectation values for the two Higgs fields; m_0 and $m_{1/2}$ which are the mass values for the boson and fermion states at the unification scale; A_0 which is the SUSY breaking tri-linear coupling; finally the sign of μ which is the Higgs breaking parameter. This is achieved by: enforcing the requirement for ‘R’ parity, the total number of SUSY and SM particles at a vertex, to be conserved, there are SUSY models where R parity is not conserved and the lightest SUSY particle has a finite lifetime; Requiring that the two Higgs doublets produce electroweak symmetry breaking; The gauge couplings are required to unify; The masses of the gauginos and scalars unify at the Grand Unified Theory (GUT) scale; Limits from experimental searches are also required to be satisfied, these include the requirement for the LSP to be a dark-matter candidate and that this LSP is both colour and electric charge neutral, the dark matter relic density is inline with astronomical observations and is inline with the measured age of the universe. Finally it is required that the theory does not need fine tuning of the particle masses to produce the current observed physics in the universe and to produce a stable theory. Given these physical constraints the CMSSM is a sensible model to interpret physical results from the LHC in terms of.

Throughout the accessible regions of these values, both Electroweak and strong production processes are predicted, as well as a multitude of final states involving a stable dark matter candidate particle χ_0 and SM particles. For the interpretation of the analysis presented in this thesis, limits are set as a function of m_0 and $m_{1/2}$ with fixed values for the other variables of $\tan\beta = 10$, $A_0 = 0$ and $\mu > 0$. Before LHC start up the preferred values for m_0 and $m_{1/2}$ as given by [38] were well defined and within reach of the early LHC SUSY searches. Table 2.3 lists the SM particles and their SUSY partners, it is to be noted that there is not a one to one correspondence between the particles as the observable states of the SUSY particles are mixed states of the directly symmetrized SM particles. Also SUSY introduces a second Higgs doublet, whilst these particles are not super partners of the SM particles they are added in addition to the SM Higgs boson.

Table 2.3.: List of the SM particles and their super partners. The neutralinos are the mixed state of the super partners of the chargeless SM bosons, note that there are now two Higgs doublets. The charginos are a mixed state involving the super partner of the charged W bosons and the charged Higgs boson (H^+) and the neutralinos are a mixed state of the neutral SM bosons [37].

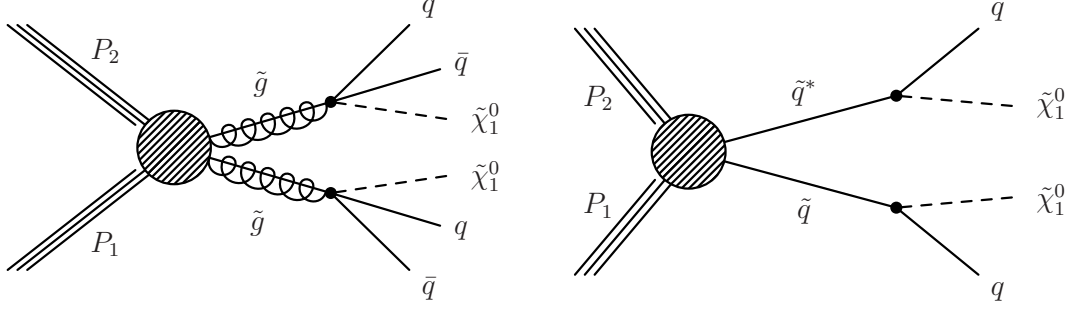
Partners	Super Partners	Spin	Charge
γ, Z^0, H^0, h^0	$\tilde{\chi}_0^0, \tilde{\chi}_1^0, \tilde{\chi}_2^0, \tilde{\chi}_3^0$	1/2	0
W, H^+	$\tilde{\chi}_0^+, \tilde{\chi}_1^+$	1/2	± 1
$e, \nu_\ell, \mu, \nu_\mu, \nu_\tau$	$\tilde{e}_{\bar{R}}, \tilde{e}_{\bar{L}}, \tilde{\nu}_e, \tilde{\mu}_{\bar{R}}, \tilde{\mu}_{\bar{L}}, \tilde{\nu}_\mu, \tilde{\nu}_\tau$	1	$\pm 1, 0$
τ	$\tilde{\tau}_0, \tilde{\tau}_1$	1	± 1
u, d, c, s	$\tilde{u}_R, \tilde{u}_L, \tilde{d}_R, \tilde{d}_L, \tilde{c}_R, \tilde{c}_L, \tilde{s}_R, \tilde{s}_L$	1	$\pm 1/3, \pm 2/3$
b	\tilde{b}_0, \tilde{b}_1	1	$\pm 1/3, \pm 2/3$
t	\tilde{t}_0, \tilde{t}_1	1	$\pm 1/3, \pm 2/3$
g	\tilde{g}	1/2	0

2.2.2. Simplified Models

The Simplified Model Spectra (SMS) models contain only one production process, for example a pair of gluions, or a pair of squarks which then decay via standard model processes, to a set decay topology, making the interpretation in these models simpler, however the individual models are not representative of some complete SUSY model. These are presented as an alternative to searching for a specific beyond the SM Lagrangian and its associated physical manifestation. The approach is to instead build a set of self consistent models of new physics, which are characterised by production and decay topologies[39]. Most generally this characterisation is based on the type of the pair produced particle (quark like or gluon like) and the mass splitting between this parent particle and the final state weakly interacting massive particle which provides a dark matter candidate. This method has several advantages over searching for a specific model:

- If a discrepancy with the SM is found, the amount of data collected during early running of the LHC will be insufficient to confirm or rule out most specific models of new physics;
- Generalised limits on decay topologies can be applied to many models and are useful for guiding model building;

- Difficult decay topologies such as those with small mass splittings can be investigated and analyses tuned to those areas of kinematic phase space.



(a) Production and decay of the T1 simplified process $pp \rightarrow \tilde{g}\tilde{g} \rightarrow q\bar{q}\tilde{\chi}^0 q\bar{q}\tilde{\chi}^0$ (b) Production and decay of the T2 simplified process $pp \rightarrow \tilde{q}\tilde{q} \rightarrow q\tilde{\chi}^0 \bar{q}\tilde{\chi}^0$

Figure 2.2.: Simplified model production and decay diagrams.

The models considered by this analysis require fully hadronic final states. Two production topologies are considered. Those involving gluino-gluino production which (pictured in Figure 2.2(a)) are referred to as T1 type models, where any suffix after the model type labels the flavour that the final state particles are forced to. T1 decays to four light (u,d or c) quarks and two $\tilde{\chi}^0$ particles, whereas T1tttt decays to four top quarks. Models that involve squark-squark production (pictured in Figure 2.2(b)) are referred to as T2 type production models, again any suffix denotes the flavour of the final state quarks. The decay topology involves two $\tilde{\chi}^0$ particles and two final state quarks which hadronise to form jets.

The final states involving heavy quarks are especially interesting as to solve the hierarchy problem the ratio $\frac{M_{top}}{M_{stop}}$ is required to be close to one as the top is the next heaviest particle to the Higgs and produces a divergence in the squared Higgs mass term. The addition of a bosonic partner to the top removes this divergence. Since the stop is expected to decay to a SM particles and the decay modes are akin to those in the SM, naturalness arguments would suggest that SUSY final states would contain SM top quarks and bottom quarks. Since the production cross sections of these particles are well understood in the SM a deviation in the number of events with bottom quarks and missing energy in the final state would be highly pronounced. Hence the analysis presented in this thesis considers bins with exclusive bottom quark requirements.

2.3. SUSY Searches at the LHC

As seen above, the decays result in a pair of chargeless, weakly interacting, stable SUSY particles ($\tilde{\chi}^0$) these particles provide a dark matter candidate and should leave a signature of a large amount of undetected energy, in proton-proton collisions the initial momentum of each of the colliding partons is not known as the proton is a composite object. However it is known that the momentum in the plane transverse to the direction of the proton beams (p_T) is zero. The final states that distinguish this new predicted physics from SM processes involve large amount of missing energy projected on to the transverse plane \cancel{E}_T . These events also involve the production of SM particles in the decay chain. The final states that are searched for in this analysis involve hadronic jets and missing energy.

However there are SM processes that produce signatures with missing energy in association with hadronic jets. These background sources need to be predicted or measured from SM processes, these predictions are then compared to the observed number of events in each of the signal regions, the compatibility of these results with the SM allows us to discover or rule out new physics models.

There are theoretical uncertainties introduced by the modelling of SM processes and their observable features at detector level. These apply equally to simulated beyond the SM processes. The first of these stems from the nature of the proton-proton collisions at the LHC, the other from the complexity of modelling the non gaussian effects inherent in measuring jet energies in calorimeter systems.

2.3.1. Parton Density Functions of the Proton

The proton is a composite particle and at its simplest it is a combination of three quarks, two up type and one down type, each of these carry a third of the proton's mass-energy. However this picture is overly simple. As seen from Table 2.1 the mass of the constituent quarks sums to ≈ 10 MeV, however the mass of the proton is ≈ 1 GeV, the majority of the mass comes from the binding forces inside the proton and from the virtual particles which arise from the dynamics of the strong force and quantum mechanics.

This has several implications, the first of which is that it is impossible to know which particles have interacted when a collision occurs and what fraction of the proton's total momentum was being carried by that particle, hence the total energy of the system is unknown. However, it is an accurate approximation to assume that the energy in

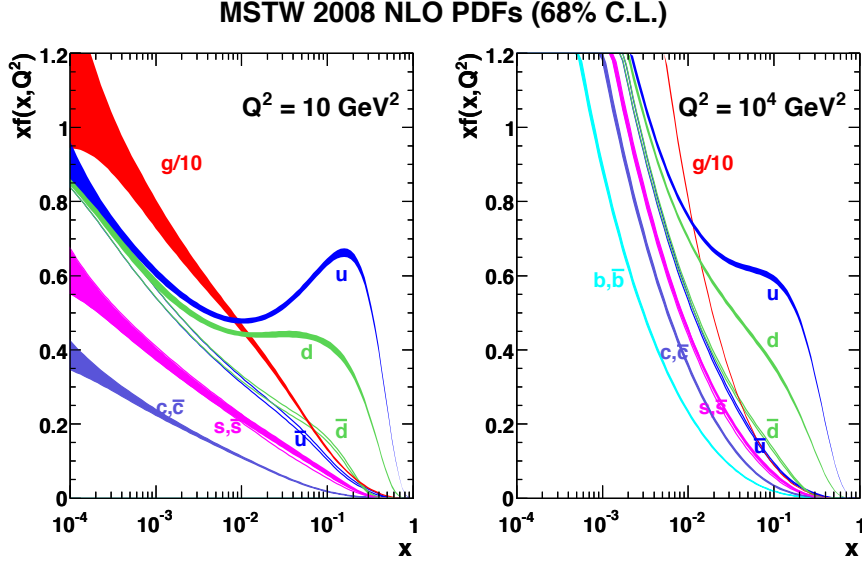


Figure 2.3.: MSTW 2008 NLO PDFs at $Q^2 = 10 \text{ GeV}^2$ and $Q^2 = 10^4 \text{ GeV}^2$ [40]. Where x is the fraction of the momentum carried by that parton type.

the plane transverse to the direction of travel is zero, hence at hadron colliders many observables are measured in terms of the observed energy deposited in the plane transverse to the beam direction.

The second major implication is that at different interaction energies the components of the proton change, as shown in Figure 2.3, where x is the fraction of the proton's momentum carried by that particle. These PDFs have not been measured at very high Q^2 , as seen at the LHC. However, they have been extrapolated from the measurements at lower energies. When the production cross section depends on the energy of the interacting particles the uncertainty has a large effect on the calculation of the production cross sections of new physics processes.

2.3.2. Hadronization Models

The “true” fragmentation and formation of colour neutral hadrons from single quarks or gluons is not yet understood from first principles, starting with the QCD Lagrangian. However, effective models have been produced that do a reasonable job of producing colour neutral final states for simulated Monte Carlo events.

Chapter 3.

The CMS detector

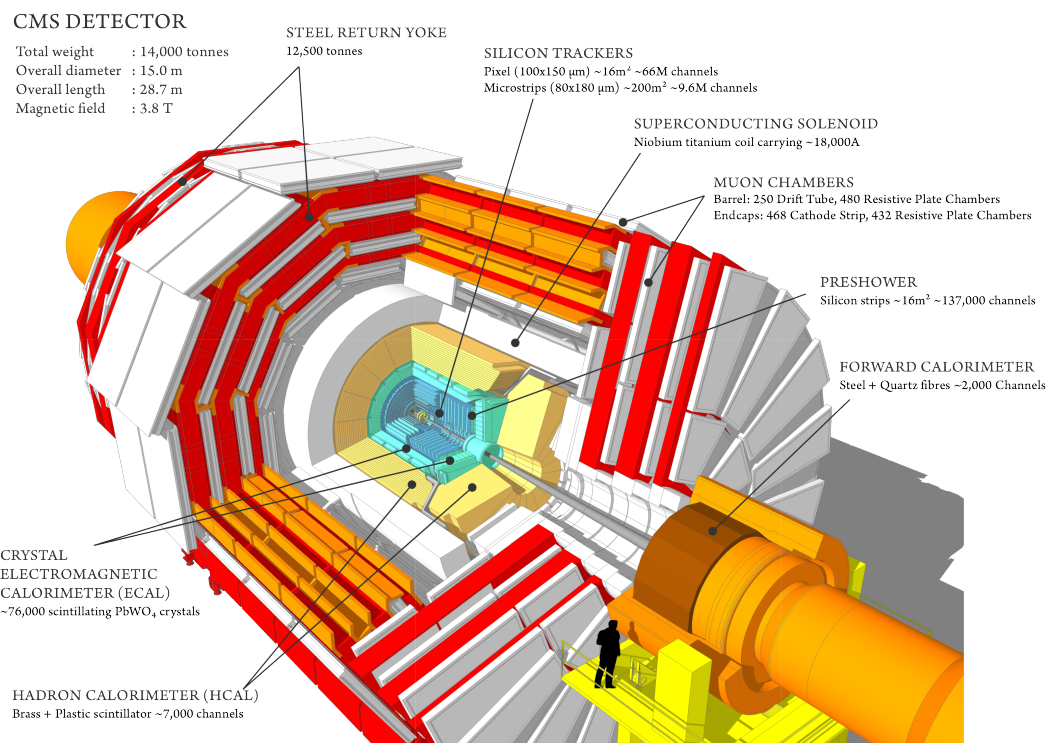


Figure 3.1.: A perspective view of the CMS detector[41].

The Compact Muon Solenoid (CMS) detector was designed and built to study proton-proton interactions at the LHC, with the aim of discovering the Higgs boson and searching for beyond the SM physics signals. The detector is a traditional onion layer design, with high precision tracking detectors nearest the interaction point and high energy resolution calorimetric detectors in the outer layers. Due to the predicted presence of missing energy \cancel{E}_T in new physics models, energy measurement over the full η range is required. As alluded to in the name the possibilities of the new physics models containing muons and

the “golden” Higgs decay channel $H \rightarrow ZZ \rightarrow \mu\mu\mu\mu$ and Z' models, the detector was designed to accurately reconstruct muons with p_T of up to 1 TeV. Due to the ability to distinguish these leptons from the large amount of hadronic fragmentation caused by smashing two protons together, at a centre of mass energy of 14 TeV. The CMS Electromagnetic calorimeter, was also designed to have precise energy measurement and fine grain spatial resolution. This design feature was motivated by the Higgs decay channel $H \rightarrow \gamma\gamma$. The other new feature of CMS, is the use of silicon detectors throughout for particle tracking. These give precise track reconstruction abilities and the associated fine grain resolution in both position and momentum. All the sub-detectors save the muon system, are contained within the barrel of a 4 T superconducting solenoid. This magnet provides the particle track bending required for momentum and lepton charge measurement. In this section the key detector elements and their design parameters are discussed.

3.1. The Silicon Tracker

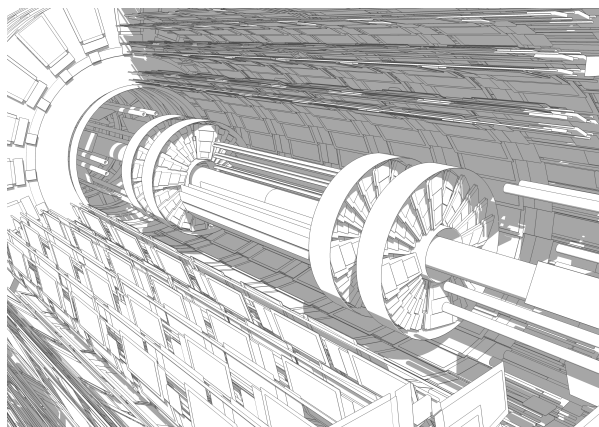


Figure 3.2.: The CMS tracking system, pixel detectors are situated at the centre of the detector closest to the interaction point, surrounded by layers of silicon strip detectors[41].

The design goal for the CMS tracking system, was to produce a system that can precisely and efficiently measure the trajectories of charged particles produced in LHC collisions. The tracking system surrounds the collision point and has a length of 5.8 m and a diameter of 2.5 m. At the LHC’s design instantaneous luminosity of $10^{34} \text{ cm}^{-2} \text{ s}^{-1}$, an average of 1000 charged particles from more than 20 proton-proton interactions will be produced per 25 ns bunch crossing. This imposes the requirements of high granularity,

so that the individual particles and their trajectories can be distinguished and a fast response, so that the hits can be assigned to the correct bunch crossing. The technical implications of these requirements imply both, a large amount of on-detector electronics and their associated cooling equipment. This large amount of tracker material increases the multiple scattering, bremsstrahlung, photon conversion and nuclear interactions of the particles which are traversing the tracking system. This in turn limits the position and energy resolution of the calorimeter systems. A compromise between the material budget of the tracking system, the desired features and the requirement for the tracking system to have an expected life time of 10 years in a high radiation environment, resulted in the construction of the tracking system using only solid state silicon detector technology.

The CMS tracking system is formed of a pixel detector with three layers situated between at radii of 4.4 cm and 10.2 cm from the interaction point and a silicon strip tracker with 10 barrel layers extending outwards to a radius of 1.1 m from the interaction point. The barrel layers of both the pixel and strip detectors are complemented by layers of either pixel or strip disks, which extend the acceptance of the tracker to $|\eta| < 2.5$. The resulting structure is that of a detector with 200 m^2 of active silicon, which makes the CMS tracker the largest detector of its type ever constructed.

The individual pixels that comprise the pixel detector are $100 \times 150 \mu\text{m}^2$, which corresponds to an occupancy of around 10^{-4} per bunch crossing. The detector cell size for the microstrip detectors at a radius between 20-55 cm is $10 \text{ cm} \times 180 \mu\text{m}$ which leads to an average occupancy of 2-3%. Further out at a radius greater than 55 cm the minimum cell size is increased to $25 \text{ cm} \times 180 \mu\text{m}$ with an occupancy of around 1%. The tracker performance is extensively documented in [42].

3.2. The Electromagnetic Calorimeter (ECAL)

The CMS electromagnetic calorimeter[43] is a hermetic, homogeneous calorimeter constructed from lead tungstate (PbWO_4) crystals. The ECAL is split into two parts, a barrel covering $|\eta| < 1.479$ read out by avalanche photodiodes and the two end-caps covering $1.479 < |\eta| < 3.0$, read out by vacuum photo-triodes.

Lead tungstate crystals were chosen because of their short radiation length, fast scintillation and radiation hardness. During the research and development program it was shown that, radiation damage does not affect the scintillation method or the

uniformity of the emitted light yield along the crystal, it only effects the transparency, through the creation of colour centres. This will be monitored throughout the lifetime of the ECAL via a light injection system[44].

The barrel crystals have a front face of $22 \times 22 \text{ mm}^2$, this corresponds to the Molire radius of $\approx 22 \text{ mm}$; with a length of 230 mm giving a each crystal length of $25.8X_0$, where X_0 is amount of material required for 68% of an electromagneticly interacting particle's energy to be radiated, in the form of bremsstrahlung or pair production whilst traversing that material. For lead tungstate this length is $X_0 = 0.89 \text{ cm}$. They are arranged in 36 super-modules, forming two half barrels. The crystal axes are skewed at 3° with respect to the vertex and each covers 1° in ϕ and η

The endcap crystals are arranged in two semi-circular ‘Dees’, groups of 5×5 crystals are canter-levered on a aluminium backing plate. The crystals are again skewed with regard to the interaction vertex, however they are arranged in an $x - y$ grid rather than a $\phi - \eta$ grid. The crystal dimensions are different to the barrel, in that the cross section is $28.6 \times 28.6 \text{ mm}^2$, with a length of 220 mm corresponding to 24.7 radiation lengths

In addition to the ECAL there is a pre-shower detector situated at $1.653 < |\eta| < 2.6$. This provides identification of isolated electrons against electrons produced in showers. Each particle passes though the detector leaving a minimum ionising track, or hit. The number of these hits per area gives information on the isolation of the particle and improves the position measurement of electrons and photons in the ECAL endcaps.

Figure 3.3 shows the change in response of the ECAL during running, due to the formation of colour centres, this response is measured using laser light at 440 nm and is used to correct the energies recorded in data during each run to form a uniform response. The ECAL performance in 2011 is extensively documented in [46].

3.3. The Hadronic Calorimeter (HCAL)

The design of the CMS HCAL is constrained by the size requirements of fitting the tracking system, ECAL and HCAL inside the solenoid magnet. The HCAL is situated between the ECAL which ends at a radius of 1.77 m and the solenoid which starts at a radius of 2.95 m. This constraint limits the amount of material which can be put in place to fully contain the hadronic showers. To overcome this an outer layer of instrumentation is placed outside of the magnet and cryogenic system, in order to fully contain hadronic

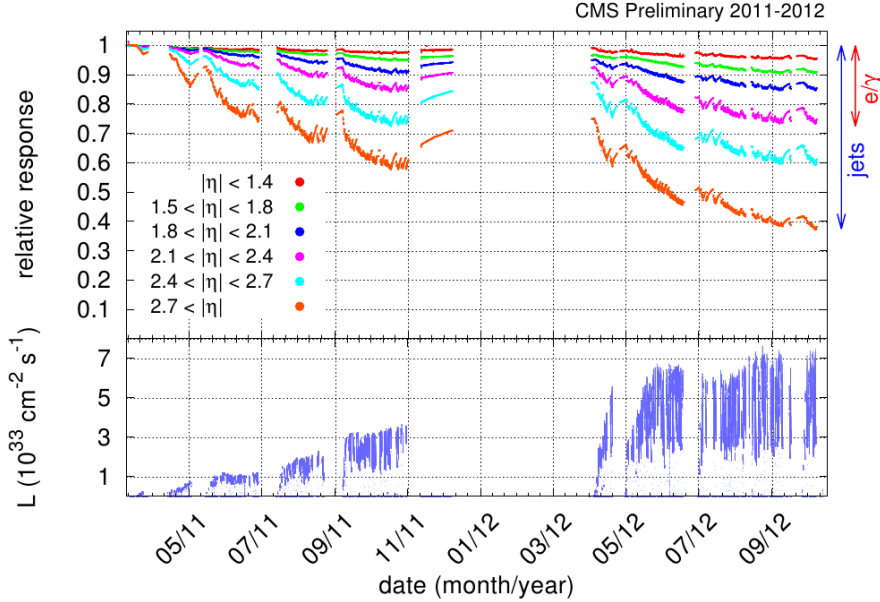


Figure 3.3.: Relative response to laser light (440 nm) measured by the ECAL laser monitoring system, averaged over all crystals in bins of pseudo-rapidity, for the 2011 and 2012 data taking periods. The response change observed in the ECAL channels is of the order of a few percent in the barrel, while it reaches up to 25% in the most forward endcap regions used for electron and photon reconstruction. The response change is up to 60% in channels closest to the beam pipe. These measurements are used to correct the physics data.
The bottom plot shows the instantaneous LHC luminosity delivered during this time period[45].

showers. The full containment of the hadronic objects is necessary for precise missing energy measurement, which is a key discriminatory feature for new physics models with undetectable final state particles.

The hadronic calorimeter is split into three sub detectors, the hadronic barrel (HB) $|\eta| < 1.3$, hadronic endcaps (HE) $1.3 < |\eta| < 3.0$ and a forward calorimeter (HF) $3.0 < |\eta| < 5.5$.

The HB and HE comprise seals of layered tiles of brass absorber plates interspersed with scintillator plates which are read out by wavelength shifting fibres. The total absorber thickness varies between 5.2 and 10.6 interaction lengths, the ECAL adds approximately one extra interaction length. The scintillators are segmented into towers of area $\Delta\eta \times \Delta\phi = 0.087 \times 0.087$ in the barrel and $\Delta\eta \times \Delta\phi = 0.17 \times 0.17$ in the endcaps. The light produced in the scintillators is merged in the wavelength shifting fibres and then read out using hybrid photo-diodes. The HF is constructed from radiation hard

quartz fibres, this enables the detector to survive in the very forward regions of the detector where high levels of radiation are experienced.

The hadronic outer (HO) which is situated outside the solenoid used the solenoid coils as an extra absorber adding extra interaction lengths in the barrel region ensuring full containment of hadronic showers. The HO is constructed from layers of scintillator tiles, the light from which is then merged in the wavelength shifting fibres and read out using hybrid photo-diodes. HCAL performance is documented in [47].

3.4. The Superconducting Solenoid

The requirement for precise muon momentum measurements, for muons with $p_T > 1 \text{ TeV}$ infers the requirement of large bending power, this requirement forces the choice of a superconducting magnet. The CMS magnet is 13 m long, has an inner diameter of 6 m and provides a 4 T magnetic field, which gives a bending power of 12 Tm before the muon bending angle is measured by the muon system. The bore of the solenoid contains the tracking and calorimeter systems. The magnet is constructed from Niobium-Titanium superconductor embedded in an aluminium stabiliser, it is coiled in four layers resulting in 220 t of cold mass. This is then cooled to around 4 K using liquid helium and a current of $\approx 20 \text{ kA}$ is applied to generate the magnetic field.

3.5. The Muon system

The CMS muon system, is designed to provide accurate muon p_T measurements ($\sigma(p_T)/p_T < 0.1$) for muons over a large p_T range. Due to the cylindrical nature of the solenoid, the muon system is also designed to be cylindrical. The muon system has three purposes. The first is the identification of muons. The second is the momentum measurement of these muons. The third is to provide information to the trigger system. The muon system uses three types of gaseous detectors for particle tracking and identification. In the barrel region where the magnetic field is uniform, drift chambers (DT) are used, these cover the region $|\eta| < 1.2$ and are interspaced between the layers of the magnetic flux return plates. In the endcap regions where the muon and background rates are higher and the magnetic field is non-uniform, cathode strip chambers (CSC) are used due to their fast response, radiation hardness and fine grain segmentation. The CSCs cover $0.9 < |\eta| < 2.4$. Due to

the initial uncertainty on the background rates and the 25 ns bunch crossing intervals expected when the LHC is running under design conditions, a complementary dedicated muon triggering system consisting of Resistive Plate Chamber (RPC) was added in the range $|\eta| < 1.6$. The RPCs provide a fast, independent and fine grain system from which to trigger on muon objects in the harshest of running conditions.

Due to multiple scattering and the sheer quantity of detector material before the first muon station, momentum measurement using the muon system only is accurate to a level of $\approx 10\%$ below 200 GeV and accurate to a level of 15 – 40%, $|\eta|$ dependent for 1 TeV muons. When including the tracker information in the muon momentum measurement the resolution is improved to $\approx 1\%$ below 200 GeV and to about 5% for 1 TeV muons. The performance of the CMS muon system is detailed in [48].

3.6. The Level-1 Trigger System

The CMS trigger system is designed in two levels. The first, the Level-1 trigger is built using custom electronics and is designed to reduce the input rate of 40 million events per second, to a manageable rate of 100 thousand events per second. Information from only the calorimeter and muon systems is considered as the time required to read out the tracking information is prohibitive at this level. Two separate trigger systems, one performing triggering on the calorimeter system, the other performing triggering on the muon systems are employed. For a detailed discussion of the calorimeter triggering algorithms and their performance see Chapter 4. The information from these two sub triggers is passed to the global trigger, where the decision to accept the event or not is made. The muon trigger considers information from each of the DT, CSC and RPC muon systems. Tracks are created from the hits in each of the sub systems and fitted. The muon momentum is then calculated from the radius of curvature of these muons. The four highest p_T muon candidates are then passed to the global trigger. Electron and photon candidates are created by the regional calorimeter trigger. The Global Calorimeter Trigger creates jet candidates, energy and missing energy sums. The four highest E_T jet candidates of each type, central, tau and forward, the energy sums and the electron/photon candidates are then passed to the global trigger, where the final trigger decisions are made. These decisions can require information from a single detector or can require coincident objects, such as the requirement of an energy sum value and a muon.

3.7. The High Level Trigger System

The High Level Trigger (HLT) system is constructed from off the shelf components. The system is composed of two sets of machines. The first are the Event Builder (EB) units, these build raw data into regional chunks from the data read out at the front end of the detector when a Level-1 accept is received, this is then combined and transmitted to the Event Filter (EF) cluster. The EB units transfer the data to the EF units via a standard TCP/IP gigabit ethernet link. The task of the EF units is to run complex reconstruction algorithms, using combined detector information to reduce the accepted data rate to a manageable level. The original design anticipated an output rate of 100 events per second, however in 2012 running, 1000 events per second were stored, half of this rate was assigned to the prompt reconstruction queue, the other half was stored for reconstruction during the long shut down of the LHC in 2013-2015.

The EF farm is formed from standard rack-mounted PC units, with a total of approximately 1000 computing cores, operating at a clock frequency of around 2 GHz. Upon receiving an event, each unit performs the CMS reconstruction, using the same software framework as used for offline analysis, meaning that the objects used for trigger decisions are as close in definition to the offline objects as possible. This increases the overall trigger efficiency, however the calibrations used at HLT level are not the final derived versions. Trigger chains are designed so that full event reconstruction can be performed. However when designing a trigger that requires full tracking reconstruction, pre-selection requirements are made before the computationally complex stages are performed, if any of these pre-selections are not satisfied the full event reconstruction is not performed. The EF farm is connected to a large (several hundred terabytes) storage area network, this acts as a temporary storage area for the events accepted by the HLT before the events are transferred to the tier-zero reconstruction farm, which is located at the central CERN site.

Chapter 4.

Level-1 Calorimeter Trigger

In this chapter the Level-1 calorimetric triggers are detailed and their performance is measured with respect to various offline quantities which are defined to match the HLT level objects. The performance is measured under evolving pile-up conditions, the impacts of analyses evolving to use pile-up corrected offline variables are measured with respect to the Level-1 quantities. Finally a method for reducing the impact of pile-up on Level-1 trigger rate without directly raising the trigger thresholds is studied and the change in performance due to this change is then studied.

The nomenclature for the Level-1 trigger algorithms is as follows L1_AlgoType Threshold for example L1_HTT150 refers to a Level-1 trigger requiring $H_T > 150$ GeV.

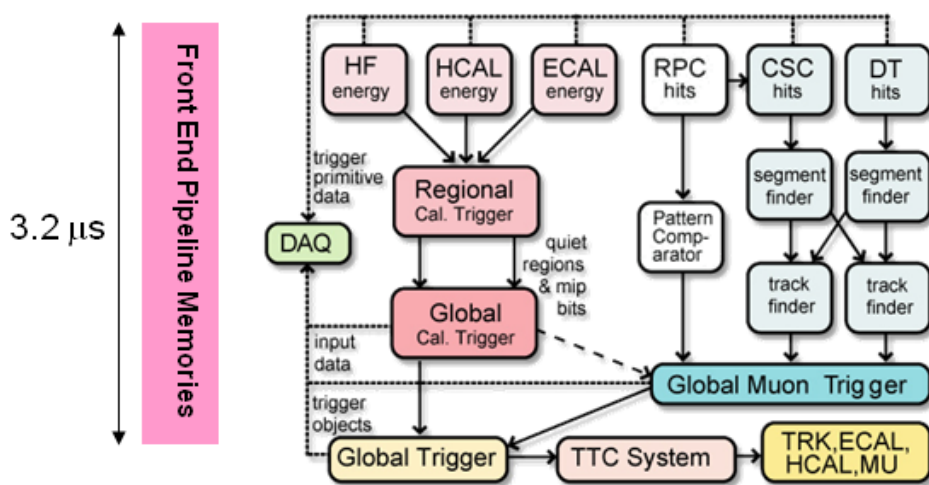


Figure 4.1.: The CMS Level-1 Trigger system.

The CMS Level-1 trigger system[49] is a pipelined dead-timeless system based on custom-built electronics. The Level-1 trigger is a combination of several sub systems, which are interconnected as depicted in Figure 4.1.

Coarse information from the electromagnetic, hadronic and forward calorimeters is processed by the Regional Calorimeter Trigger (RCT). This is then passed to the Global Calorimeter Trigger (GCT), where the coarse grain information is clustered into physics objects. These objects are then passed to the Global Trigger (GT) where the Level-1 accept decision is made. Due to the limited size of the pipeline this Level-1 accept must be issued within $4.0\ \mu\text{s}$.

The objects passed from the GCT to the GT include: electromagnetic objects, which include both electrons and photons, as due to the lack of tracking information at the Level-1 trigger these objects are indistinguishable, jets and energy sums.

The RCT generates up to 72 isolated and non-isolated electromagnetic objects. These are sorted by rank, which is equivalent to transverse energy E_{T} . The four highest ranked electromagnetic objects are then passed via the GCT to the GT at an equivalent data rate of $29\ \text{Gbs}^{-1}$ per type.

Hadronic objects undergo two clustering steps. First the transverse energy sums of the ECAL and corresponding HCAL towers are calculated, the towers are then summed into 4×4 trigger regions, these are passed to the GCT at a data rate of $172.8\ \text{Gbs}^{-1}$. These trigger regions are clustered into jet candidates by the GCT and ranked. The jets are then sub-divided in the categories depending on their pseudo-rapidity and the result of τ identification.

Energy sums come in two forms. The total transverse energy E_{T} , which is the scalar sum of all transverse energies and the total jet transverse energy H_{T} , which is calculated as the scalar sum of all jets above some programmable threshold.

The missing energy equivalents of these, \cancel{E}_{T} and \cancel{H}_{T} , are formed from the negative vector sum of the objects considered for the transverse sums.

4.1. Level-1 Trigger Jet Algorithm

The Level-1 trigger algorithm is detailed in [50]. The CMS detector can be un-rolled in the ϕ direction to form a rectangular grid of the 396 calorimeter regions, connected along

the ϕ edge. The rectangle is formed from 18 ϕ divisions (from $-180^\circ < \phi \leq 180^\circ$) and 22 η divisions (from $-5 < \eta < 5$). Each ϕ division corresponds to 20° . The η divisions correspond to $\Delta\eta = 0.5$ in the forward calorimeters and to $\Delta\eta \approx 0.348$ in the barrel. A pictorial representation of this can be seen in Figure 4.3.

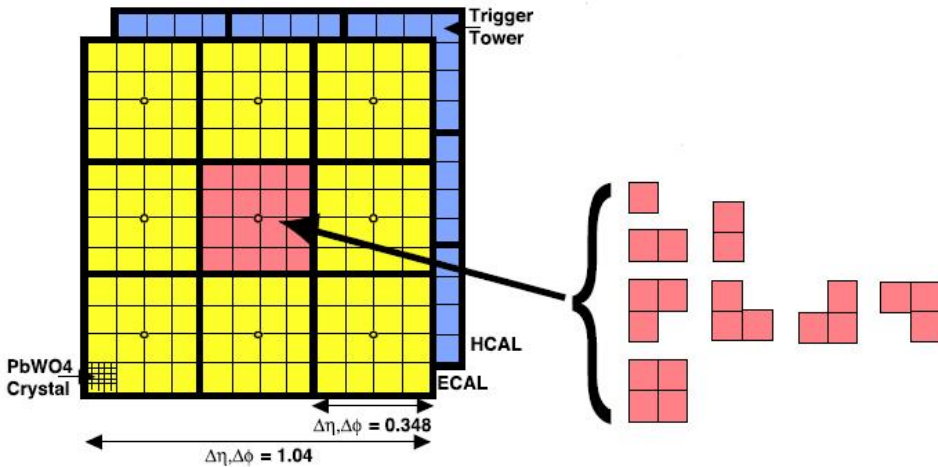


Figure 4.2.: The 3×3 jet-finder window at Level-1. Each deviation represents a 4×4 grouping of ECAL crystals which form a trigger tower. The ECAL energies are then summed with the corresponding HCAL tower energies. The τ -jet veto patterns are shown to the right.

A jet candidate is created when the sum of the HCAL and ECAL energies of the central calorimeter region has an energy deposit larger than all of its neighbours, as shown in Figure 4.2. The jet is centred at the region where $p_T^{central} > p_T^{surrounding}$ and the transverse energies of the surrounding regions are summed into the central region. The jet is then classified as a τ jet if $|\eta| < 3.0$ and none of the τ veto bits are set. If any τ vetoes are set the jet is classified as a central jet. The jet is classified as forward if $3.0 < |\eta| < 5.0$

The τ -vetoes are set by the RCT, depending on whether or not the energy depositions in up to four contiguous trigger towers are below a programmable fraction of the regional E_T , as shown in Figure 4.2. These topologies are due to the hadronic decay modes of the τ containing one or three isolated pions. Any signal that deposits energy in all the trigger towers in a region is not from one or three isolated pions.

It is possible to apply separate jet energy corrections to each of the sub categories of GCT jets, however at current the same E_T and η dependent corrections are used for all three jet types.

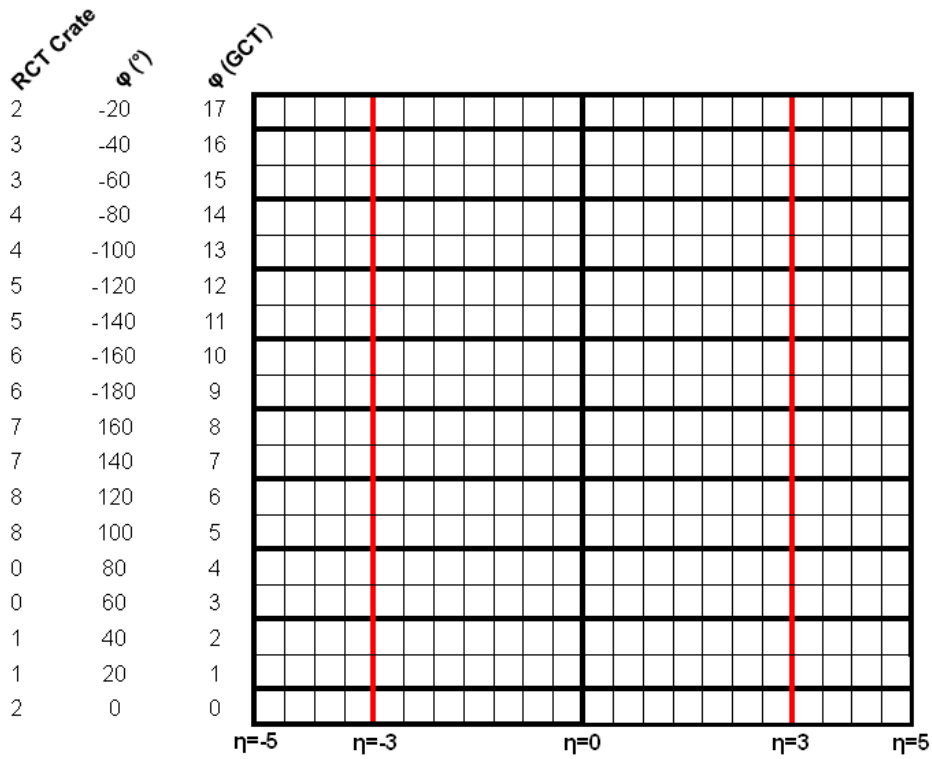


Figure 4.3.: The calorimeter map that the 3×3 jet-finder operates over is made up of 396 calorimeter regions. Each jet finder is mapped on to an RCT crate which is composed of an 11×2 strip of these regions. RCT crate labels are shown for negative η only.

In order to reduce the total data duplicated and shared between the jet finders, the GCT employs a pre-clustering algorithm, which involves 18 jet finders operating simultaneously over the whole detector. These jet finders then only share information with neighbouring regions, when the clustered jets are found. Figure 4.3 shows the boundaries between which the jet finders operate, these map naturally on to one RCT crate per jet finder. A maximum of three jets can be found on each of the ϕ strips acted on by the jet finders, this gives a maximum of 108 jets per event. In order to preserve continuity across the $\eta = 0$ boundary, the two adjacent trigger regions are shared between the jet finders.

An example of the jet finding is shown in Figure 4.4. The first step is to create a 2×3 mini cluster around any local maxima found in the 12×2 strip (the strips are 11 cells long, however the first cell from the adjacent strip is shared so that no jet clusters are missed). Equality statements are imposed so that the energy of the central cell is greater than its neighbours in some directions and greater than or equal to the neighbours other

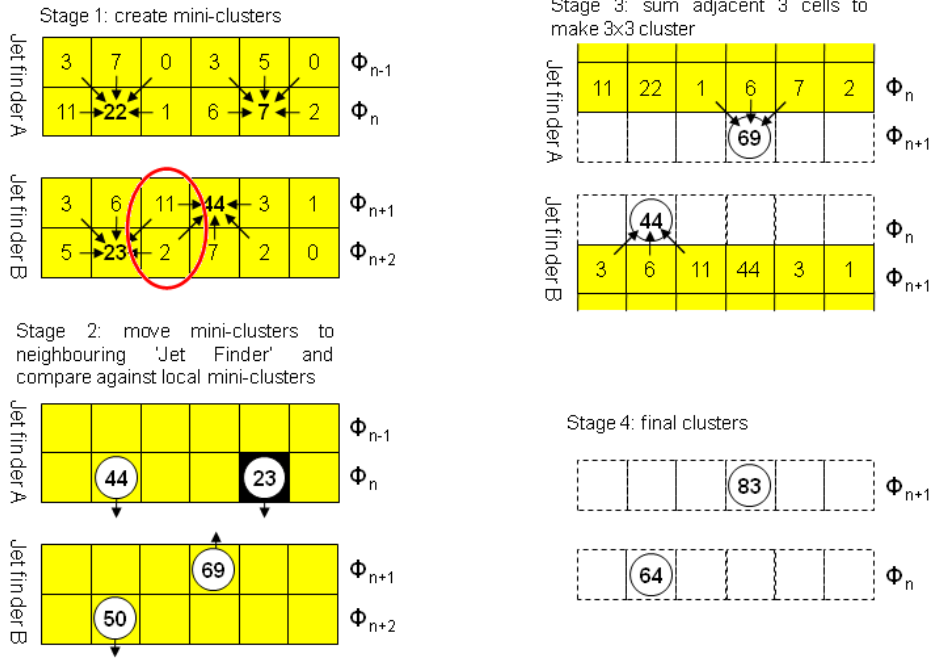


Figure 4.4.: The Level-1 jet clustering method, six cells in η are shown. An example of overlapping jets is shown.[51]

directions to enforce a gap of at least one trigger region in both η and ϕ between the centres of the clustered jets.

In the second step, the jet finder transfers the three largest mini clusters on a given ϕ strip, to the closest ϕ strip on the neighbouring jet finder. These are then compared against the existing mini clusters in that ϕ strip, those that are adjacent or diagonally adjacent to a larger mini cluster are removed. The inequality statements are then reimposed to prevent problems with clusters having the same energies. In the final stages the mini clusters have their three adjacent regions summed to produce a 3×3 jet cluster. Finally the four highest ranked jets are corrected and passed to the GT.

4.2. Level-1 Trigger Performance

During the start of data taking in 2010, no Jet Energy Corrections (JEC) were applied in the Level-1 trigger. This gave a large difference in energy between the energy of the Level-1 objects and the offline objects, i.e. the energy range over which the objects ‘turn on’ is large, giving a relatively slow turn on in terms of offline hadronic objects. During the winter shutdown of the LHC between the 2010 and 2011 running periods, a

set of Level-1 JEC were developed. These corrections used a piecewise cubic form for the interpolation function used to correct the jet energy, dependent on its uncorrected E_T and η values. However as can be seen in Figure 4.5 these corrections were only applied to jets with a raw energy below 130 GeV, the secondary lobe shows those objects that do not have their energies corrected.

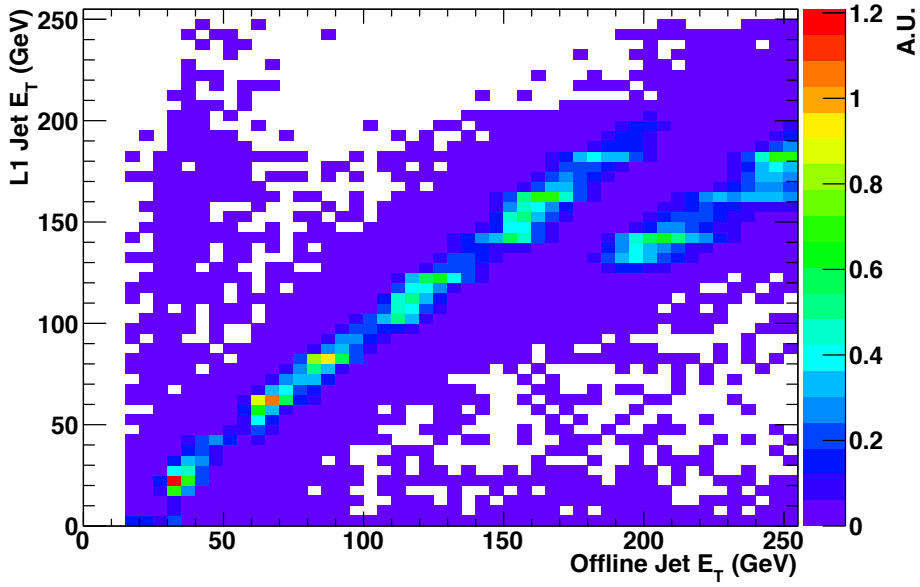


Figure 4.5.: Correlation between offline corrected jet energy and Level-1 corrected jet energy for matched jets. The discontinuity shows where the Level-1 jet corrections do not alter the raw energy of the jet. The z-axis is measured in arbitrary units.

To overcome this a new set of corrections were derived, using a well established tool for producing offline corrections, using the same functional form that was derived for correcting particle flow jets[52]. In this section we discuss the performance of both sets of Level-1 JEC and the performance of the energy sum and missing energy triggers H_T , \cancel{H}_T , and \cancel{E}_T . The performance of which are not effected by the application of jet energy corrections at the Level-1 trigger, due to the quantities being built from the internal GCT jets before they pass-through the corrections look up table. The performance is studied under both low pile-up conditions where the mean peak pile-up $\langle PU \rangle$ is 16 primary vertices and under high pile-up conditions where $\langle PU \rangle$ is 36 primary vertices.

To measure the performance of the Level-1 single jet triggers we assume that the leading offline corrected anti- k_t calorimeter (see Section 5.1.1 for a description of the offline jet clustering algorithm) jet is the jet that triggered the event. We then match this offline jet to the closest Level-1 jet in ΔR ($\Delta R = \sqrt{((\Delta\eta)^2 + (\Delta\phi)^2)}$), where for there

to be a match $|\Delta\mathcal{R}| < 0.5$ is required. For this match central, τ and forward jets are considered. Events where the recorded Level-1 energy is set to the overflow bit, meaning they have more than 254 GeV of E_T measured at Level-1, are ignored.

To collect an unbiased sample in which to measure the performance, two methods are used. The first is to require a Minimum Bias trigger, which is triggered by beam induced activity in the CMS detector. However due to the nature of these collisions the number of events with high energy interactions is low and the prescale applied to this trigger further reduces the sample size. This method does though produce the least bias. The second method is to trigger an object that does not deposit significant energy in the calorimeter systems. In this case we choose the muon trigger with the lowest unprescaled p_T threshold. The muon trigger is chosen with some loose detector based isolation requirements to make sure it does not overlap with a jet, causing a discrepancy in the measurement of the calorimetric energy. The sample has a higher number of events due to the large amount of bandwidth given to the single object muon triggers at CMS. The use of a muon trigger also serves to increase the precision of the measurement of the performance of the Level-1 missing energy trigger, as the muons are not seen by the calorimeter system the \cancel{E}_T sample is enriched.

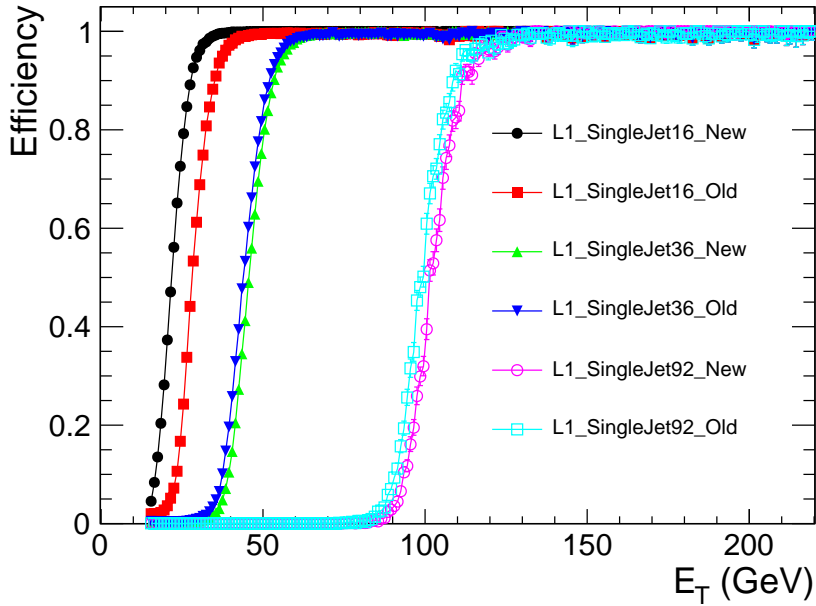


Figure 4.6.: Comparison of the performance of L1_SingleJet16, L1_SingleJet36 and L1_SingleJet92, when using the piecewise cubic corrections and using the new correction scheme. The difference in performance of the two is negligible above 36 GeV.

Figure 4.6 shows the performance of the piecewise cubic corrections (PWC) and the performance of the new corrections. The data was taken with the PWC enabled in the GCT hardware. The updated corrections were emulated in the bitwise reproduction of the GCT. This made an event by event comparison possible. At low E_T the new corrections turn on before the PWC corrections, if the new corrections were applied with no change to the trigger menu, the Level-1 trigger rate would rise. At a threshold of 36 GeV and higher, the performance of the two correction schemes is very similar. Due to the small change in observed performance and the ability to correct raw energies above 130 GeV, the new corrections were deployed online after the first machine development period of 2011 and are still online at the end of data taking in 2012.

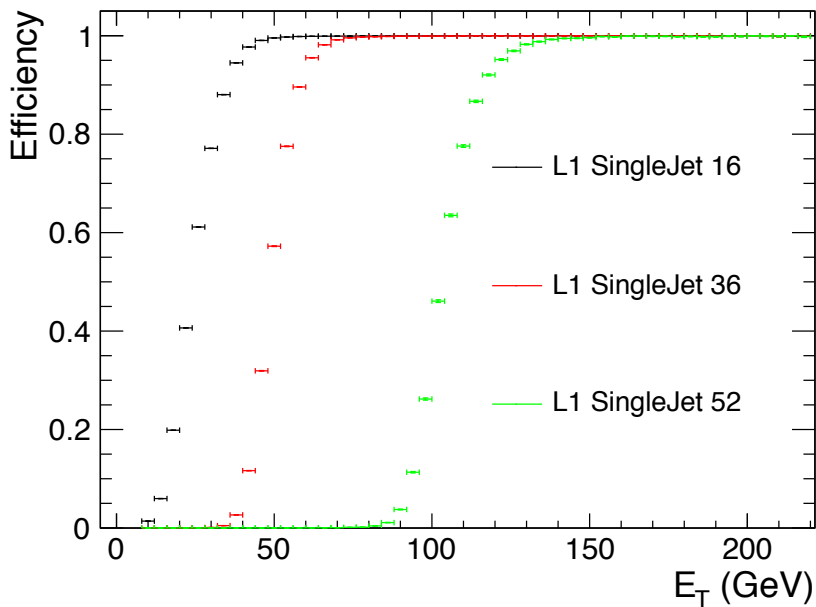


Figure 4.7.: Trigger efficiency of the L1_SingleJet16, L1_SingleJet36 and L1_SingleJet92 triggers, when using the new correction scheme deployed in the GCT hardware. The performance is slightly worse than that of the emulated triggers, where the plateau is reached at a higher offline energy, due to a change in pile-up conditions between the two data taking periods. Due to the shift to lower energies the purity of the trigger is lower and a higher trigger rate is observed for the same threshold value.

The performance of the updated corrections was then measured with data taken with the corrections applied in the GCT hardware. The reference sample was taken with a trigger requiring an isolated muon with $p_T > 24$ GeV (HLT_IsoMu24_v*). The performance of three example triggers is shown in Figure 4.7. The data collected and represented in Figure 4.7 has a peak mean pile up ($\langle PU \rangle$) of 16 interactions, this

is higher than the $\langle PU \rangle$ of approximately 8-10 present in Run2011A, on which the previous comparison was performed. The observed difference in the performance of the Level-1 single jet triggers as a function of pile-up is a case of concern, when data taking is underway at continually increasing luminosity and pile-up conditions.

The instantaneous luminosity in 2012 was predicted to be $5 \times 10^{33} \text{ cm}^{-2} \text{ s}^{-1}$, with $\langle PU \rangle \approx 32$. In order to study the effect on the trigger rate and efficiency a high pile-up, low instantaneous luminosity, LHC fill was taken in 2011.

The Level-1 single jet performance was studied in this run in terms of two offline object definitions. The first was the standard anti- k_t calorimeter jet reconstruction, the second was a set of anti- k_t calorimeter jets which were corrected for pile-up using the fastjet correction algorithm, which is further detailed in Section 5.1.1. The fastjet corrections remove the energy deposited by the secondary interactions, from the objects which are expected to come from the primary hard interaction, thus removing energy from the offline jets. The effect of these pile-up corrections on the Level-1 trigger performance is first studied under conditions with $\langle PU \rangle$ of 16, the performance of which has already been measured with respect to non pile-up corrected offline objects, as a sanity check. The results are shown in Figure 4.8 , the performance is measured with respect to `HLT_IsoMu24_v*`, in terms of both pile-up corrected and standard offline objects. As expected the performance in the two cases is very similar. The same comparison is shown for H_T in Figure 4.9, where the effect of the fastjet[53] corrections is more pronounced due to the sum over jets. The difference between the turn on points for the two offline quantities is on the order of 10 GeV under low pile-up conditions.

Due to the high pile-up fill being a specialised fill with low instantaneous luminosity, the high level trigger paths were disabled, instead Level-1 trigger pass-through paths were utilised to take the data. The Level-1 single muon pass though trigger is used to collect the reference sample. Otherwise the same analysis method is common between the two data sets. Figure 4.10 shows the difference in turn on for three example Level-1 single jet triggers when using standard calorimeter jets and fastjet corrected calorimeter jets. In the high pile-up conditions the switch to offline jets that are corrected for pile-up shifts the turn on point to lower vales of E_T , the magnitude of this effect reduces as the Level-1 trigger trigger threshold raises. This implies that the same offline performance as seen in the low pile-up conditions can be achieved by using the pile-up corrected offline objects and raising the Level-1 single jet trigger thresholds.

Figure 4.11 shows the same high pile-up comparison, but for the Level-1 H_T triggers. Due to the size of the sample the precision of this measurement is low. However the same trend of a shift to lower H_T values of the turn on point of the Level-1 triggers when using pile-up corrected offline objects is observed. This again implies that the Level-1 H_T trigger thresholds can be raised whilst preserving the same offline performance as during the low pile-up conditions.

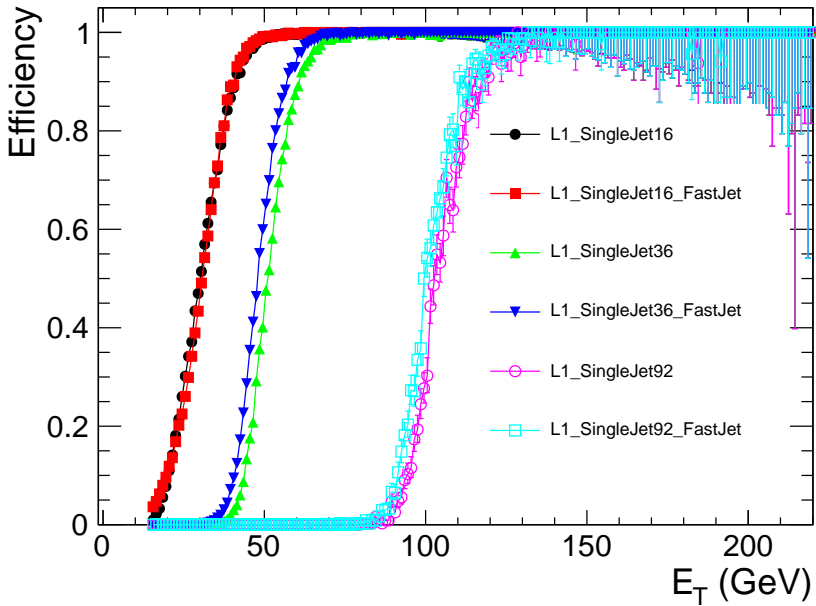


Figure 4.8.: Comparison of the performance of L1_SingleJet16, L1_SingleJet36 and L1_SingleJet92 triggers. Where $\langle PU \rangle = 16$. For two offline reconstruction methods: standard anti- k_t calorimeter jets and pile-up corrected anti- k_t calorimeter jets.

The performance of each of the Level-1 triggers is then reported to the analysis users so that high level trigger paths can be designed with the Level-1 constraints in mind. These measurements are also used when designing new Level-1 trigger menus where the requirement for taking the correct data has to be balanced against the total trigger rate of the Level-1 menu.

4.3. Level-1 Trigger Pile-up Mitigation

We have seen that the offline performance of the Level-1 hadronic triggers can be maintained when raising the trigger thresholds to deal with increased rate, when switching

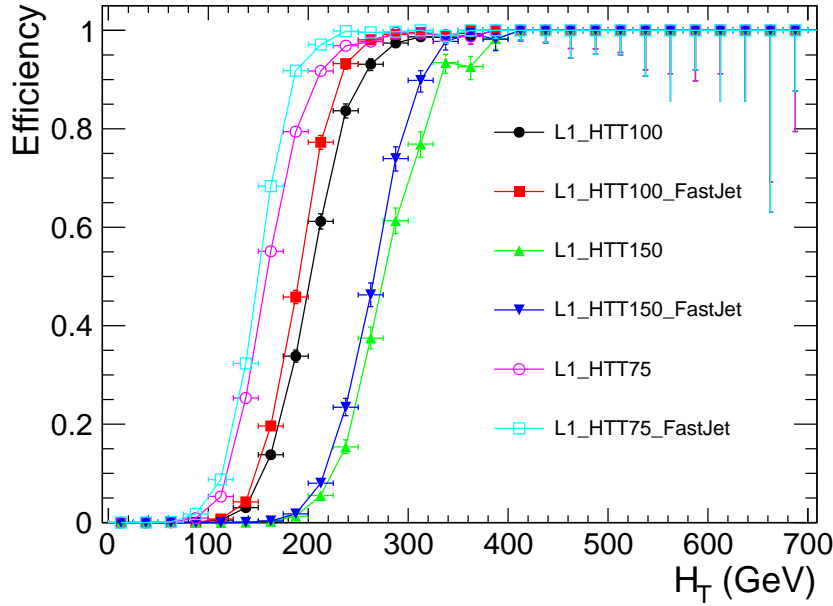


Figure 4.9.: Comparison of the performance of L1_HTT75, L1_HTT100 and L1_HTT150 triggers. Where $\langle PU \rangle = 16$. For two offline reconstruction methods: standard anti- k_t calorimeter jets and pile-up corrected anti- k_t calorimeter jets.

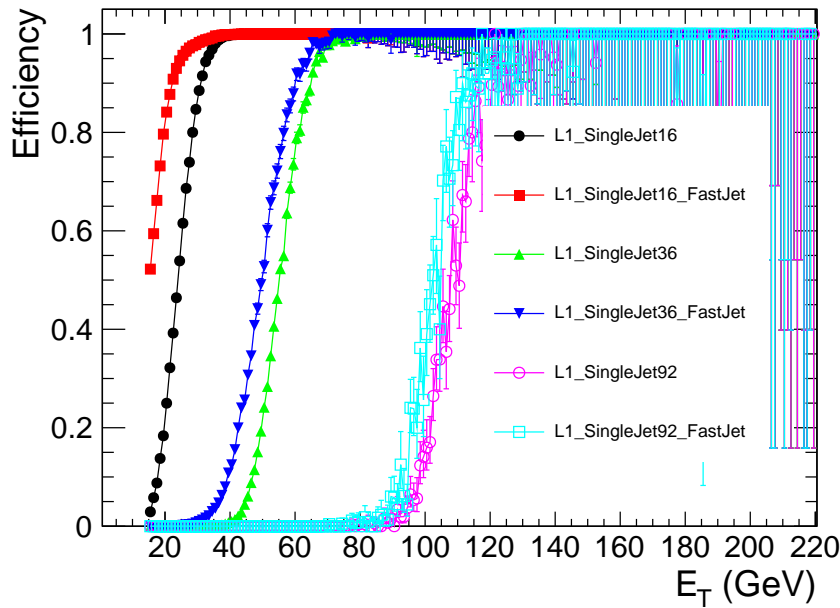


Figure 4.10.: Comparison of the performance of L1_SingleJet16, L1_SingleJet36 and L1_SingleJet92 triggers. Where $\langle PU \rangle = 36$. For two offline reconstruction methods: standard anti- k_t calorimeter jets and pile-up corrected anti- k_t calorimeter jets.

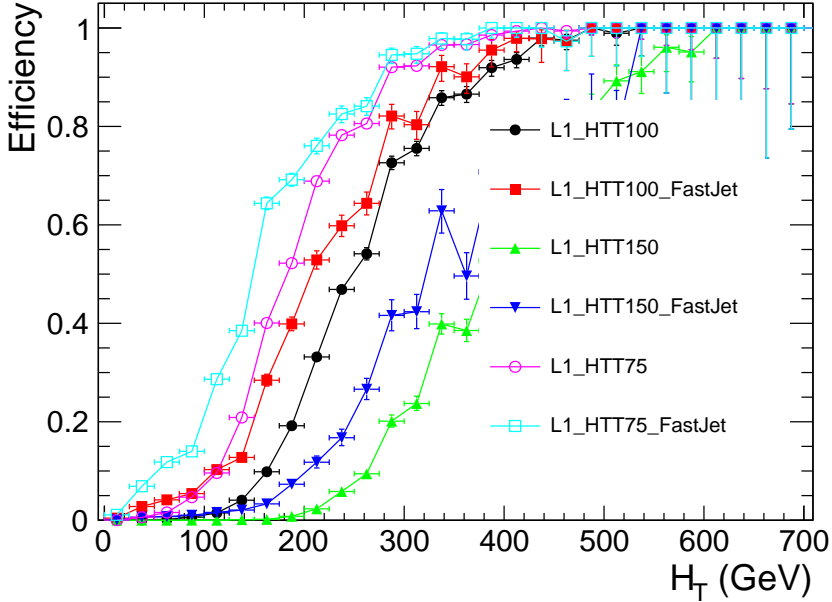


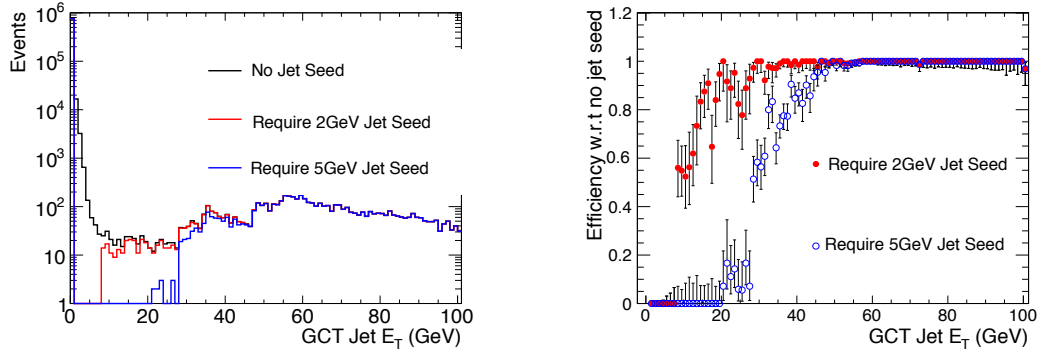
Figure 4.11.: Comparison of the performance of L1_HTT75, L1_HTT100 and L1_HTT150 triggers. Where $\langle PU \rangle = 36$. For two offline reconstruction methods: standard anti- k_t calorimeter jets and pile-up corrected anti- k_t calorimeter jets.

to pile-up corrected offline objects. Figure 4.14 shows the trigger cross section as a function of instantaneous luminosity for the L1_HTT150 trigger, which requires $H_T > 150$ GeV. Beyond a certain point raising thresholds causes a loss of performance. In this section we look at a method to reduce the effects of pile-up hadronic Level-1 triggers, by making an addition to the Level-1 jet finding algorithm.

In Section 4.1 the Level-1 jet clustering algorithm was described. The proposed change was to add a requirement that the seeding region has an energy threshold, in addition to the equality relations that are set up. The effects of applying a 2 GeV and a 5 GeV threshold are studied. This threshold is on the raw, uncorrected energy of the trigger regions and affects all Level-1 jets. The impact will be seen in the Level-1 jet triggers which use corrected energy and Level-1 H_T and \cancel{H}_T which are formed from uncorrected jets. The aim is to remove the events which are accepted due to pile-up, but not to remove physics events.

The triggers most affected by this change are the energy sum triggers as they sum many jets of low threshold, whereas the single object triggers are already cutting on high E_T objects.

Figure 4.12(a) shows the internal GCT uncorrected jet energy spectrum in high pile-up conditions, taken with the L1_SingleMu pass though triggers, however due to the presence of other triggers in the menu the distribution is not exponentially falling as would be expected. The three histograms are for: no application of jet seed threshold in black, where there are many low E_T jets; in red a 2 GeV seed requirement is made, the effect is to cut out all jets below 2 GeV and cut out jets with an energy up to approximately 35 GeV of uncorrected energy; the blue histogram shows the jet energy spectrum after applying a 5 GeV seed threshold, the effect is to remove all jets below 5 GeV and to cut out jets with energy up to 55 GeV. Figure 4.12(b) shows the efficiency with respect to the no seed sample for the two test seed thresholds. The removal of jets in the low energy region of the E_T spectrum due to the jet stemming from pile-up rather than collimated objects is where the advantage of applying a seed threshold is seen over simply raising the trigger thresholds, or raising the threshold of jets to be included in the Level-1 H_T or \cancel{H}_T calculation.



(a) GCT internal uncorrected jet E_T distributions for the same events with a 0, 2 or 5 GeV seed requirement.
(b) Efficiency of applying a requirement of 2 or 5 GeV with respect to no requirement.

Figure 4.12.: Effect of requiring a jet seed threshold on GCT internal jets.

To quantify the effects of the addition of the jet seed a low pile-up sample, where the effects are expected to be small, is studied in terms of rate reduction and efficiency change. The dedicated high pile-up fill is then studied in terms of rate reduction, due to the limited sample size of the high pile-up fill the change in efficiency on this sample is not studied. However due to the addition of energy from the secondary pile-up interactions the change in efficiency in the low pile-up sample is the worse case scenario.

Table 4.1 details the rate reduction with respect to the 0 GeV seed threshold for seed thresholds of 2 GeV and 5 GeV for three example triggers, these are:

Table 4.1.: Summary of rate reduction during low pile-up conditions.

Trigger	% rate reduction with a 2 GeV requirement	% rate reduction with a 5 GeV requirement
L1_HTT100	$3 \pm 11\%$	$3 \pm 11\%$
L1_QuadJet38	$0 \pm 0\%$	$15^{+6}_{-8}\%$
L1_Jet50	$0^{+0}_{-12}\%$	$15^{+9}_{-15}\%$

Table 4.2.: Summary of rate reduction during high pile-up conditions.

Trigger	% rate reduction with a 2 GeV requirement	% rate reduction with a 5 GeV requirement
L1_HTT100	$40 \pm 5.7\%$	$99^{+1}_{-50}\%$
L1_QuadJet38	$30 \pm 20\%$	$40^{+22}_{-24}\%$
L1_Jet50	$0^{+7}_{-0}\%$	$30^{+10}_{-12}\%$

- L1_SingleJet50, which requires at least one jet with $E_T > 50$ GeV within $|\eta| < 3.0$;
- L1_QuadJet38, which requires 4 jets with $E_T > 38$ GeV within $|\eta| < 3.0$;
- L1_HTT100, which requires that Level-1 $H_T > 100$ GeV.

The rate of L1_SingleJet50 is not affected by the requirement of a 2 GeV seed threshold and is reduced by 15% when a 5 GeV seed requirement is made. The L1_QuadJet38 trigger rate is reduced by the same amount as the single jet trigger, under low pile-up conditions for both seed thresholds. L1_HTT100 sees a 2% rate reduction when requiring a 2 GeV seed threshold and a 3% reduction in rate when requiring a 5 GeV seed.

Table 4.2 shows the rate reduction under high pile-up conditions with respect to the 0 GeV seed threshold requirement, for the same three example triggers as in the low pile-up case. The rate of L1_SingleJet50 is not reduced when making a 2 GeV seed requirement, when making a 5 GeV seed requirement the single jet 50 GeV rate is reduced by 30%. The rate of L1_QuadJet38 is reduced by 30% when requiring a 2 GeV seed and by 40% when requiring a 5 GeV seed. The rate of L1_HTT100 is reduced by 40% when requiring a 2 GeV seed threshold and when requiring a 5 GeV seed threshold the rate is reduced by $\approx 99\%$, however the statistical error on this prediction is large.

4.3.1. Effect on trigger efficiency

Section 4.3 shows that requiring a jet seed threshold substantially reduces the trigger rate at in high pile-up conditions.

However the aim of requiring a jet seed is to reduce rate, but not at the cost of physics. In this section we look at the effects of requiring a seed threshold, whilst requiring some loose, generic offline selection on the hadronic objects.

The change in efficiency is measured in low pile-up conditions where the least extra energy is added to the event. This gives a worse case estimate of the effect of requiring a jet seed on the offline efficiency.

Each offline reconstructed calorimeter jet must satisfy the following quality criteria:

- Pass loose calorimeter ID[55];
- $p_T \geq 30 \text{ GeV}$;
- $|\eta| \leq 3.0$;
- Matched to a Level-1 jet with $\Delta R \leq 0.5$.

4.3.2. Efficiency of H_T Triggers

Figure 4.13(a) shows the acceptance reduction after applying the two different jet seed thresholds. The distribution is the cumulative number of events passing a cut of $L1 HT^{cut}$ in bins of 25 GeV. Since H_T is the scalar sum of the jet p_T s in the event the value of Level-1 H_T is reduced as jets are removed from the calculation. To preserve efficiency the Level-1 trigger threshold will have to be reduced. When comparing to the high pile-up rate reduction in table 4.2 it can be seen that the trigger rate can be reduced by $\approx 20\%$ when requiring a 2 GeV seed threshold and reduced by $\geq 99\%$ when requiring a 5 GeV seed threshold, for a trigger threshold of 100 GeV.

4.3.3. Efficiency of Jet Triggers

Figure 4.13(b) shows the change in acceptance of jets in low pile-up conditions when the two different seed thresholds are required. The effect is of the order of a few percent for each of the thresholds. Requiring a 2 GeV seed reduces the efficiency for jets above

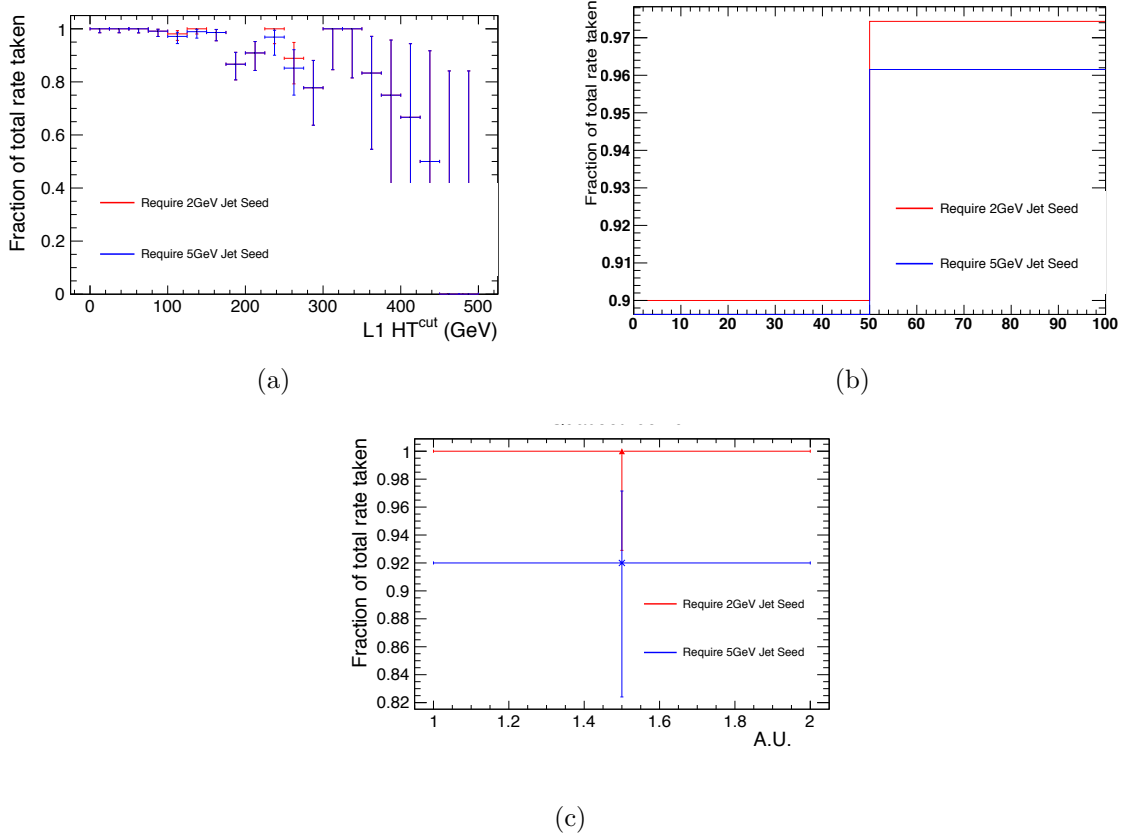


Figure 4.13.: Efficiency reductions for various Level-1 algorithms when applying a 2 or 5 GeV seed tower requirement, in low pile-up conditions. Figure (a) shows the efficiency reduction for H_T triggers at low pile-up in cut steps of 25 GeV. Figure (b) shows the efficiency reduction for jets within $|\eta| < 3$. and $p_T > 50\text{GeV}$. Figure (c) show the efficiency reduction for a quad jet trigger, with jet $|\eta| < 3$. and $p_T > 38\text{GeV}$.

50 GeV by $\approx 2.5\%$, whilst requiring a 5 GeV seed reduces the efficiency of the same jets by $\approx 4\%$.

4.3.4. Efficiency of MultiJet Triggers

Figure 4.13(c) shows that the effect of requiring a seed threshold of 2 GeV has no effect on the efficiency of the quad jet 38 GeV trigger and requiring a seed threshold of 5 GeV reduces the efficiency of the quad jet 38 trigger by 8%. The change in rate is dramatic in high pile-up conditions where for a 2 GeV seed threshold the rate is reduced by $\approx 30\%$ and by $\approx 40\%$ when requiring a 5 GeV seed. However it is to be noted that the sample

where this measurement has been made is of limited size, and so has a reasonably large statistical uncertainty of $\pm 8\%$

4.4. Summary

The effects of requiring a jet seed have been studied using the Level-1 trigger emulator on high and low pile-up samples. The studies show that requiring a jet seed of 5 GeV greatly reduces the rate of the H_T and Multi Jet triggers in high pile-up conditions, whilst not adversely affecting the data taking efficiency of these triggers.

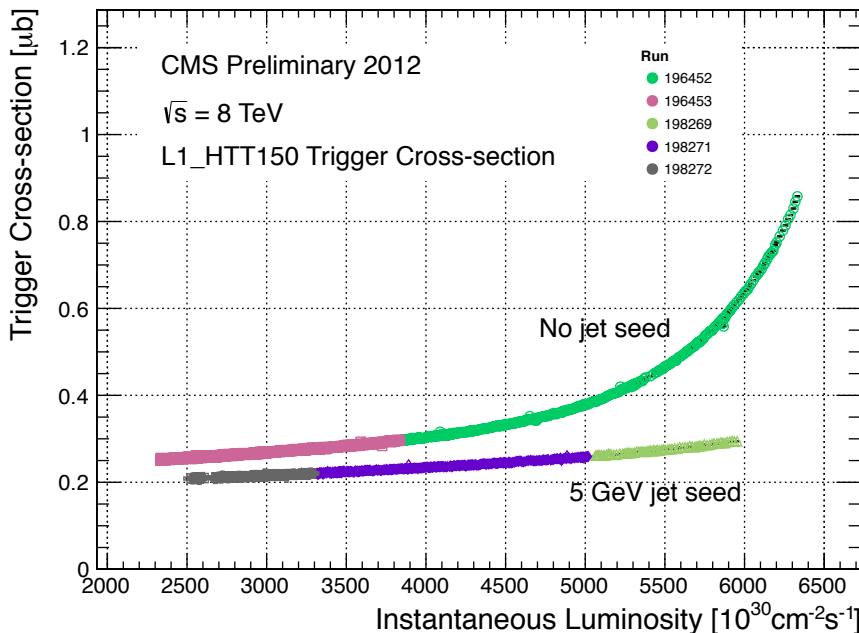


Figure 4.14.: Trigger cross section as a function of number of pile-up interactions. Showing that applying a 5 GeV jet seed threshold dramatically reduces the dependance of cross section on the instantaneous luminosity[54].

The cross section of L1_HTT150 has been measured with and without the addition of a jet seed threshold of 5 GeV as shown in Figure 4.14. Ideally the trigger cross section would be independent of the instantaneous luminosity and pile-up, Figure 4.14 shows that the addition of a 5 GeV seed threshold reduces the dependence on instantaneous luminosity of the trigger cross section. For the next run the Level-1 trigger hardware is being upgraded, this will enable event by event pile up corrections.

Chapter 5.

Reconstruction and Event selection

In this chapter the event reconstruction and selection for events of interest to the analysis is described. As previously described this analysis focuses determining the number of events containing missing energy in the pure hadronic channel and comparing this with the SM expectation. The SM sources of this missing energy come in two forms, one irreducible from standard model processes involving neutrinos which are not measured in the detector. The other from fake missing energy, introduced by miss-measurement, due to detector effects. The search variable α_T is constructed both as an offline discriminator and as an analysis specific trigger. It is the later of the two sources of missing energy, i.e. those from detector effects that α_T variable is designed to suppress. The performance of the trigger under different data taking conditions is measured after the final event selection, with respect to a well understood control region.

The first performance measurement is performed on the full 5 fb^{-1} of 7 TeV data collected in 2011, this data set is then used for the analysis presented in this thesis. The performance of a suite of upgraded α_T triggers is then measured on 11 fb^{-1} of 8 TeV data which was collected during the 2012 LHC run. These performance measurements were used in the analysis presented in [56].

5.1. Event selection

In order to select events for the hadronic signal sample and the muon and photon control samples a common set of section cuts is defined. In this section the objects are defined as are the flow of the analysis cuts and filters.

5.1.1. Preselection of hadronic objects

Hadronic showers are clustered into objects which from now on will be referred to as jets. These jets are formed from the energy deposits recorded in the calorimeter towers. Individual jets are clustered using the anti- k_t algorithm with a clustering parameter of 0.5[57], for high p_T jets this produces cone like jets, for low p_T jets deviations from the circular geometry are allowed, as shown in Figure 5.1.

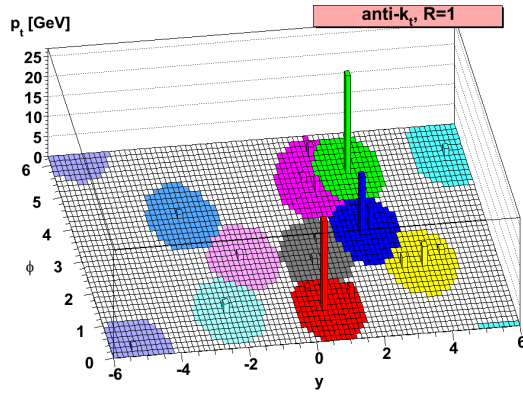


Figure 5.1.: Simulated hadronic objects clustered into jets using the anti- k_t jet clustering algorithm.

The jets have their raw energies corrected based on their position and momentum to establish a uniform relative response in η and a calibrated absolute response in transverse energy E_T , with an associated uncertainty of between 2% and 4% dependent on E_T and η [58]. Figure 5.2 shows the absolute jet energy scale uncertainty as a function of the jet p_T for the jets considered in this analysis.

It is also possible to correct the raw energies of the jets for pile-up. Pile-up causes energy from secondary interactions to be added to the event, this energy is distributed uniformly throughout the detector. Two forms of pile-up corrections are used in CMS to correct the energies of calorimeter jets. The first is an offset correction, the raw energy has a constant energy removed throughout the detector based on the number of primary vertices in the event. The second method is to calculate per event, the average energy deposited in each calorimeter tower using the `FastJet`[53, 60] jet clustering package, this quantity is referred to as ρ and is also used to correct the isolation variables for electrons, muons and photons.

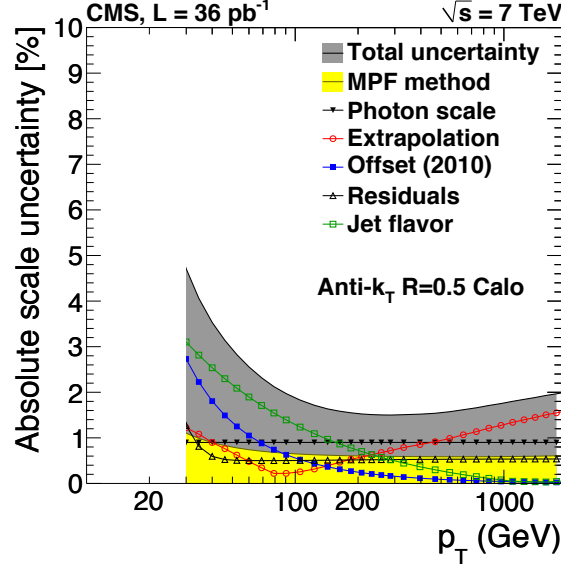


Figure 5.2.: Absolute jet energy scale uncertainty as a function of jet p_T for anti- k_t -calorimeter jets[59].

The jets considered in the analysis are not corrected for pile-up, as during the data taking period the mean number of pile up vertices was at maximum 16 per bunch crossing, this means that the effects of the pile up corrections were low and in many cases the removal of energy from the calorimeters caused events to be come more unbalanced. Each jet is required to have $E_T > 50 \text{ GeV}$, the highest E_T jet in the events is required to be within the tracker acceptance ($|\eta| < 2.5$) and the sub leading jet is required to have $E_T > 100 \text{ GeV}$. In the lowest two offline H_T bins the jet thresholds are scaled to preserve the jet multiplicity, for the bin $275 \text{ GeV} < H_T < 325 \text{ GeV}$, the jet threshold is 36.6 GeV and the sub leading jet threshold is 73.3 GeV . In the bin $325 \text{ GeV} < H_T < 375 \text{ GeV}$, the jet threshold is 43.3 GeV and the sub leading jet threshold is 86.6 GeV . This scaling of the jet thresholds is implemented to conserve the allowed jet multiplicities in each of the search bins, which in turn preserves the relative contribution of each of the background sources.

The quantities H_T and $\#_T$ are then formed from these jets.

5.1.2. Electrons

Two complementary algorithms are used at the track seeding stage of the electron reconstruction. Tracker driven seeding which is more suitable for low p_T ($p_T < 5 \text{ GeV}$) electrons and ECAL driven seeding, which starts at the ECAL and works back towards

the interaction point. The ECAL driven seeding starts by creating superclusters[61] which contain information on the lateral shower shape in the η direction of the electron or photon shower and the spread of energy deposits in the ϕ plane for electrons, due to the radiation of photons by the electron in the CMS magnetic field. Track seeds from inner tracking layers and electron track are then build from these track seeds. The trajectories are reconstructed using a dedicated modelling of the electron energy loss and fitted with a Gaussian Sum Filter[62]. For the purpose of the analysis an object is defined as an electron if it has $p_T > 10 \text{ GeV}$, $|\eta| < 2.5$ and passes standard criteria for 95% selection efficiency[63]. Any event containing an identified electron is vetoed.

5.1.3. Muons

Muon reconstruction at CMS is designed to be regional meaning that the full reconstruction sequence can be run at both the HLT and offline. Regional reconstruction only performs the reconstruction in a small part of the detector meaning that the time taken is short. As an example the amount of information required to reconstruct a muon in the silicon tracker is less than one percent of the entire tracker read out. The regions which are reconstructed at the HLT are seeded by the muon candidates produced by the Level-1 trigger even if these muons did not cause the issue of the Level-1 accept. Global muon reconstruction uses information from both the standalone muon system and from the silicon tracker and performs a fit to the individual detector hits. Figure 5.3 shows the muon momentum resolution for muons reconstructed using either the muon system only, the tracker only or the global muon reconstruction.

Signal events are vetoed if they contain a muon with $p_T > 10 \text{ GeV}$ and $|\eta| < 2.5$ that passes the standard quality criteria for muon identification that gives 95% selection efficiency[64]. Two separate muon control samples are defined, one requiring exactly one muon with $p_T > 10 \text{ GeV}$, the second requiring two oppositely charged muons where the invariant mass sums to the Z mass.

5.1.4. Photons

Photons are reconstructed in the ECAL using the same methods as used to reconstruct electrons. However the tracking requirements are inverted. For photons which do not convert in the tracker a supercluster energy deposit is required with no associated electron track, for photons which undergo pair production in the tracker material the tracks

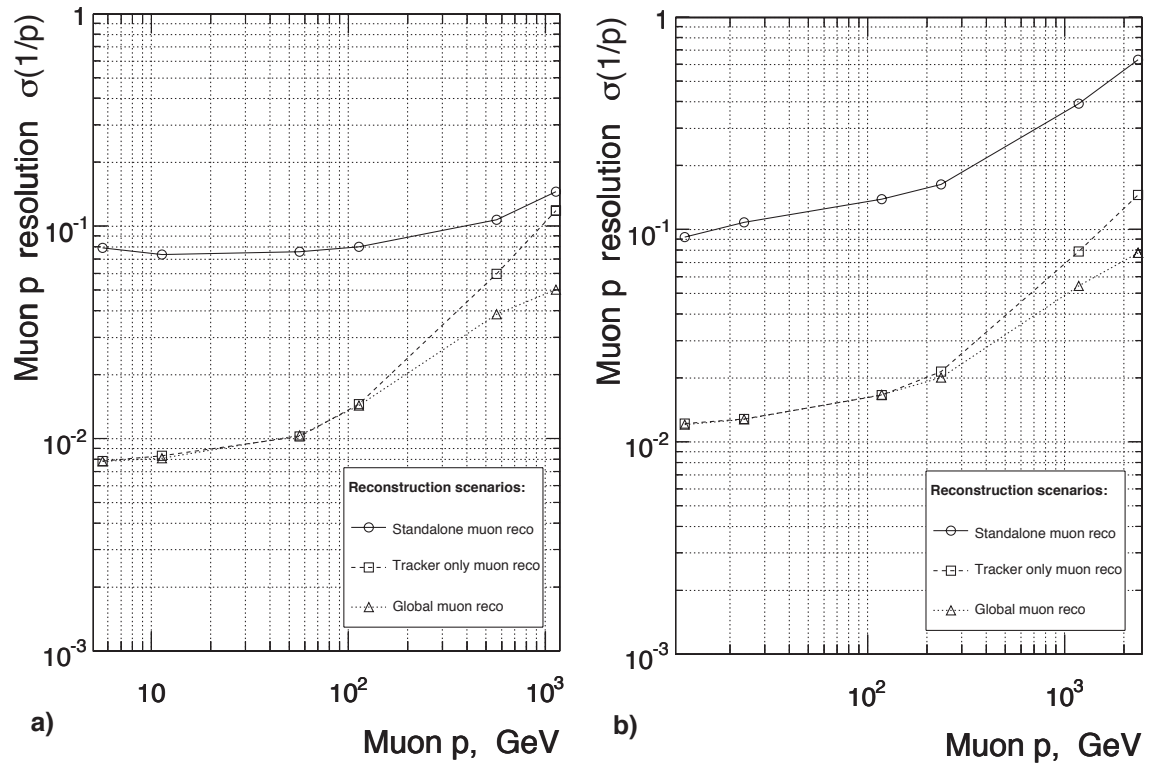


Figure 5.3.: Resolution of $(1/p)$ versus p for standalone, global and tracker-only reconstruction.
 a) Barrel, $\eta = 0.5$; b) Endcap, $\eta = 1.5$ [61].

associated with the superclusters do not originate from the interaction vertex, instead they appear in a layer of the tracker. For unconverted photons the ratio of the energy deposited in the central ECAL crystal to the energy of the surrounding 3×3 group of ECAL crystals is used as an identification variable. Signal events are vetoed if they contain a photon with $E_T > 25$ GeV, $|\eta| < 2.5$ and that passes ID requirements[65]. A requirement of exactly one photon with $E_T > 150$ GeV within $|\eta| < 1.45$ is made for the photon control sample.

5.1.5. Resolving object overlaps

The CMS software attempts to identify each object in the detector, at times this results in overlapping offline objects. For example a muon reconstructed inside a jet. To avoid double counting of objects a cleaning scheme is set up. The object with the tightest ID is declared the true object and the overlapping object is merged and the energy recomputed. This is referred to as “Cross Cleaning”.

5.2. The α_T variable

The α_T is variable inspired by Ref [66] and was expanded first to consider transverse topologies and later expanded to multi-jet systems by members of the CMS collaboration in Refs [67, 68]. The purpose is to provide variable that can be used to reduce the fraction of QCD from the final event selection. To do this the balance of the QCD system is exploited.

For di-jet systems α_T is defined as:

$$\alpha_T = \frac{E_T^{j_2}}{\mathcal{M}_T} \quad (5.1)$$

where $E_T^{j_2}$ is the transverse energy of least energetic of the two jets and \mathcal{M}_T is defined as:

$$M_T = \sqrt{\left(\sum_{i=1}^2 E_T^{ji}\right)^2 - \left(\sum_{i=1}^2 p_x^{ji}\right)^2 - \left(\sum_{i=1}^2 p_y^{ji}\right)^2}. \quad (5.2)$$

For a perfectly measured di-jet system with $E_T^{j_1} = E_T^{j_2}$ and where the jets are opposite in azimuth (ϕ), $\alpha_T = 0.5$. For events with back to back jets where one is missmeasured $\alpha_T < 0.5$. However a large number of beyond the standard model signals predict many jets in the final state. α_T can be generalised to work with an arbitrary number of jets in the following way. The variables H_T and \cancel{H}_T are constructed as:

$$H_T = \sum_{i=1}^n E_T^{jet_i}, \quad (5.3)$$

$$\cancel{H}_T = \left| \sum_{i=1}^n \vec{p}_T^{jet_i} \right|, \quad (5.4)$$

for jets above some predefined threshold in E_T which is common for all jet-based quantities. The multi-jet system is reduced to a pseudo di-jet system, where the jets are clustered into two objects around the leading and sub-leading jets, forming two large jets. The individual jet E_T values are summed, with the final configuration being chosen to have the minimum difference in energy (ΔH_T) between the two new jets. This simple clustering criteria provides the best separation between missmeasured events and those with real \cancel{E}_T , this is shown in Ref [68].

α_T is then defined as:

$$\alpha_T = \frac{H_T - \Delta H_T}{2\sqrt{H_T^2 - \cancel{H}_T^2}} \quad (5.5)$$

Figure 5.4 shows the α_T distribution for both data and simulated background samples after all full event selection which is described in detail later in this chapter. The QCD multi-jet background is negligible above an α_T value of 0.55, whereas the standard model processes which involve real \cancel{E}_T exist at all possible values of α_T . Values of α_T in the range $0.5 < \alpha_T < 0.55$ arise in multi-jet QCD due to jets falling below threshold, large stochastic fluctuations or catastrophic missmeasurement due to detector element failures. It is to be noted that the discrepancy between data and simulation for $\alpha_T \leq 0.55$ is due to no trigger emulation being applied to the simulated background samples. The trigger emulation is omitted due to the changing thresholds throughout the data taking period and the centralised production of the Montecarlo (MC) containing only one threshold value emulated on the HLT level objects. However as this region is not considered for the analysis this does not effect the final result.

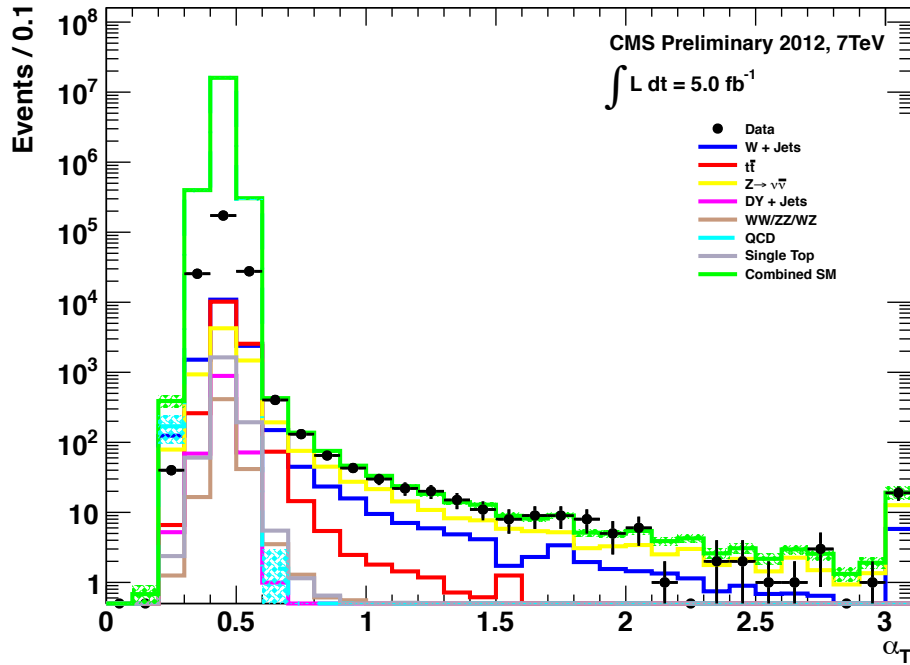


Figure 5.4.: α_T distribution for background and data for the region $H_T > 375$ GeV. Trigger emulation is not applied in the simulated background which leads to the discrepancy in the region $\alpha_T \leq 0.55$. The QCD multi-jet background is reduced to less than one event.

5.3. Common Analysis cuts

- **Good run selection**, All detector subsystems on, CMS in “Physics Declared” mode and all physics object groups have certified the runs and luminosity sections. This removes any events where the sub-detectors were in an error state or events from before the tracker was switched to high voltage mode.
- **P.K.A.M (Previously Known As Monsters) filter**, these events are caused by beam-gas interactions close to CMS, which cause a shower of particles to enter the pixel detector along the beam line, resulting in a large proportion of the pixel detector to record hits. If a large number of non-vertex related hits are recorded the event is vetoed.
- **Vertex Selection** requires at least one vertex with at least four associated tracks, within a cylinder of radius 2 cm and length 48 cm, centred at $Z = 0$ of the CMS detector.

- **Hadronic barrel and end-cap noise filter**, this filter removes events where strips of towers in the hadronic calorimeters record energy from electrical noise, mimicking large, unbalanced energy deposits.
- **Vertex $p_T/H_T > 0.1$** , removes events where the sum of the p_T of all tracks from all good vertices is less than 10% of the energy deposited by jets in the calorimeters. This cut is designed to remove events with a tracking failure, which would otherwise pass the calorimeter only event quality requirements.
- **Masked ECAL channel filter:** Approximately 1% of the ECAL crystals are masked, or have readout failures. To avoid selecting events with large energy missmeasurement, a topological cut was devised. The first step is to calculate $\Delta\phi^*$ for each jet (\vec{j}) in the event, where:

$$\Delta\phi^* = \Delta\phi \left(\vec{E}_T + \vec{j}, \vec{j} \right). \quad (5.6)$$

Which gives a measure of the missmeasurement of a jet, if $\Delta\phi^*$ is small, the missing energy points along the jet in the ϕ direction. By selecting the miss measured jet, full position information is preserved. If any jet has $\Delta\phi^* < 0.5$, the number of masked ECAL crystals within $\Delta R < 0.3$ are summed, if there are more than 10 masked crystals adjacent to the jet, the event is vetoed.

- **$R_{miss} < 1.25$:** The total hadronic energy in an event is required to be greater than 275 GeV which is well above the transverse energy threshold of 50 GeV for each jet. However several jets falling below this threshold can sum to a significant quantity of energy which is not considered by the event level variables. This is shown in Figure 5.5, here the missing energy calculated from jets in the range $10 \text{ GeV} < E_T < 50 \text{ GeV}$ is shown, whilst requiring that $\cancel{E}_T < 20 \text{ GeV}$. This shows that for a well balanced event the jets below threshold can carry greater than 100 GeV of ignored energy. R_{miss} is defined as $\cancel{H}_T/\cancel{E}_T$ and can be used to single out events where the inclusion of lower momentum jets does significantly improve the balance of the event. Figure 5.6 shows, for two H_T regions, the R_{miss} distribution after the application of the full cut flow, including α_T . QCD contamination is visible in the signal sample for $R_{miss} > 1.25$.

This selection and set of object definitions define the common selection, on top of this an α_T cut is applied, the events satisfying these requirements are then binned in 8 H_T bins, these are 275 GeV - 325 GeV, 325 GeV - 375 GeV, 375 GeV - 475 GeV, 475 GeV -

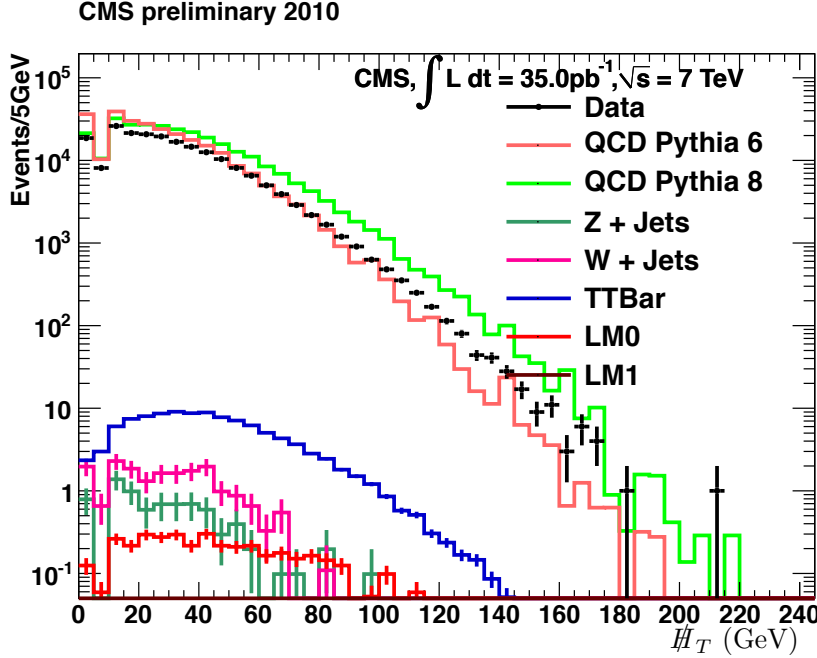


Figure 5.5.: \cancel{H}_T from jets with $10 \text{ GeV} < E_T < 50 \text{ GeV}$ in events with $H_T > 350 \text{ GeV}$ and $\cancel{E}_T < 20 \text{ GeV}$ in 35 pb^{-1} of data. LM0 and LM1 are two low mass SUSY benchmark points which are included to show that the \cancel{H}_T in these events is highly correlated with the \cancel{E}_T in the event.

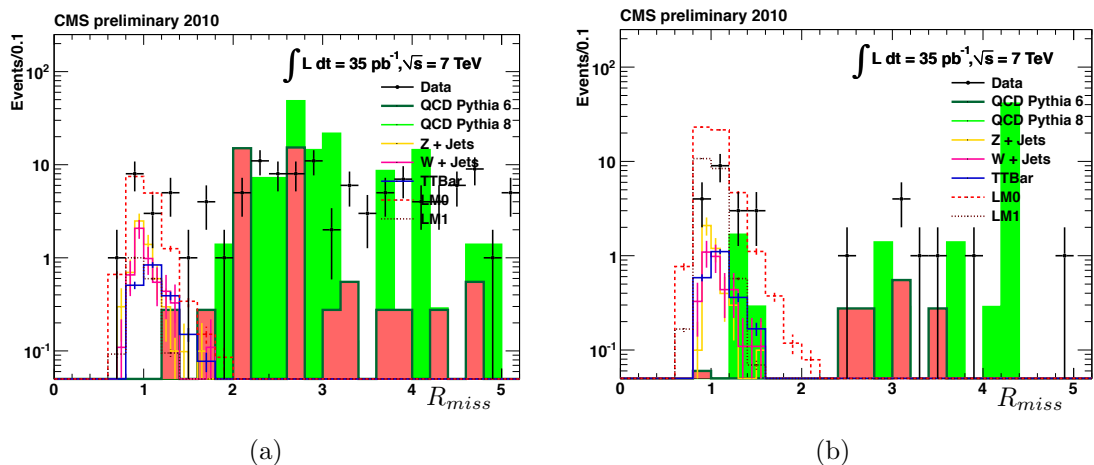


Figure 5.6.: (a) R_{miss} distribution for events in the $250 \text{ GeV} < H_T < 350 \text{ GeV}$ region, where due to the low H_T requirement QCD contamination is enriched.

(b) R_{miss} distribution for events in the $H_T > 350 \text{ GeV}$ region, QCD contamination occurs at $R_{miss} > 1.25$.

575 GeV, 575 GeV - 675 GeV, 675 GeV - 775 GeV, 875 GeV - 7 TeV. This binning was chosen with regard to the H_T trigger thresholds, with a gap of 25 GeV given to account for the turn on of the H_T of the trigger. The next section describes the triggers used to collect the data samples.

5.4. High Level Triggers for the α_T analysis

The CMS trigger system has been discussed in Section 3.7 and Chapter 4, however details of analysis specific trigger paths were not discussed. During 2011 the first α_T specific trigger was designed and deployed online. The trigger was then upgraded for the higher luminosity and energy of the 2012 data taking period.

The trigger takes advantage of two variables, H_T and α_T . At low H_T a high α_T value cuts the trigger rate, whereas at high H_T where the trigger rate is lower the α_T requirement can be loosened.

Due to the scaling of jet thresholds in the lowest offline H_T bins as detailed in Section 5.1 using a fixed jet threshold would cause inefficiency in the lowest offline H_T bins. To overcome this the trigger level α_T calculation is performed iteratively for all jets above a predefined threshold. This raises the total number of accepted events whilst adding the benefit of being efficient for any offline jet threshold above the minimum trigger jet threshold.

Due to concerns on the time taken to perform the ΔH_T minimisation at the trigger and time constraints enforced on trigger menu development, the first implementation calculated α_T for the first 3 jets. For higher jet multiplicities the variable β_T is calculated, where the jet minimisation stage is omitted, this causes a higher acceptance due to the balance of the event not being considered by the trigger algorithm. The trade off between purity and rate along with the time constraints is acceptable.

$$\beta_T = \frac{H_T}{2\sqrt{H_T^2 - \cancel{E}_T^2}} \quad (5.7)$$

this gives us the relation:

$$\alpha_T \leq \beta_T. \quad (5.8)$$

The decision flow is shown in Figure 5.7 and explained in detail below.

When a Level-1 accept is issued the trigger bits that fired are checked, if the event fires a Level-1 muon trigger it is passed to the HLT muon triggers where only muon reconstruction is performed, reducing the reconstruction time. The α_T triggers are seeded on the lowest threshold unprescaled L1 H_T trigger, during 2011 this was L1_HTT100, which requires 100 GeV of uncorrected H_T in the event. Any events issuing a L1 accept and passing L1_HTT100 undergo calorimeter jet reconstruction, the reconstruction algorithm is detailed in Section 5.1.1.

Once the jets have been formed the trigger filter is entered. Initially the first two jets ranked by E_T , are considered, H_T and α_T are calculated, if both pass the trigger thresholds the event is accepted and the full detector readout is performed. If either H_T or α_T is below threshold, the next jet in E_T order is added, if the jet list contains more than 3 jets then the β_T approximation is used. All jets in the event are added until either the event is accepted, or there are no more jets to be added above 40 GeV.

The effect of switching to the β_T approximation is to accept events that have missing energy due to missmeasurement, when calculating α_T offline these events have values of $\alpha_T < 0.5$. This introduces an impurity to the trigger and costs rate for events that will not be considered in the offline analysis.

5.4.1. Trigger efficiency measurement

The performance of the α_T trigger suite is measured with respect to a reference sample collected using the muon system. This allows the measurement of efficiency of both the Level-1 seed trigger and the higher level trigger at the same time, as different sub-systems are used to collect the reference and the signal triggers. This is due to the exclusive use of calorimeter jets in the α_T trigger, if more complicated reconstruction methods which produce an event hypothesis were used then muons would at HLT level be considered as jets. Whereas during calorimeter only reconstruction, muons are not considered and the p_T of any muons in an event is viewed as missing energy.

The selection for the trigger efficiency measurement is the same as listed in Section 5.1 with the requirement of exactly one well identified muon with $p_T > 45$ GeV, the sum of the \cancel{E}_T in the event and the muon must add to the transverse W mass as defined in Equation (5.1). Finally the muon must be separated by at least 0.5 in ΔR to the closest

jet. This avoids the muon energy changing the energy of the jet offline when the cross cleaning is applied.

Due to the increase in luminosity over the running period the trigger thresholds were increased, to ensure constant rate throughout the year and the trigger version numbers were increased each time the trigger menu was updated. The list of triggers considered and the triggers used to collect the respective reference sample are listed in Tables B.1 and B.2.

The efficiency of each trigger version is measured in the required H_T bins, the total efficiency for each H_T bin is then calculated by combining the individual efficiencies using a weighted sum based on the fraction of the total luminosity of the sample that each version carries. This accounts for the change in running conditions during the data taking period and the criteria that the trigger suite takes constant rate. The higher trigger versions and thresholds generally represent more integrated luminosity due to the evolution of running conditions with time.

The efficiency is measured as a function of the cumulative number of events, i.e. the efficiency at each point on the x axis is the measured efficiency if a cut were applied offline at that cut value.

As an example, the efficiency of each trigger used in the $275 \text{ GeV} < H_T < 325 \text{ GeV}$ bin is measured and then combined to give the total efficiency. The cumulative efficiency curves for each trigger seeding the lowest bin is show in Figures 5.8 and 5.9. Note that some of the triggers are repeated, due to the reference trigger version incrementing and the signal trigger not.

These are then combined to give Figure 5.10. The efficiency at a cut of $\alpha_T > 0.55$ is $83.3^{+0.5\%}_{-0.6\%}$. The loss in efficiency comes from the disparity between the minimum thresholds for jets to enter the H_T and α_T calculations at the HLT and those used in the analysis. The trigger jet E_T threshold is 40 GeV whereas the analysis jet E_T threshold in this bin is 36.6 GeV. The triggers used to take data at the end of this running period also have an α_T threshold above the analysis cut of $\alpha_T > 0.55$, which again causes an inefficiency. The list of efficiencies for each H_T bin are shown in Table 5.1. The trigger efficiencies are measured to better than one percent and this information is used in the final analysis.

The α_T triggers were upgraded for the increased instantaneous luminosity and pile-up conditions expected during the 2012 data taking period. The first stage was to implement

H_T range	Trigger efficiency (%)
275 GeV – 325 GeV	$83.3^{+0.5}_{-0.6}$
325 GeV – 375 GeV	$95.9^{+0.7}_{-0.9}$
375 GeV – 475 GeV	$98.5^{+0.5}_{-0.9}$
475 GeV – 7 TeV	$100.0^{+0.0}_{-4.8}$

Table 5.1.: Efficiencies of the α_T triggers used in the 7 TeV α_T analysis on 5 fb^{-1} of LHC data.

the full α_T calculation for each addition of a new jet, this change increases the purity of the trigger, meaning that for the same threshold the rate taken is lower than that of the previous algorithm. This allows the thresholds to be kept low, whilst not increasing the overall trigger rate.

The second upgrade was to switch to pile-up corrected jets at the HLT, this change keeps the trigger cross section linear as a function of instantaneous luminosity.

The third choice was to design a trigger suite that could run for the entire 2012 data taking period, without changing the trigger thresholds, this was done to make the measurement of the efficiency simpler.

The trigger thresholds used are presented in Table B.3, due to the constant thresholds in H_T and α_T throughout the run, the versioning of the triggers is excluded from this table. The efficiency of the triggers is measured for 11.7 fb^{-1} of LHC data taken at a centre-of-mass energy of 8 TeV the efficiencies were measured for the analysis documented in [69]. A single-muon trigger is used to collect the reference sample, the threshold of this trigger was unchanged during the data taking period, the path selected requires at least one muon with $p_T > 24 \text{ GeV}$ that is not overlapping with any other object in the detector(`HLT_IsoMu24_v*`). The same method is used as for the 2011 trigger efficiency measurement. However the offline jets are corrected for pile up using the fastjet corrections, to stay inline with the HLT object definitions.

Figure 5.11 shows the efficiencies of the four individual triggers that seed the 275 GeV–325 GeV H_T region for 11.7 fb^{-1} of 8 TeV LHC data, Figure 5.12 shows the combined cumulative efficiency of the 2012 trigger suite.

H_T range (GeV)	Trigger efficiency (%)
275 GeV – 325 GeV	$89.6^{+0.4}_{-0.4}$
325 GeV – 375 GeV	$98.6^{+0.2}_{-0.3}$
375 GeV – 475 GeV	$99.4^{+0.2}_{-0.3}$
475 GeV – 8 TeV	$100.0^{+0.0}_{-0.5}$

Table 5.2.: Efficiencies of the α_T triggers at a centre of mass energy of 8 TeV α_T measured in 11.7 fb^{-1} of LHC data.

The two trigger suites have very similar offline performance with 100% efficiency in the analysis bins above 475 GeV and high efficiency in the lower bins. To quantify the difference in performance between the two algorithms the purity is defined as the number of events passing the trigger that pass the offline α_T requirement at the same threshold as the trigger requirement divided by the total number of events accepted by the trigger. The purity of each trigger algorithm is measured for an example trigger with a H_T threshold of 350 GeV and an α_T threshold of 0.52. The 2011 trigger which only performs the full α_T calculation for jet multiplicities of less than four has a purity of 48%, which means a quarter of all rate taken by the trigger is used in the offline analysis. The 2012 trigger which performs the full α_T calculation for all jet multiplicities has a purity of 75%. This 25% increase in purity translates into a 25% rate reduction for the same trigger threshold when changing to the full α_T calculation for all jet multiplicities, thus enabling the trigger thresholds to be kept at the same or lower thresholds in the 2012 run as in the 2011 run.

5.5. Including B-tagging in the α_T analysis.

As discussed in Chapter a multitude of SUSY final states exist, following the naturalness argument that the super partner to the top quark should be the lightest SUSY particle, and that these stops decay in a similar way to the SM top quark. I.e. to topologies involving bottom quarks. The extra discrimination power of counting the number of bottom quarks in the final state should not be ignored. This is also due to the relatively low production of bottom quarks along with missing energy from SM processes. From the experimental side, due to the decay lifetime of the bottom quark, tagging these objects using the CMS tracking system by virtue of the displaced secondary decay vertex is achievable at high reconstruction efficiency. Jets are tagged as originating from a

b-quark decay via the identification of a displaced vertex as it takes the b-quark a finite amount of time to decay, during this time the quark which is not produced at rest travels away from the initial interaction point, where upon decaying a secondary decay vertex is created. The algorithm used to classify these jets as containing a b-quark is the Combined Secondary Vertex (CSV) tagger. The “Medium” working point is used in the analysis, which requires a cut of > 0.679 on the CSV value. This results in a gluon/light quark mis-tag rate of 1% (where “light” quarks are u, d and s-types), and an efficiency for tagging b-quark jets in the range 60 – 70%[70] is achieved, this efficiency depends on the jet p_T . The discriminator is supported by the CMS b physics object group[71] and its performance is well understood. The Monte Carlo miss tag and identification rates are re-weighted to agree with data observations, thus provide an accurate background prediction for the high multiplicity b-tagged bins which are dominated by the mistag of light quarks as b-quarks.

The measurements of the trigger efficiencies are transparent to the number of b-tags in the event as no selection requirements are imposed at trigger level.

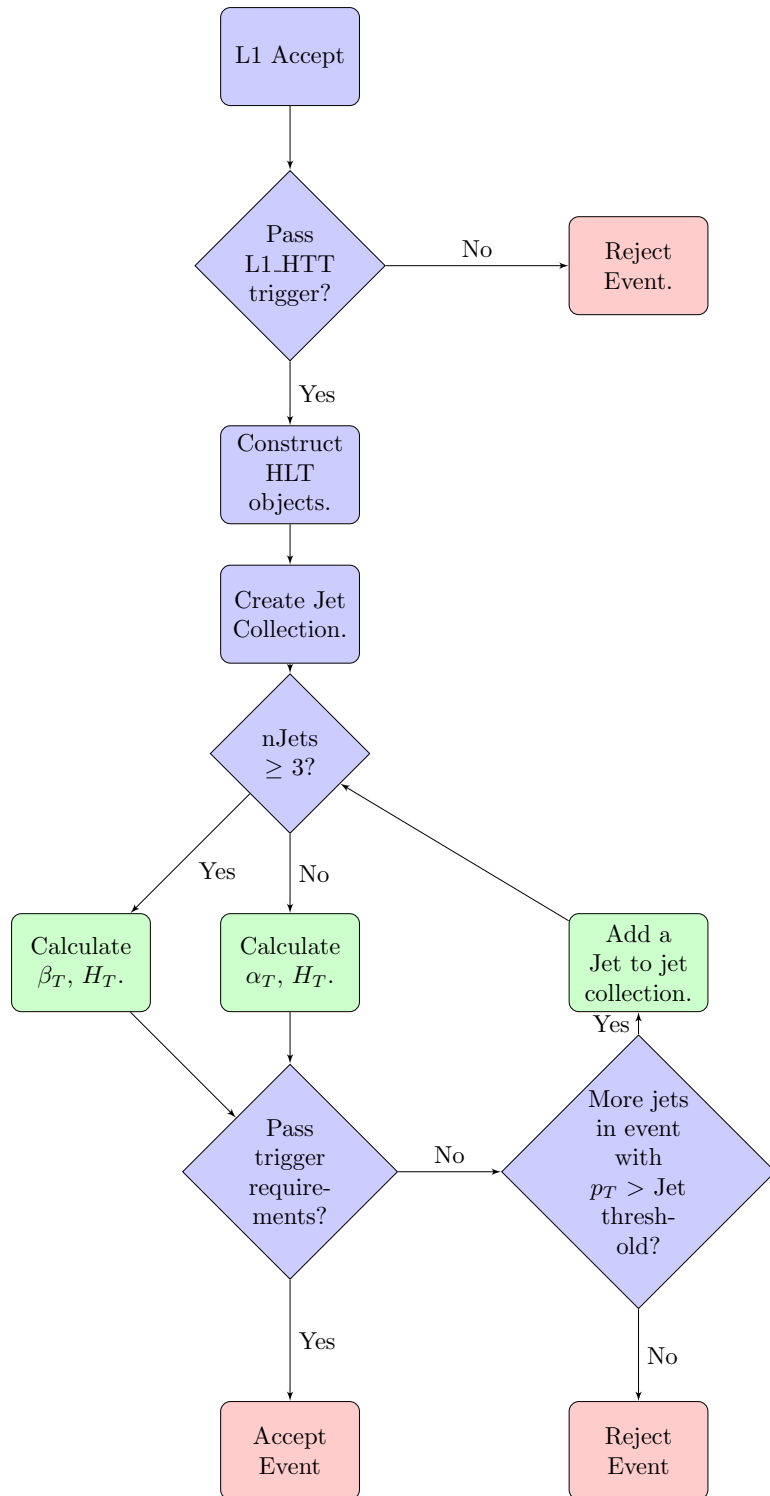


Figure 5.7.: Flow chart representing the steps taken to make a trigger decision using the α_T trigger algorithm.

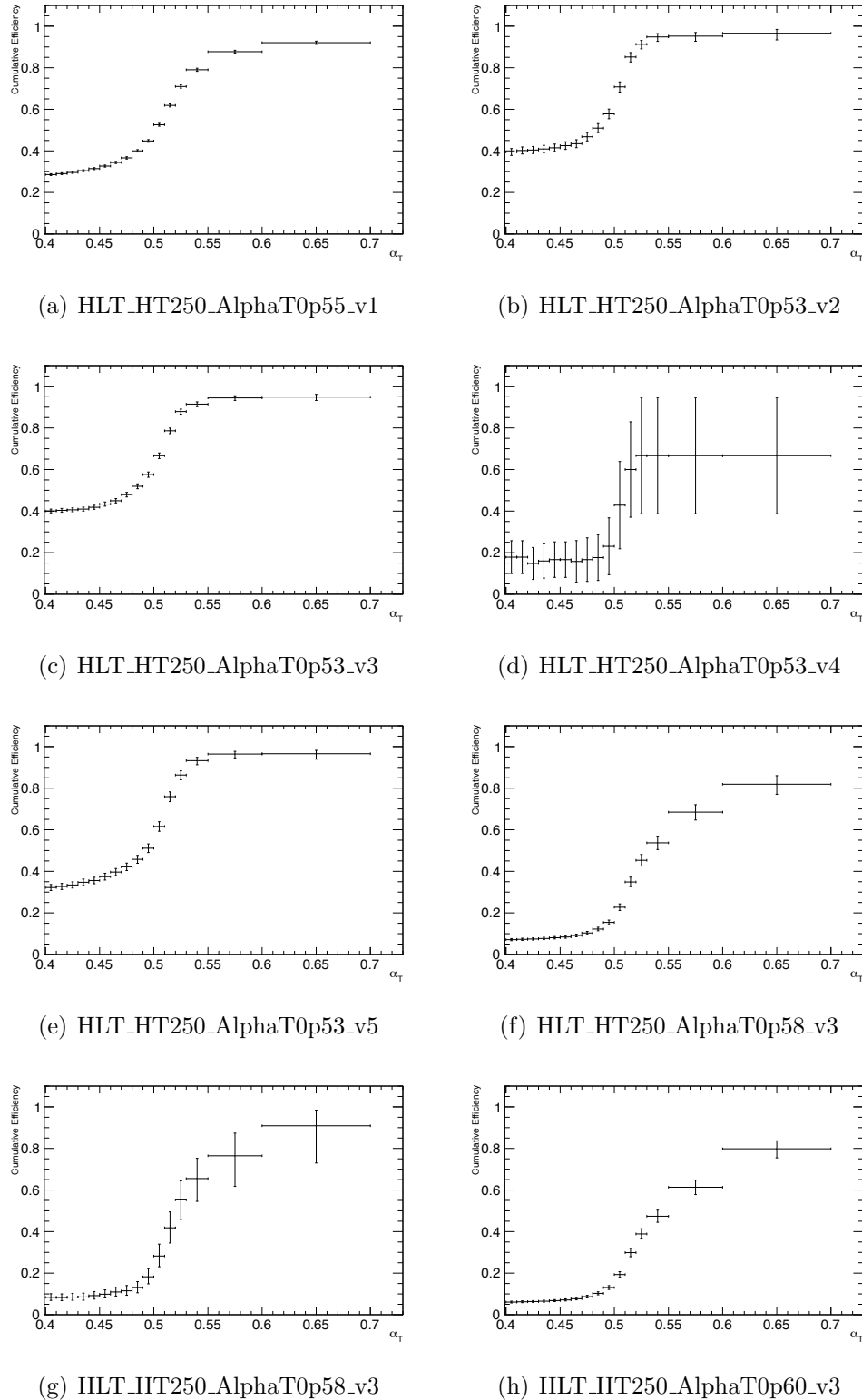
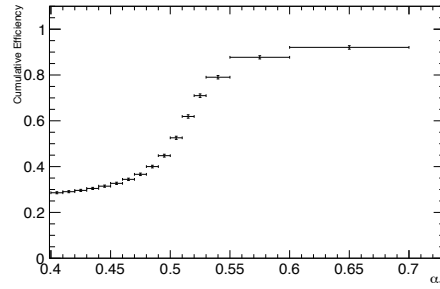


Figure 5.8.: Turn on curves for the individual α_T triggers used to seed the $275 \text{ GeV} < H_T < 325 \text{ GeV}$ bin.



(a) HLT-HT250_AlphaT0p60_v3

Figure 5.9.: Turn on curves for the individual α_T triggers used to seed the $275 \text{ GeV} < H_T < 325 \text{ GeV}$ bin.

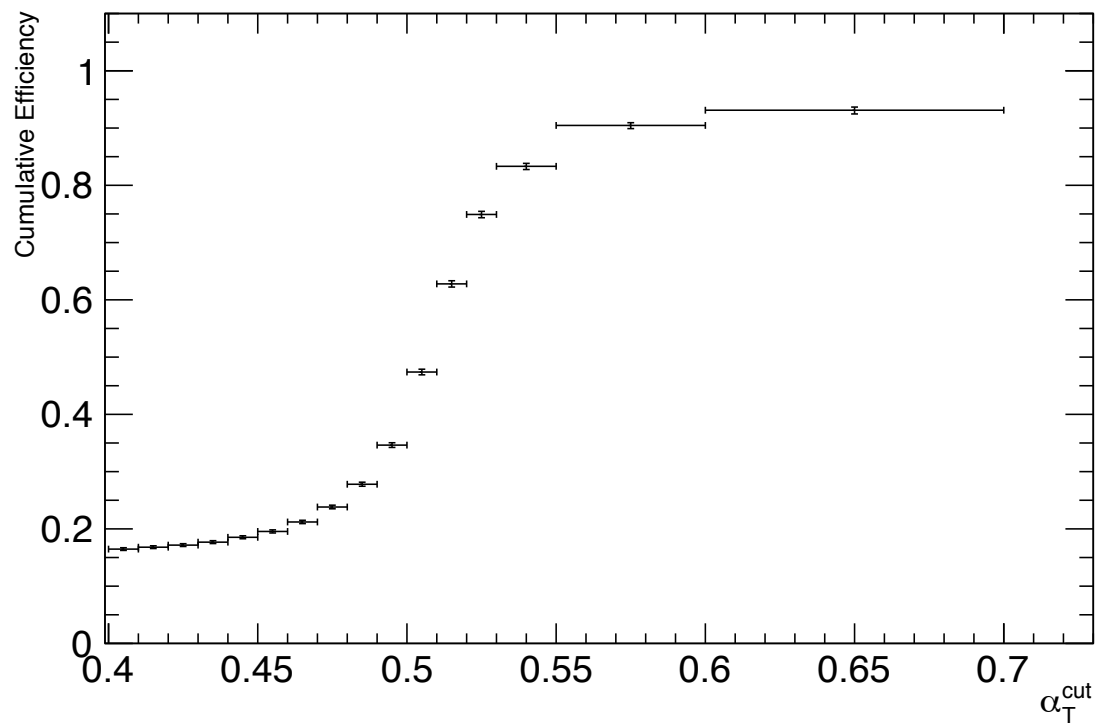


Figure 5.10.: Combined cumulative efficiency for the triggers seeding the $275 \text{ GeV} < H_T < 325 \text{ GeV}$ offline analysis bin.

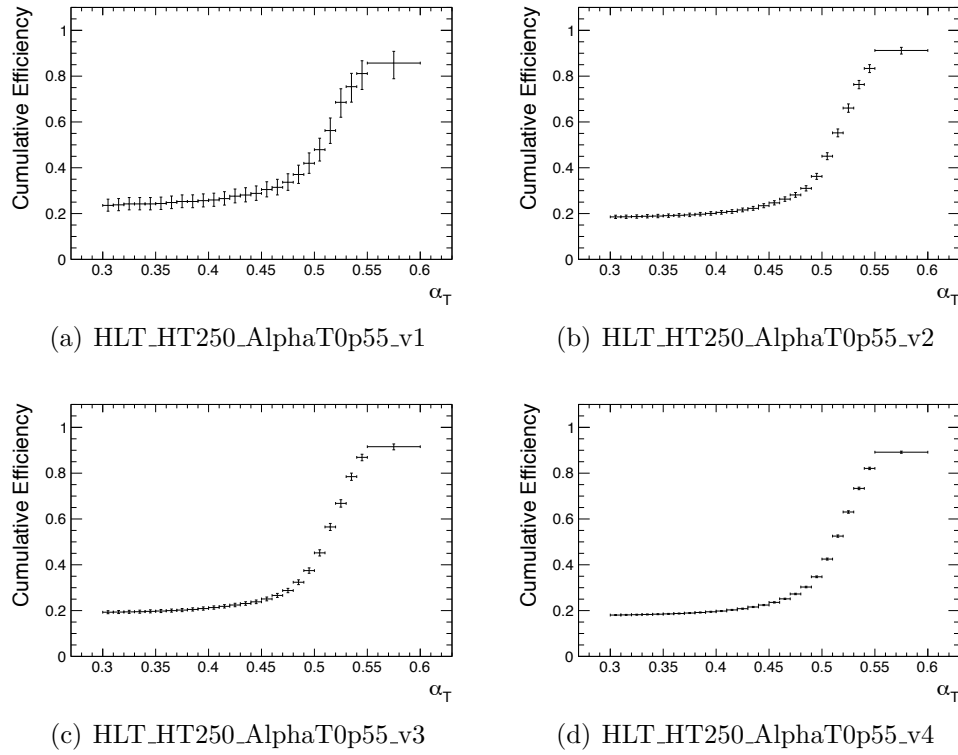


Figure 5.11.: Turn on curves for the individual α_T triggers used to seed the $275 \text{ GeV} < H_T < 325 \text{ GeV}$ bin, during 2012 data taking.

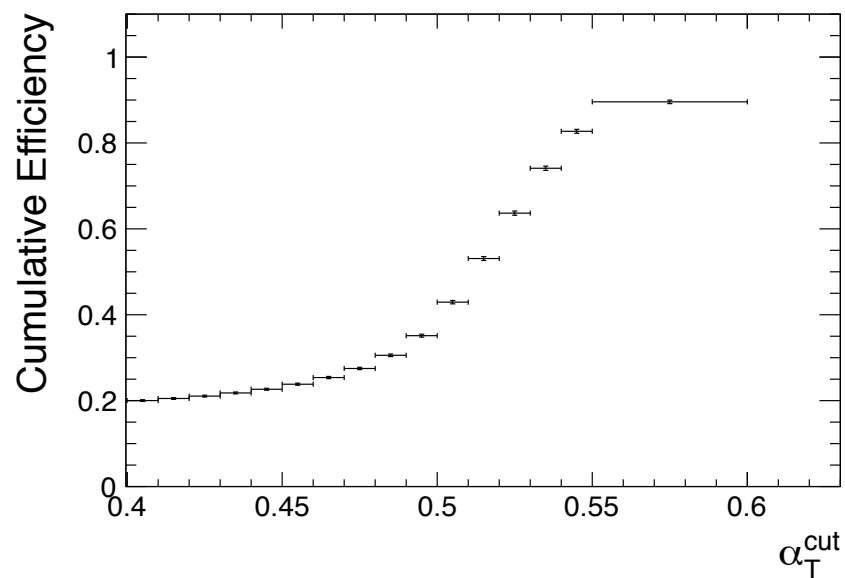


Figure 5.12.: Combined cumulative efficiency for the triggers seeding the $275 \text{ GeV} < H_T < 325 \text{ GeV}$ offline bin for 11.7 fb^{-1} of 8 TeV LHC data.

Chapter 6.

Background Prediction

The raw number of events in the signal region, where $\alpha_T > 0.55$ and $H_T > 275$ GeV, is meaningless without an accurate background prediction. Due to the hadronic nature of the backgrounds, selected in turn by the choice of a purely hadronic signal region and the prevalence of multi jet topologies in the final states, the detector simulation of the stochastic missmeasurement of jet energies is not advanced enough, not due to lack of understanding of the system, however due to the non-Gaussian nature of these effects the simulation is inherently incorrect. Hence the simulation is used to form a translation factor between two samples measured in data, a control sample which closely mimics the SM processes producing real missing energy, but has a visible muon or photon in the final state. The background estimation methods are described and the background predictions stated in this chapter. The backgrounds fall into the three categories:

By far the largest of these backgrounds arises from QCD multi-jet events where fake missing energy is introduced either from failures in reconstruction, or stochastic fluctuations in the calorimeter systems. However due to the theoretical errors on the QCD production cross section predicting the number QCD background events from Monte Carlo simulation is not possible. A secondary QCD background also exists, where due to the requirement of a jet E_T threshold, multiple jets fall under threshold by a few GeV, this causes a balanced event to look unbalanced as the jets under threshold are no longer considered. It is these sources of QCD background that α_T is designed to remove, for a detailed explanation of the α_T variable see Section 5.2.

The second major background comes from SM Electroweak decays and is irreducible, as the final states involve real missing energy from neutrinos. The Electroweak decays that form the background are $W \rightarrow \tau\nu + \text{Jets}$, where the τ is reconstructed as a jet, or the lepton fails the identification required for the dedicated lepton vetoes. $Z \rightarrow \nu\bar{\nu}$

+ Jets is completely irreducible. These are generally di-jet topologies. At higher jet multiplicities top quark production, followed by semi-leptonic top decay accounts for the largest background. These backgrounds are predicted using a well understood control sample this is fully explained in Section 6.1.

The final background source is that introduced by detector failure or electronic noise. Approximately 1% of the ECAL read out is not available in offline event reconstruction, this provides a source of fake missing energy. These generally add to the QCD background but are separated due to the cause being systematic due to hardware rather than intrinsic factors of the physical processes involved or the selection criteria applied.

6.1. Electroweak Background Prediction

The requirement of an α_T cut on the signal sample removes multi-jet QCD events where a balanced event is counted as signal due to missmeasurements. The remaining background events in the signal region are due to Electroweak processes which produce real missing energy. Primarily these events are produced from $Z \rightarrow \nu\bar{\nu} + \text{Jets}$, $W \rightarrow \ell\bar{\nu} + \text{Jets}$ and $t\bar{t}$ decay, with smaller contributions from Drell-Yan + Jets, single top production in the s, t channels and from di-boson + Jet events. To predict the number of these events contributing to the number of signal like events three control samples are defined and though the use of a Monte Carlo derived transfer factor the control samples are used to predict the number of SM events expected in the signal region.

Figure 6.1[72] shows the expectation from simulation in all bins of the hadronic signal region, for the different background samples and an example CMSSM reference model RM1 where $m_0 = 320 \text{ GeV}$, $m_{1/2} = 520 \text{ GeV}$, $A_0 = 0$ and $\tan\beta = 10$. The expected composition of the backgrounds in the signal region, as a percentage of the total SM background, are summarised in Table 6.1. $Z \rightarrow \nu\nu$ contributes $\approx 43\%$ of the SM background in the 275 GeV–325 GeV H_T bin, rising to $\approx 53\%$ in the $H_T > 875 \text{ GeV}$ bin. Events entering the signal region due to Z or W decays where the lepton is missed by the lepton vetoes account for $\approx 25\%$ at low H_T and $\approx 13\%$ at high H_T . Events from hadronic τ (τ_h) decays have little H_T dependance, contributing $\approx 22\%$ of the background at low H_T and $\approx 27\%$ of the background at high H_T . Those events arising from τ particles which decay leptonically (τ_l) and are missed by the lepton vetoes account for $\approx 10\%$ of the SM background.

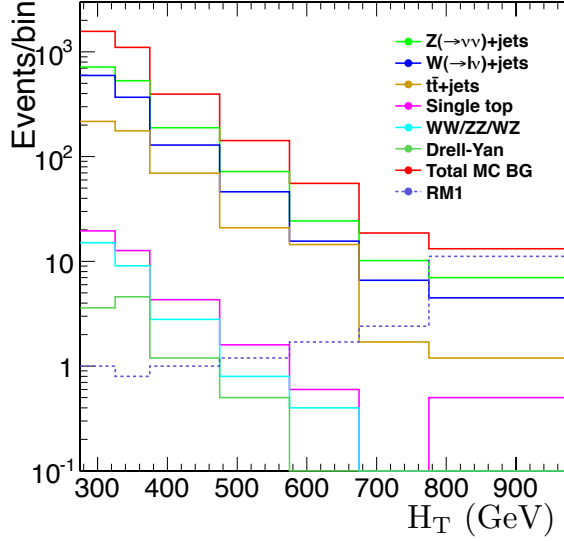


Figure 6.1.: Expectation from MC in all bins of the hadronic signal region for the following different background processes: $Z \rightarrow \nu\nu + \text{jets}$, $W + \text{jets}$, $t\bar{t}$, single top + jets, di-boson production ($WW/WZ/ZZ$), and Drell-Yan. The total SM expectation is also shown, along with that for the CMSSM benchmark model RM1.

Table 6.1.: Relative background composition as given by MC simulation in all bins of the hadronic signal region (expressed as a percentage of the total SM background).

H_T GeV	N _{events}	$Z \rightarrow \nu\nu + \text{jets}$ (%)	W + jets, $t\bar{t}$, single top, DY and di-boson			
			missed e, μ from W/Z (%)	τ_h (%)	τ_l (%)	τ_h matched to jet (%)
275–325	3938.0	43	24	22	11	7
325–375	1569.9	46	25	22	9	7
375–475	1104.2	48	20	23	10	7
475–575	396.0	48	17	24	11	10
575–675	142.4	51	17	23	10	11
675–775	55.5	44	19	31	7	17
775–875	18.7	55	17	22	4	9
875–7000	13.2	53	13	27	7	19

To calculate the bin-by-bin translation factors the signal selection and the individual control selections are applied to the Monte Carlo simulated background samples. The ratio of the number of accepted events is then taken, the signal yield prediction is computed from applying the the control selections to real data and multiplying the

event yield by the translation factor. The measurements form the control samples are considered simultaneously in a fit defined in Section 6.5. This method can be extended to include the exclusive b-tagged bins. For example in [69] a secondary dimension involving the number of b quarks in the event is studied. However the b extension is not detailed in this thesis.

Equation (6.1) describes the background prediction method, the number of predicted signal events per H_T bin is given as the number of events observed in the data control selection per H_T bin multiplied by the ratio of the number of events observed in the simulation when the hadronic selection is applied to the number of events observed in simulation when the control selection is applied, again per H_T bin.

$$N_{\text{prediction}}^{\text{sig}}(H_T) = N_{\text{obs}}^{\text{control}}(H_T) \times \frac{N_{\text{MC}}^{\text{sig}}(H_T)}{N_{\text{MC}}^{\text{control}}(H_T)} \quad (6.1)$$

The three control samples used are a $W \rightarrow \mu\nu + \text{Jets}$ sample, a $Z \rightarrow \mu\mu + \text{Jets}$ sample and a $\gamma + \text{Jets}$ sample.

The selection criteria for each of these control samples is kept as similar to the signal selection as possible, so as to not introduce systematic errors from incorrect modelling in the simulation. The use of the ratio of the number of observed events in the Monte Carlo cancels the systematic effects. A systematic is still assigned to each translation factor to account for theoretical uncertainties and acceptance and instrumental effects.

Additional kinematic cuts are applied in the two muon control samples to enrich the $W + \text{Jets}$ $t\bar{t}$ and $Z + \text{Jets}$ components in the control samples. The samples are defined to maximise efficiency rather than purity. Any impurities are accounted for in the transfer factors as the yields from all Monte Carlo samples are used. This is valid under the assumption that the SM Electroweak and Drell-Yan processes are well modelled by the simulation. The possibility of SUSY-like signal contamination in the control samples is accounted for in the final likelihood, after measuring the signal acceptance for the control samples on simulated SUSY events.

The magnitude of the systematic uncertainties on the transfer factors is motivated by a set of closure tests between the control samples. A transfer factor is produced to predict each control sample from each of the other control samples. No assumed systematic is

applied in these closure tests, instead the level of agreement after accounting for the statistical uncertainty is used to set the scale of the systematic error for each H_T bin.

6.1.1. The $\mu + \text{Jets}$ control sample

The $\mu + \text{Jets}$ control sample is designed to mimic the events appearing in the signal region due to $W + \text{Jets}$ and $t\bar{t}$ decays where the leptons are missed offline, either due to falling out of acceptance or being missed by the reconstruction algorithms. Hadronic tau decays from high p_T W bosons are also predicted from this sample. The additional selection criteria for this sample are designed to select events containing the decay $W \rightarrow \mu\nu + \text{Jets}$ in the same kinematic conditions as those events entering the signal selection. Offline the event level discriminators, H_T and α_T , are calculated using only the hadronic components of the event. In order to select the W , exactly one tightly identified, isolated muon within $|\eta| < 2.5$ with $p_T > 10 \text{ GeV}$ is required. The transverse mass of the muon combined with the missing energy of the event $M_T(\mu, \cancel{E}_T)$ is required to be larger than 30 GeV . As shown in Figure 6.2 the transverse mass cut removes a large amount of QCD whilst preserving a high efficiency W selection. Events are vetoed if for any jet $\Delta R(\mu, \text{jet}) < 0.5$, or if a second muon candidate exists that is either loose, non-isolated or outside of acceptance if the two muons have an invariant mass within $\pm 25 \text{ GeV}$ of the Z mass, to suppress $Z \rightarrow \mu\mu$ events.

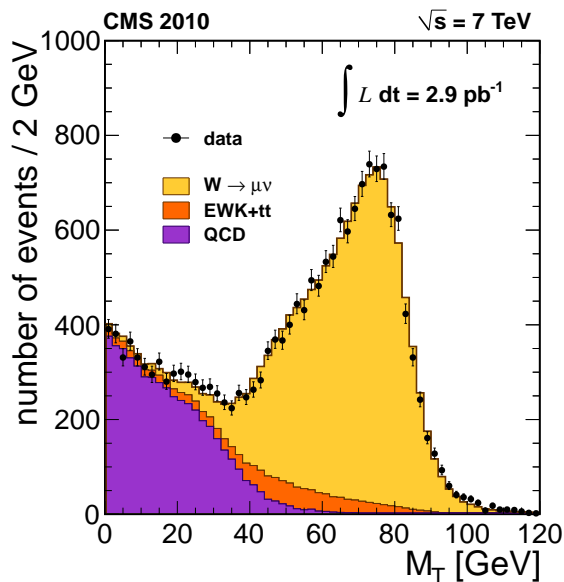


Figure 6.2.: Transverse mass between the selected muon and \cancel{E}_T in $W \rightarrow \mu\nu$ events.[73].

6.1.2. The $\mu\mu + \text{Jets}$ control sample

The $\mu\mu + \text{Jets}$ control sample is used to measure the $Z \rightarrow \nu\nu + \text{Jets}$ irreducible background in the signal region. The process $Z \rightarrow \mu\mu + \text{Jets}$ is identical kinematically, however the acceptance and the branching ratio are both smaller. The branching ratio due to the possible decay into one of three neutrino flavour states versus the requirement of a particular lepton flavour. The acceptance difference is due to the p_T and identification quality requirements on the muons which alter the acceptance between the two processes. The following selection criteria are applied on top of the common selection: Exactly two tightly identified, isolated muons, within $|\eta| < 2.5$ with $p_T > 10 \text{ GeV}$ are required; The invariant mass of the di-muon pair is required to be within $\pm 25 \text{ GeV}$ of the Z mass; Events are vetoed if for any muon and jet combination $\Delta R(\mu, \text{jet}) < 0.5$. As in the single muon control sample all event level quantities are calculated from the hadronic objects alone. This control sample can be used in all of the offline H_T bins.

6.1.3. The $\gamma + \text{Jets}$ control sample

The $\gamma + \text{Jets}$ control sample can also be used to measure the $Z \rightarrow \nu\nu + \text{Jets}$ background as the $\gamma + \text{Jets}$ process is kinematically similar when the photon $E_T > \approx 100 \text{ GeV}$ [74, 75], again when calculating the event level quantities only hadronic objects are considered. The photon sample requires the following criteria on top of the common selection requirements: exactly one photon with $E_T > 150 \text{ GeV}$ to ensure trigger efficiency, $|\eta| < 1.45$. Events are vetoed if for any jet $\Delta R(\gamma, \text{jet}) < 1.0$. Given that due to the trigger requirements the photon E_T is required to be greater than 150 GeV and the photon is treated as missing energy, the $\alpha_T > 0.55$ requirement implies a minimum H_T threshold of $\approx 350 \text{ GeV}$, hence the $\gamma + \text{Jets}$ control sample can only be used in the offline region where $H_T > 375 \text{ GeV}$.

Table 6.2 gives the hadronic signal yields in each of the offline H_T bins along with the simple background estimate from the single muon plus jets control sample. The full background prediction is given from the results of the simultaneous fit to the separate background estimates.

Table 6.2.: Total SM prediction using the $\mu + \text{Jets}$ sample only. These are illustrative only, as the final prediction is provided by the final simultaneous fit.

α_T bin	0.55– ∞	0.55– ∞	0.55– ∞	0.55– ∞
H_T bin (GeV)	275–325	325–375	375–475	475–575
Hadronic selection MC	2872.32 ± 64.44	1384.22 ± 51.46	1041.38 ± 12.53	396.13 ± 19.85
$\mu + \text{jets}$ selection MC	1228.90 ± 46.18	670.50 ± 38.74	495.14 ± 7.86	181.65 ± 9.65
Translation factor	2.34 ± 0.10	2.06 ± 0.14	2.10 ± 0.04	2.18 ± 0.16
$\mu + \text{jets}$ selection yield data	1421	645	517	169
Total SM prediction	3321.30 ± 169.97	1331.57 ± 105.45	1087.36 ± 52.50	368.56 ± 39.09
Hadronic yield data	3703	1533	1043	346
α_T bin	0.55– ∞	0.55– ∞	0.55– ∞	0.55– ∞
H_T bin (GeV)	575–675	675–775	775–875	875–7000
Hadronic selection MC	142.37 ± 7.61	55.47 ± 3.51	18.68 ± 1.45	13.18 ± 1.15
$\mu + \text{jets}$ selection MC	70.84 ± 4.36	22.64 ± 1.82	7.54 ± 0.80	5.19 ± 0.67
Translation factor	2.01 ± 0.16	2.45 ± 0.25	2.4 ± 0.33	2.54 ± 0.40
$\mu + \text{jets}$ selection yield data	52	18	8	1
Total SM prediction	104.50 ± 16.81	44.09 ± 11.33	19.83 ± 7.41	2.54 ± 3.47
Hadronic yield data	122	44	14	6

6.1.4. Muon control samples without an α_T cut

The requirement of an α_T value above 0.55 in the previous control samples limits the event yield of each of the Monte Carlo samples, increasing the statistical error of the prediction. This is especially evident when splitting the analysis into more dimensions than the H_T binning. The requirement of an α_T cut on the control samples means that as the muon is not seen by the calorimeter systems the signal trigger can also be used to collect the both the single and di muon background samples. The translation factor method can be used to create a prediction from any sample to any other sample if and only if the modelling of the event kinematics and acceptances of any cuts introduces no large systematic errors. We now show that the Monte Carlo simulation accurately reproduces the kinematics and acceptance of the α_T cut when applied to Electroweak background samples, enabling the removal of the α_T requirement for the muon control samples.

The preselection of events in the two muon control samples ensures samples with negligible QCD contamination, which are enriched with $t\bar{t}$, $W + \text{Jets}$ and $Z + \text{Jet}$ events. This is shown for the $\mu + \text{Jets}$ sample in Figure 6.3 and for the $\mu\mu + \text{Jets}$ sample in

Figure 6.4. In both sets of plots the expected number of QCD events from Monte Carlo simulation is less than one event at any α_T value for 5 fb^{-1} of integrated luminosity. The requirement of tight isolation on each of the muons is largely responsible for the purity of the sample, the transverse mass and di-muon mass window cuts ensure the sample is rich in Electroweak events. The agreement between data and Monte Carlo in these plots is good and the simulation models the α_T acceptance well. The systematic assigned to this acceptance is detailed in Section 6.2.

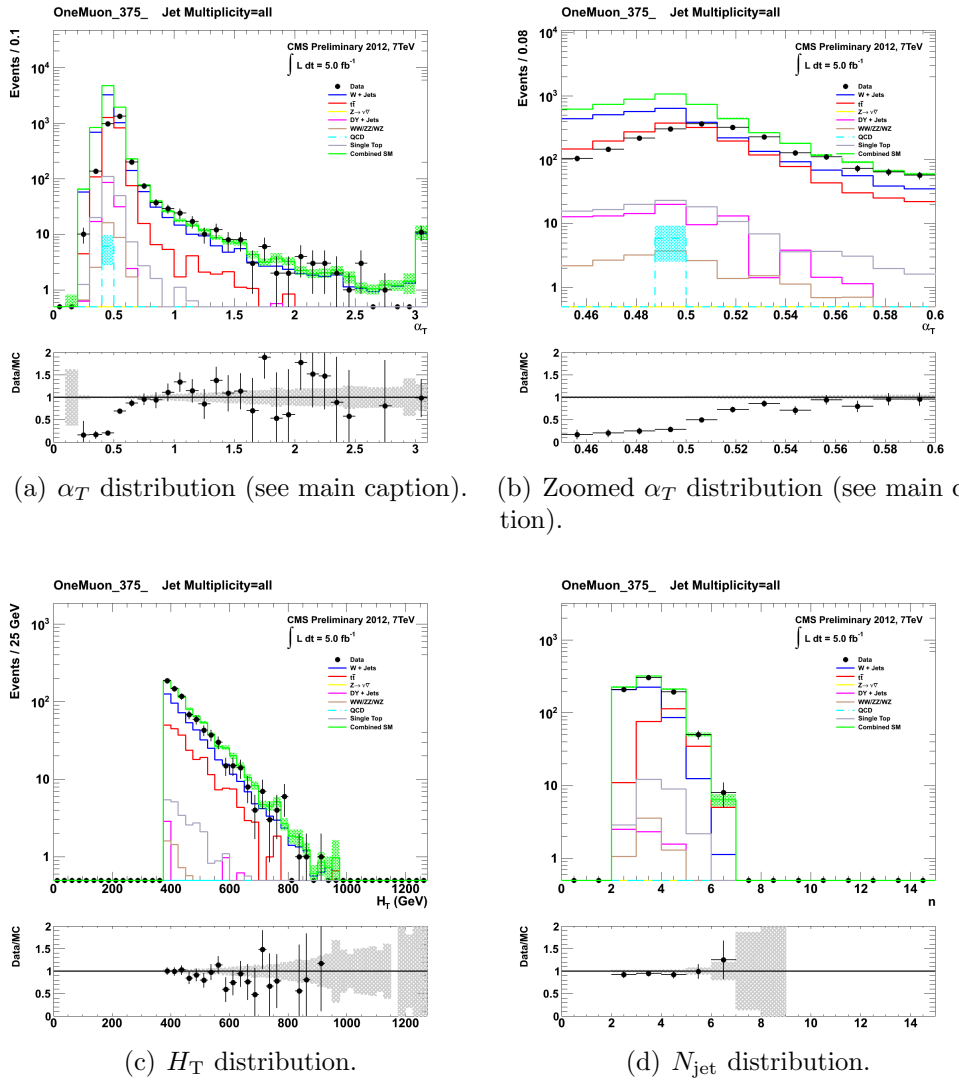


Figure 6.3.: Data–MC comparisons of key variables for the muon control sample, for the region $H_T > 375 \text{ GeV}$ and $\alpha_T > 0.55$. Bands represent the uncertainties due to the limited size of the MC samples. *The discrepancy in the α_T distributions for values $\alpha_T < 0.55$ is due to the trigger not being simulated in the MC simulation.*

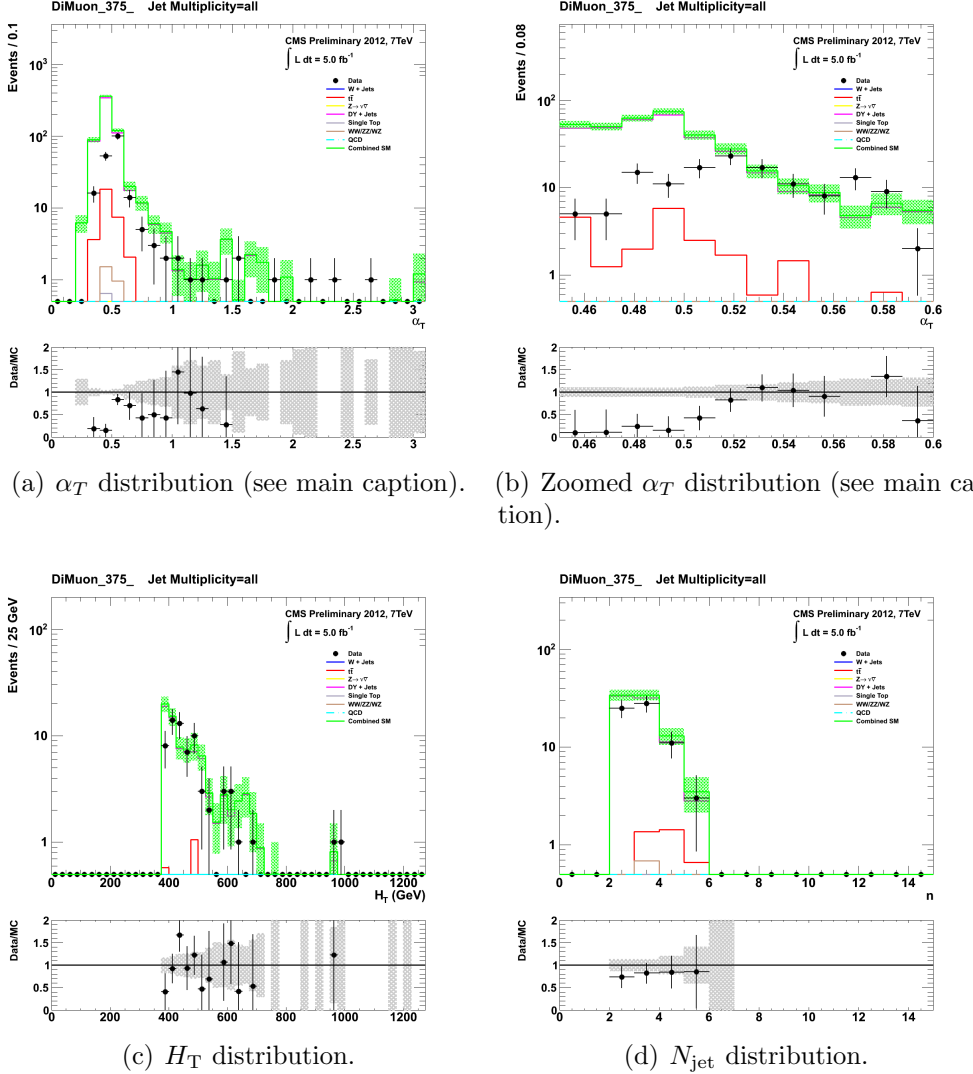


Figure 6.4.: Data–MC comparisons of key variables for the di-muon control sample, for the region $H_T > 375 \text{ GeV}$ and $\alpha_T > 0.55$. Bands represent the uncertainties due to the limited size of MC samples. *The discrepancy in the α_T distributions for values $\alpha_T < 0.55$ is due to the trigger not being simulated in the MC simulation.*

Moving to a selection where there is no required α_T cut means that the α_T trigger suite cannot be used to collect the high event yield control samples. Instead a trigger requiring H_T and a muon in the final state (`Mu_HT`) is used, due to the muon trigger threshold the p_T acceptance cut is raised to 45 GeV in these control samples. The H_T requirement on these triggers raises to 300 GeV so only the offline bins with $H_T > 375 \text{ GeV}$ are able to benefit from the increased background estimation precision, due to the larger size of the predicting sample. The efficiency for triggering on a single muon at 45 GeV is measured to be $91.3 \pm 0.1\%$ throughout the data taking period. For the

$H_T +$ single muon triggers, the H_T component of the trigger is measured to be 100% efficient throughout. In the case of the di-muon sample, as both muons have to be above 45 GeV and either of them could have triggered the event, the efficiency is found to be H_T -dependent in the range of 95-97%.

The muon control samples in the H_T bins where $H_T < 375$ GeV are collected with the α_T trigger suite and the measured efficiencies are the same as those measured for the hadronic sample. The details of the triggers used for each of the muon + Jets control samples are listed in Table 6.3.

Table 6.3.: List of triggers used for the larger $\mu +$ Jets and $\mu\mu +$ Jets samples.

H_T bin (GeV)	275–325	325–375	375–475	475–575	575–675	675–775	775–875	>875
α_T cut	0.55	0.55	None	None	None	None	None	None
Muon p_T cut	10	10	45	45	45	45	45	45
Trigger	α_T	α_T	Mu_HT	Mu_HT	Mu_HT	Mu_HT	Mu_HT	Mu_HT
Thresholds	Table B.5	Table B.5	Table B.6					

6.2. Systematic uncertainties on the Electroweak background model

As previously discussed in Section 6.1 the final background prediction is given by the simultaneous fit to the yields in the signal and control samples and the translation factors obtained from MC. The fit has some freedom via the statistical and systematic uncertainties measured for each translation factor. The measurement of the systematic uncertainties on the translation factors are thus vital for the fitting procedure.

A set of closure tests were performed on data to identify any sources of systematic biases introduced by the background prediction method. To do this the individual background samples are used to predict one another using the same translation factor method as for the prediction of the SM missing energy sources in the hadronic signal regions. The level of agreement is quantified in terms of the ratio $(N_{obs} - N_{pred}) / N_{pred}$, the statistical error from the translation factor, based on the available Monte Carlo sample size is combined with the statistical error on the number of events in the predicting sample to give the error on the closure. A deviation in the ratio from zero gives the

level of closure per analysis bin. This gives a measure of any biases introduced by the background estimation method.

The closure tests between the background samples are designed to test the Monte Carlo's ability to model kinematic effects: such as the α_T acceptance; μ acceptance and γ acceptance, instrumental effects such as, reconstruction efficiencies and the effects of pile-up on isolation and finally the theoretical precision of the production and decay cross sections and their relative contributions to the SM background. These individual components are not separable by the closure tests, which instead gives a total systematic error estimation.

As described in Section 6.1.4 the control samples which do not require an α_T cut use a Mu-HT cross object trigger to collect the data events. As shown in Table B.6 there was a period of data taking where due to the increased trigger thresholds the Mu-HT triggers are unsuitable for use in the region $H_T < 375$ GeV. Thus in the closure tests between the control samples which use an α_T cut and those that do not, the integrated luminosity is limited to 3.9 fb^{-1} . This causes a loss of some statistical power in these cases.

The individual closure tests and fits to the H_T dependance of the ratio $(N_{obs} - N_{pred}) / N_{pred}$ are shown in Appendix D. Figures D.1 show the closure of the prediction between $\mu + \text{Jets}(\text{no } \alpha_T) \rightarrow \mu + \text{Jets}(\alpha_T > 0.55)$ and $\mu\mu + \text{Jets}(\text{no } \alpha_T) \rightarrow \mu\mu + \text{Jets}(\alpha_T > 0.55)$ for two samples, one with no requirement on the number of b-tagged jets (n_b), which increases the precision of the measurement, and one requiring $n_b = 1$, the red line is the result of a one parameter fit. The level of closure shows that the Monte Carlo accurately models the α_T acceptance, with no significant bias.

Figure D.2 shows the closure between $\mu + \text{Jets} \rightarrow \mu\mu + \text{Jets}$ and between $\gamma + \text{jets} \rightarrow \mu\mu + \text{Jets}$ over the full H_T range using only 3.9 fb^{-1} of integrated luminosity and for $H_T > 375$ GeV using the full data set. Again the red lines are the result of fitting with a one parameter fit. The muon to di-muon closure tests the value for σ_Z/σ_W and any acceptance effects due to the inclusion of real missing energy in the same. The di-muon to photon closure quantifies the level of certainty of the ratio of the photon + Jets production cross section to the Z + Jets production cross section as well as the acceptance difference between the muon and photon requirements.

Figure D.3 tests the closure between samples with differing n_b the three tests are $\mu + \text{Jets}(n_b = 0) \rightarrow \mu + \text{Jets}(n_b = 1, \text{no } \alpha_T)$, $\mu + \text{Jets}(n_b = 1) \rightarrow \mu + \text{Jets}(n_b > 1, \text{no } \alpha_T)$ and $\mu + \text{Jets}(n_b = 0) \rightarrow \mu + \text{Jets}(n_b > 1, \text{no } \alpha_T)$. Figure D.4 also tests the closure between samples with differing n_b , here the test is between $\mu + \text{Jets}(n_b = 0) \rightarrow \mu\mu + \text{Jets}(n_b = 0)$

and $\mu + \text{Jets}(n_b = 1) \rightarrow \mu\mu + \text{Jets}(n_b = 1)$. These tests show that the re-weighting method applied to the b tagging efficiency and fake rates is correct and that by using these values it is possible to translate between different b tag multiplicities.

Finally any dependence on pile-up is measured by comparing a subset of the individual closure tests between samples which have pile-up subtracted jets and those that do not. The example closures are $\mu + \text{Jets}(\text{no } \alpha_T) \rightarrow \mu + \text{Jets}(\alpha_T > 0.55)$, $\mu + \text{Jets}(\text{no } \alpha_T) \rightarrow \mu\mu + \text{Jets}(\text{no } \alpha_T)$, and $\mu + \text{Jets}(n_b = 0) \rightarrow \mu + \text{Jets}(n_b = 1, \text{no } \alpha_T)$.

6.3. Systematic errors and biases on the translation factors

The closure tests described in the previous section are combined to give a total systematic uncertainty. This uncertainty is binned into three H_T regions 275 GeV \rightarrow 575 GeV, 575 GeV \rightarrow 775 GeV and $>$ 775 GeV. In each of these regions all of the individual closure tests are used to calculate a weighted mean and variance. The systematic is defined as 3σ of this variance, which is conservative but necessary to cover any biases. The systematics are treated as fully uncorrelated between the three regions, again this is the conservative approach. Figure 6.5 shows the key example closures, the grey shaded region shows the systematic error. The values obtained for the error are 6%, 20% and 39%, these are rounded to 10%, 20% and 40% and then used in the final background simultaneous fit.

6.4. Estimating the residual QCD background component.

The expected QCD contamination in the signal region where $H_T > 275$ GeV and $\alpha_T > 0.55$ from simulated background samples is negligible[72]. Residual events are removed via the application of the detector failure and $R_{miss} < 1.25$ filters. However due to the difficulty in simulating QCD multi-jet events accurately a conservative approach is taken where a term is inserted in the likelihood to model any residual QCD contamination.

The term is based on the ratio of the number of events above and below the α_T threshold of 0.55 in the individual H_T bins. The dependance of this ratio is modelled as

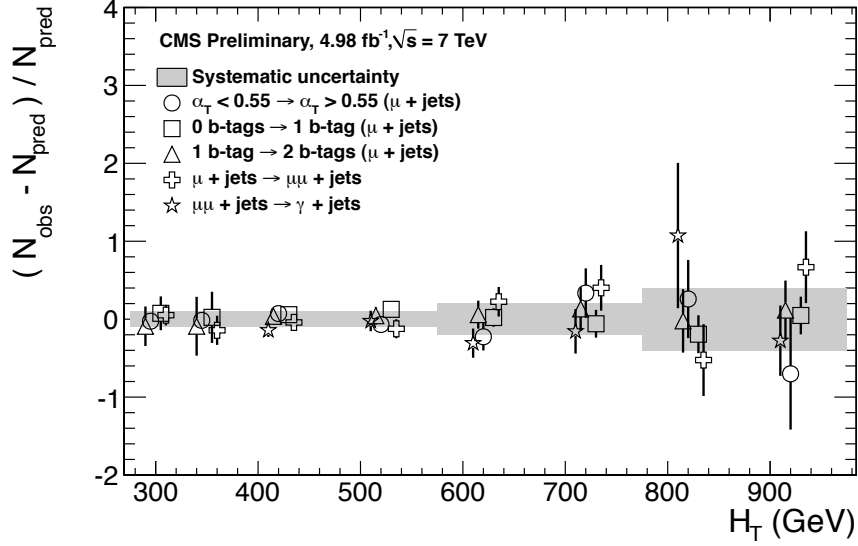


Figure 6.5.: A set of closure tests (open symbols) overlaid on top of grey bands that represent the systematic uncertainties used for three H_T regions in the final simultaneous fit. The solid circles and their errors represent the weighted mean and standard deviation for the five closure tests of each individual H_T bin.

an exponentially falling quantity:

$$R_{\alpha_T}(H_T) = \mathcal{A}_{n_b} e^{-k_{QCD} H_T}. \quad (6.2)$$

Where \mathcal{A}_{n_b} is the b-tag bin dependent normalisation factor and k_{QCD} is the b-tag dependent decay constant.

The exponential behaviour, which is shown in Figure C.1 is due to several features, the first of which is the improvement of the relative jet energy resolution with H_T due to the larger energies deposited in the calorimeter systems. Secondly for the region $H_T > 375$ GeV the jet multiplicity rises slowly with H_T , which due to the combinatorics used in the α_T calculation, results in a narrower α_T distribution peaked at 0.5. Due to the signal region definition and the exponentially falling nature of the QCD, the QCD background component is reduced to zero above ≈ 500 GeV, thus the validity of the QCD background model above 575 GeV is not of consequence to the final analysis, however the model chosen is shown to be valid over the whole H_T region of the analysis as shown below.

Maximum likelihood (ML) values for k_{QCD} and \mathcal{A}_{n_b} are found by the final likelihood fit, however k_{QCD} is first constrained by a measurement in the background enriched side band regions where either the α_T cut is relaxed or the R_{miss} cut is inverted. Figure 6.6

depicts the regions where k_{QCD} is measured, the signal region is as described before where $\alpha_T > 0.55$ and $R_{miss} < 1.25$ are required. Region B is defined by the inversion of the α_T cut. Region C is defined by inverting both the α_T requirement and the R_{miss} requirement, this region is further divided into three slices in α_T of $0.52 < \alpha_T < 0.53$, $0.53 < \alpha_T < 0.54$ and $0.54 < \alpha_T < 0.55$, as the index of C_i rises the expected amount of QCD in that control region increases. Finally region D has only the R_{miss} requirement inverted, region D is not used to constrain k_{QCD} , but instead to check the validity of the exponential model. The fits to the individual side bands are shown in Appendix C. The

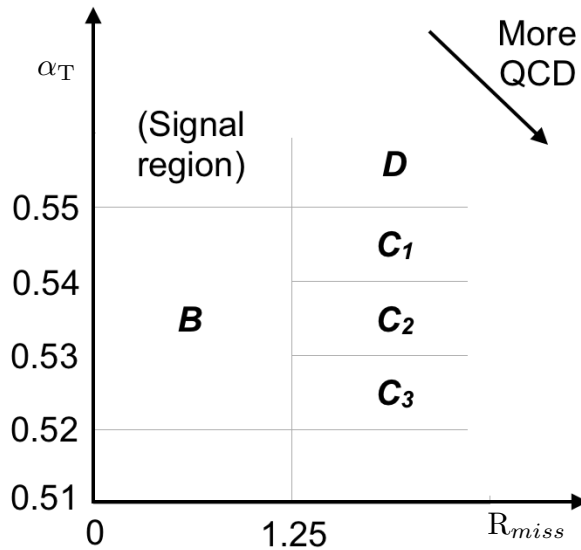


Figure 6.6.: QCD side-band regions, used for determination of k_{QCD} .

best fit value for k_{QCD} of $2.96 \pm 0.64 \times 10^{-2} \text{ GeV}^{-1}$ obtained from region B is used as the central value of the constraint. The assumption that this method gives an unbiased estimate of k_{QCD} stems from the similarity in event kinematics in the two α_T regions. The best fit values for the three C_i regions are used to estimate the systematic uncertainty on the central value obtained from region B . The fit results show no dependence on the α_T region used to measure the number of events, supporting the assumption that region B provides an unbiased estimate of k_{QCD} . The variation of the measured values for each C_i slice are used to calculate the error on the central value, the weighted mean and standard deviation of the three slices in α_T are calculated to be $1.31 \pm 0.26 \times 10^{-2} \text{ GeV}^{-1}$, the relative error on this value is 20% which is then applied to the central value to give an estimate of the systematic uncertainty.

The data side bands are used to provide a constrained value of k_{QCD} as an input to the final likelihood model which describes the expected number of background events in

bins of H_T and the number of observed jets containing a b quark. The value measured for k_{QCD} is $2.96 \pm 0.61(\text{stat}) \pm 0.46(\text{sys}) \times 10^{-2} \text{ GeV}^{-1}$. The uncertainty values are used as penalty terms in the likelihood model which is described in Section 6.5.

Table 6.4.: Best fit values for the parameters k as obtained from the regions B , C_1 , C_2 , and C_3 . The latter three measurements are used to calculate a weighted mean (identified as region C). Also quoted is the maximum likelihood value of the parameter k given by the simultaneous fit using the sample defined by region D . Quoted errors are statistical only. From [72].

Side-band region	$k_{QCD} (\times 10^{-2} \text{ GeV}^{-1})$	p -value
B	2.96 ± 0.64	0.24
C_1	1.19 ± 0.45	0.93
C_2	1.47 ± 0.37	0.42
C_3	1.17 ± 0.55	0.98
C (weighted mean)	1.31 ± 0.26	-
D (likelihood fit)	1.31 ± 0.09	0.57

A final check is performed using region D , which requires $\alpha_T > 0.55$ but has no R_{miss} cut, this introduces QCD background into the signal region. The likelihood fit is performed on this background enriched region and no constraint is applied on k_{QCD} which is then determined by the fit only. The fit is performed over the full H_T range used in the final analysis. Figure 6.7 shows the resulting fit, the ML value obtained for k_{QCD} is $(1.31 \pm 0.09) \times 10^{-2} \text{ GeV}^{-1}$, this value is in excellent agreement with the value found from the weighed mean of the regions C_i . The fit shows that the choice of exponential function used in the likelihood model is valid over the entire H_T range. This supports the assumption that region B provides an unbiased estimate of k_{QCD} in the signal region $\alpha_T > 0.55$ and $R_{miss} < 1.25$.

6.5. Likelihood model

The likelihood model which is fully described in [76] is used to gauge the agreement between the observed yields in the hadronic signal region and the predicted yields obtained from the control samples. For the hadronic sample the likelihood is as follows, for N bins in H_T , let n_i represent the observed hadronic yield in H_T bin i , the likelihood for

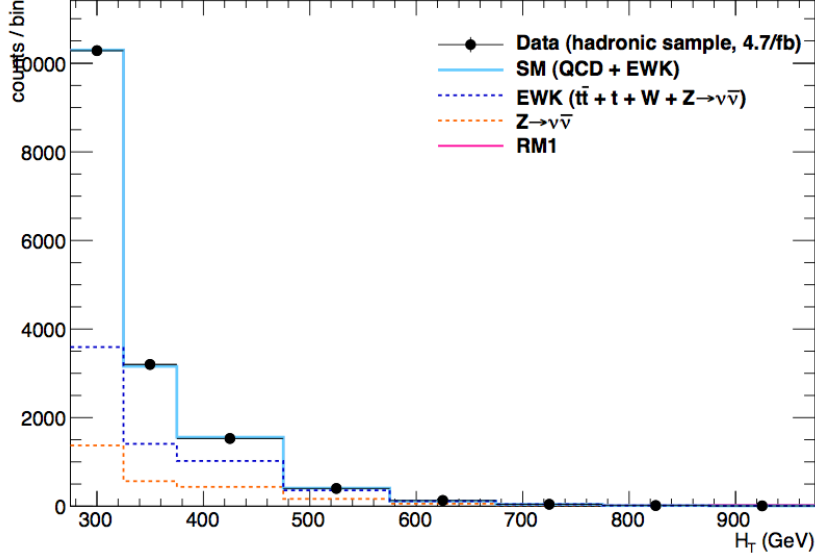


Figure 6.7.: Comparison of the observed yields and SM expectations given by the simultaneous fit in bins of H_T for the side-band region D . No requirement on the number of b jets is made. Shown are the observed event yields in data (black dots with error bars representing the statistical uncertainties) and the expectations given by the simultaneous fit for the $Z \rightarrow \nu\nu + \text{jets}$ process (orange dotted-dashed line); the sum of all processes with genuine \cancel{E}_T , which are primarily $t\bar{t}$, $W + \text{jets}$, and $Z \rightarrow \nu\nu + \text{jets}$ (dark blue long-dashed line); and the sum of QCD and all aforementioned SM processes (light blue solid line).[72]

observing n_i events is then

$$L_{had} = \prod_i \text{Pois}(n_i | b_i + s_i) \quad (6.3)$$

where b_i is the number of expected background events and s_i the expected signal yield, which is dependent on the signal model being considered. Pois refers to the Poisson distribution of these values and is defined in Equation (6.4), b_i is equal to the sum of Electroweak events expected plus the number of QCD events ($b_i = EWK_i + QCD_i$) expected per bin.

$$\text{Pois}(\mathcal{X}|\lambda) = \frac{\lambda^x e^{-\lambda}}{k!} \quad (6.4)$$

In Section 6.4 it was shown that the QCD contribution can be modelled as an exponentially falling as a function of H_T .

$$R_{\alpha_T}(H_T) = A_{QCD} e^{-k_{QCD} H_T} \quad (6.5)$$

Where A_{QCD} and k_{QCD} have been constrained by measurements in the control regions. QCD_i is then given as:

$$QCD_i = m_i A_{QCD} e^{-k_{QCD} \langle H_T \rangle^i}. \quad (6.6)$$

Where m_i is the number of events per H_T bin which fail $\alpha_T > 0.55$ and $\langle H_T \rangle^i$ is the mean H_T of the bin.

For the Electroweak background two components are considered, f_{Zinv}^i which represents the fraction of the total Electroweak background contributed by $Z \rightarrow \nu\nu + \text{Jets}$ events. This is modelled as a linear component:

$$f_{Zinv}^i = f_{Zinv}^0 + \frac{\langle H_T \rangle^i - \langle H_T \rangle^0}{\langle H_T \rangle^{N-1} - \langle H_T \rangle^0} (f_{Zinv}^{N-1} - f_{Zinv}^i), \quad (6.7)$$

where f_{Zinv}^i and f_{Zinv}^{N-1} are floating parameters whose final values are limited between zero and one. The total number of $Z \rightarrow \nu\nu + \text{Jets}$ events per bin is then given by:

$$Z_{inv}^i = f_{Zinv}^i \times \text{EWK}^i. \quad (6.8)$$

The remaining background from other Electroweak processes given by:

$$Y = (1 - f_{Zinv}^i) \times \text{EWK}^i. \quad (6.9)$$

In each H_T bin i there are three background measurements, n_γ^i , n_μ^i and $n_{\mu\mu}^i$, representing the event counts from the photon, muon and di-muon control samples respectively. Each of these yields has a Monte Carlo counter-part yield. From the Monte Carlo it is also possible to extract MC_{Zinv}^i and MC_Y^i . After defining:

$$r_\gamma^i = \frac{MC_\gamma^i}{MC_{Zinv}^i}, \quad r_{\mu\mu}^i = \frac{MC_{\mu\mu}^i}{MC_{Zinv}^i}, \quad r_\mu^i = \frac{MC_\mu^i}{MC_Y^i} \quad (6.10)$$

Table 6.5.: The systematic parameters used in H_T bins.

H_T bin (i)	0	1	2	3	4	5	6	7
syst. parameter (j)	0	0	0	0	1	1	2	2

three likelihood functions are defined:

$$L_\gamma = \prod_i Pois \left(n_\gamma^i | \rho_{\gamma Z}^j \cdot r_\gamma^i \cdot Z_{inv}^i \right), \quad (6.11)$$

$$L_{\mu\mu} = \prod_i Pois \left(n_{\mu\mu}^i | \rho_{\mu\mu Z}^j \cdot r_{\mu\mu}^i \cdot Z_{inv}^i \right), \quad (6.12)$$

$$L_\mu = \prod_i Pois \left(n_\mu^i | \rho_{\mu Y}^j \cdot r_\mu^i \cdot Y^i + s_\mu^i \right), \quad (6.13)$$

Equation (6.11) is used to estimate the ML values for Z_{inv} , which is the expectation of the number of $Z \rightarrow \nu\nu + \text{Jets}$ events in the hadronic signal region, using the observations n_γ^i in the photon control sample and the ratio r_γ^i . Similarly the number of $Z \rightarrow \nu\nu + \text{Jets}$ events expected in the signal region, predicted by the $Z \rightarrow \mu\mu + \text{Jets}$ are found using Equation (6.12). The non $Z \rightarrow \nu\nu$ backgrounds are estimated by the ML value for Equation (6.13), in a similar way with the addition of s_μ^i , which represents the signal contamination in the single muon control sample. The measurements and ratios are considered simultaneously though the relationships defined in Equations (6.3), (6.8) and (6.9). The ratios r_γ^i , $r_{\mu\mu}^i$ and r_μ^i are the inverse of the translation factors given by Equation (6.1). The parameters $\rho_{\gamma Z}$, $\rho_{\mu\mu Z}$ and $\rho_{\mu Y}$ are correction factors that account for the systematic uncertainty on each of the ratios and $\sigma_{\gamma Z}$, $\sigma_{\mu\mu Z}$ and $\sigma_{\mu Y}$. They represent the relative systematic uncertainties for the control sample constraints, these are accounted for in:

$$L_{EWK \ syst} = \prod_j Gaus \left(1.0 | \rho_{\mu Y}^j, \sigma_{\mu Y}^j \right) \times Gaus \left(1.0 | \rho_{\mu\mu Z}^j, \sigma_{\mu\mu Z}^j \right) \times Gaus \left(1.0 | \rho_{\gamma Z}^j, \sigma_{\gamma Z}^j \right) \quad (6.14)$$

Three parameters per control sample are used to cover the eight H_T bins as show in Table 6.5.

Alternatively the single muon control sample can be used to constrain the total Electroweak background, we can define:

$$r'_\mu = \frac{MC_\mu^i}{MC_{tot}^i} \quad (6.15)$$

and

$$L'_\mu = \prod_i Pois(n_\mu^i | \rho_{\mu Y} \times r'_\mu^i \times EWK^i + s_\mu^i) \quad (6.16)$$

6.5.1. Signal Contamination

The cross section for each model is represented by x and l represents the total recorded luminosity considered by the analysis in the signal region. The efficiency is defined as ϵ_{had}^i for the signal region and ϵ_μ^i for the single muon control sample, δ represents the relative uncertainty on the signal as measured in the previous section, δ is taken to be fully correlated though the H_T bins. ρ_{sig} is the correction factor to the signal yield which accommodates this uncertainty. f represents an unknown multiplicative factor on the signal cross section, for which an allowed interval is computed. The expected signal yield s^i from Equation (6.3) is defined as:

$$s_{had}^i = f \rho_{sig} x l \epsilon_{had}^i, \quad (6.17)$$

the signal contamination s_μ^i is given by:

$$s_\mu^i = f \rho_\mu x l \epsilon_\mu^i. \quad (6.18)$$

The systematic uncertainty on the signal is included by an additional term in the likelihood:

$$L_{sig} = Gaus(1.0 | \rho_{sig}, \delta). \quad (6.19)$$

6.5.2. The total likelihood

The total likelihood for a given signal selection $k(H_T, n_b)$ is given by:

$$L^k = L_{had}^k \times L_\mu^k \times L_\gamma^k \times L_{\mu\mu}^k, \quad (6.20)$$

each k has $3 + N$ nuisance parameters; $\mathcal{A}_{QCD}, f_{Zinv}^0, f_{Zinv}^{N-1}, \{\text{EWK}^i\}_{i=0}^{N-1}$. The 11 parameters k_{QCD}, ρ_{sig} , and $\rho_{\gamma Z}^k, \rho_{\mu\mu}^k, \rho_\mu^k$ with $j = \{0, 1, 2\}$ are shared between the selections, the total likelihood is then given as:

$$L = L_{sig} \times L_{\text{EWKsyst}} \times \prod_k L_{had}^k \times L_\mu^k \times L_\gamma^k \times L_{\mu\mu}^k. \quad (6.21)$$

6.6. Final Results

The yields obtained in the hadronic signal regions are tested for their compatibility with the background predicted by the likelihood model both in terms of agreement with the SM and interpretations in the forms of limits on new physics models.

To test the level of agreement with the SM the signal terms are dropped from the likelihood, which is then maximised over all parameters using RooFit[77] and MINUIT[78]. The individual yields and errors from the fits are shown in Appendix A. The total background and data yields and their errors as given by the ML fit are show below in Table 6.6.

Table 6.6.: Comparison of the measured yields in the different H_T and b-jet multiplicity bins for the hadronic sample with the SM expectations and combined statistical and systematic uncertainties given by the simultaneous fit.

H_T (GeV)	275–325	325–375	375–475	475–575	575–675	675–775	775–875	875– ∞
0 b jets SM	2933^{+56}_{-52}	1139^{+17}_{-40}	783^{+17}_{-27}	261^{+14}_{-8}	$81.5^{+6.5}_{-6.5}$	$34.2^{+4.0}_{-3.8}$	$10.4^{+2.8}_{-1.8}$	$5.3^{+1.7}_{-1.1}$
0 b jets Data	2919	1166	769	255	91	31	10	4
1 b jet SM	630^{+26}_{-25}	271^{+10}_{-16}	202^{+10}_{-6}	$78.0^{+6.9}_{-1.9}$	$24.2^{+2.9}_{-2.0}$	$10.6^{+1.7}_{-1.3}$	$2.9^{+0.9}_{-0.5}$	$2.2^{+0.7}_{-0.4}$
1 b jet Data	614	294	214	71	20	6	4	0
2 b jets SM	162^{+13}_{-12}	$61.8^{+4.8}_{-6.3}$	$58.8^{+4.8}_{-2.6}$	$28.0^{+3.5}_{-1.1}$	$9.0^{+1.4}_{-1.0}$	$7.1^{+1.4}_{-1.0}$	$0.6^{+0.3}_{-0.2}$	$0.9^{+0.4}_{-0.2}$
2 b jets Data	160	68	52	19	11	7	0	2
≥ 3 b jets SM	$10.5^{+3.5}_{-2.2}$	$7.1^{+2.2}_{-1.8}$	$5.8^{+1.4}_{-0.9}$	$3.1^{+1.0}_{-0.7}$	$1.7^{+0.5}_{-0.4}$	$0.7^{+0.5}_{-0.4}$	$0.1^{+0.1}_{-0.1}$	$0.2^{+0.1}_{-0.1}$
≥ 3 b jets Data	10	8	8	1	0	0	0	0

Figures 6.8, 6.9, 6.10 and 6.11 show comparisons of the observed yields and the SM only expectations given by the simultaneous fit for 0, 1, 2, ≥ 3 exclusive b-tag bins. A good agreement with the standard model is observed in all H_T and b-tag categories. Given the lack of a signal like observation, limits are set on the production masses and cross sections of beyond the SM particles. In the figures the two SUSY models refer to

points in the SMS plane. Model A has a heavy gluino and a relatively light neutralino, this gives a final state involving four or more jets and no preference to heavy quarks in the final state. Model D has a heavy stop and a light neutralino, given the smaller mass splitting the H_T bin that the signal falls in to is lower and due to the sbottom in the production method there are necessarily b-jets in the final state.

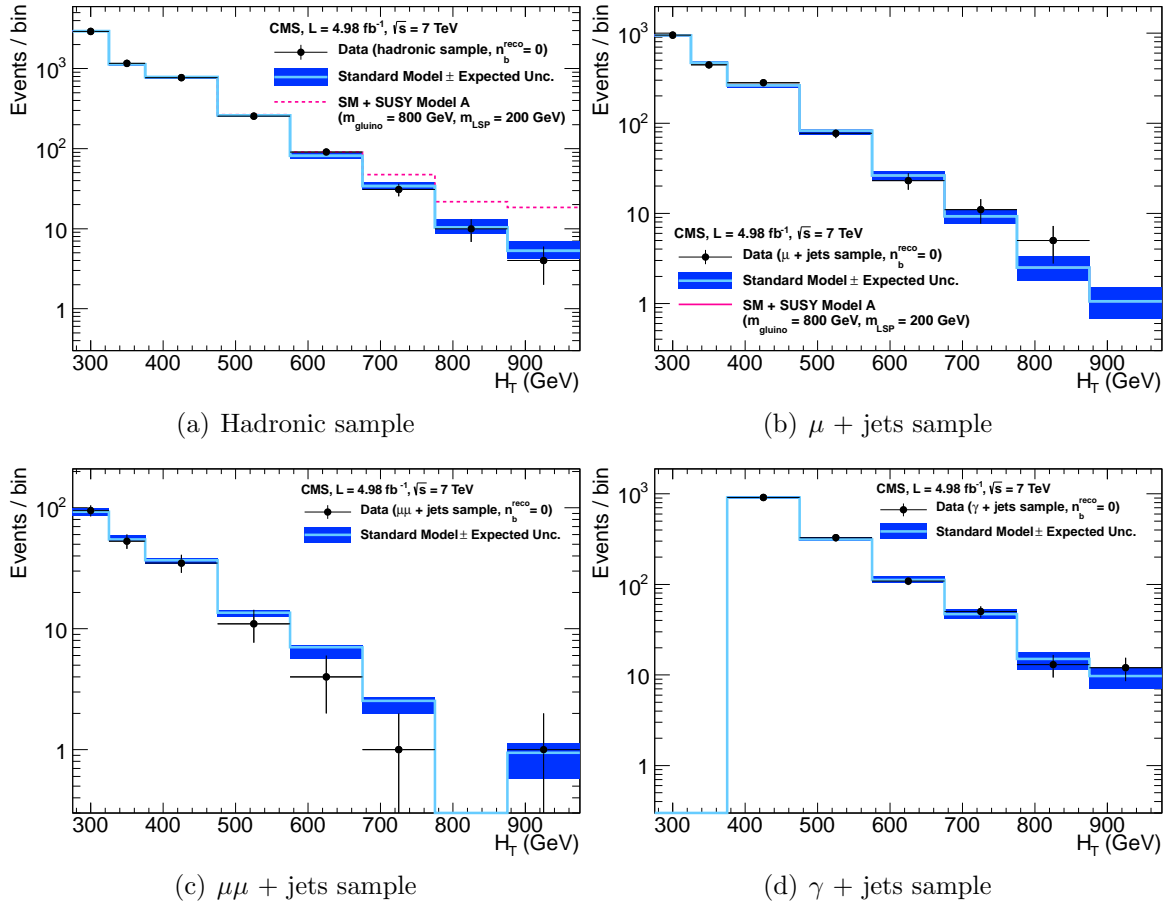


Figure 6.8.: Comparison of the observed yields and SM expectations given by the simultaneous fit in bins of H_T for the (a) hadronic, (b) $\mu +$ Jets, (c) $\mu\mu +$ Jets and (d) $\gamma +$ Jets samples when requiring exactly zero reconstructed b-jets. The observed event yields in data (black dots) and the expectations and their uncertainties, as determined by the simultaneous fit, for all SM processes (light blue solid line with dark blue bands) are shown. For illustrative purposes only, an example signal model is superimposed on the SM expectation (magenta solid line). The expected signal contamination in the control samples is negligible.

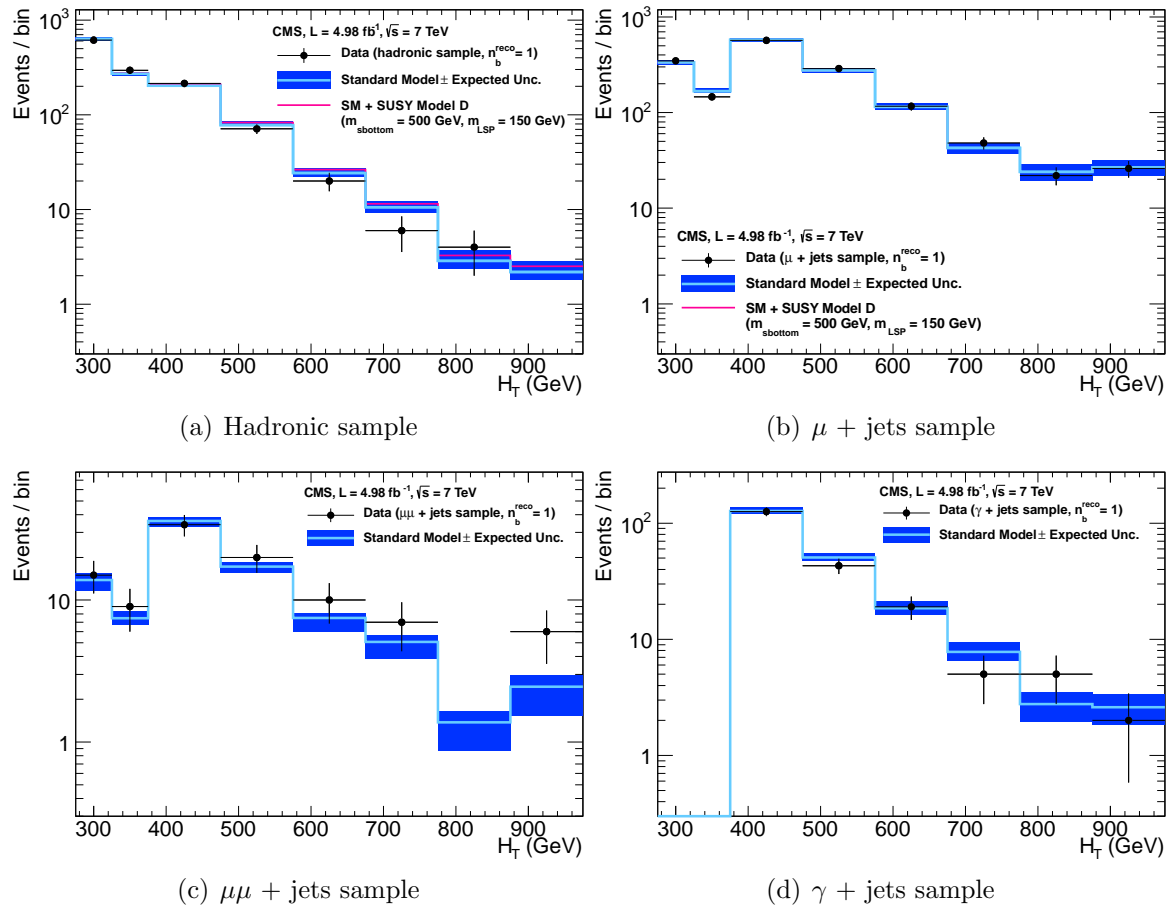


Figure 6.9.: Comparison of the observed yields and SM expectations given by the simultaneous fit in bins of H_T for the (a) hadronic, (b) $\mu + \text{Jets}$, (c) $\mu\mu + \text{Jets}$ and (d) $\gamma + \text{Jets}$ samples when requiring exactly one reconstructed b-jet. The observed event yields in data (black dots) and the expectations and their uncertainties, as determined by the simultaneous fit, for all SM processes (light blue solid line with dark blue bands) are shown. For illustrative purposes only, an example signal model is superimposed on the SM expectation (magenta solid line). The expected signal contamination in the control samples is negligible.

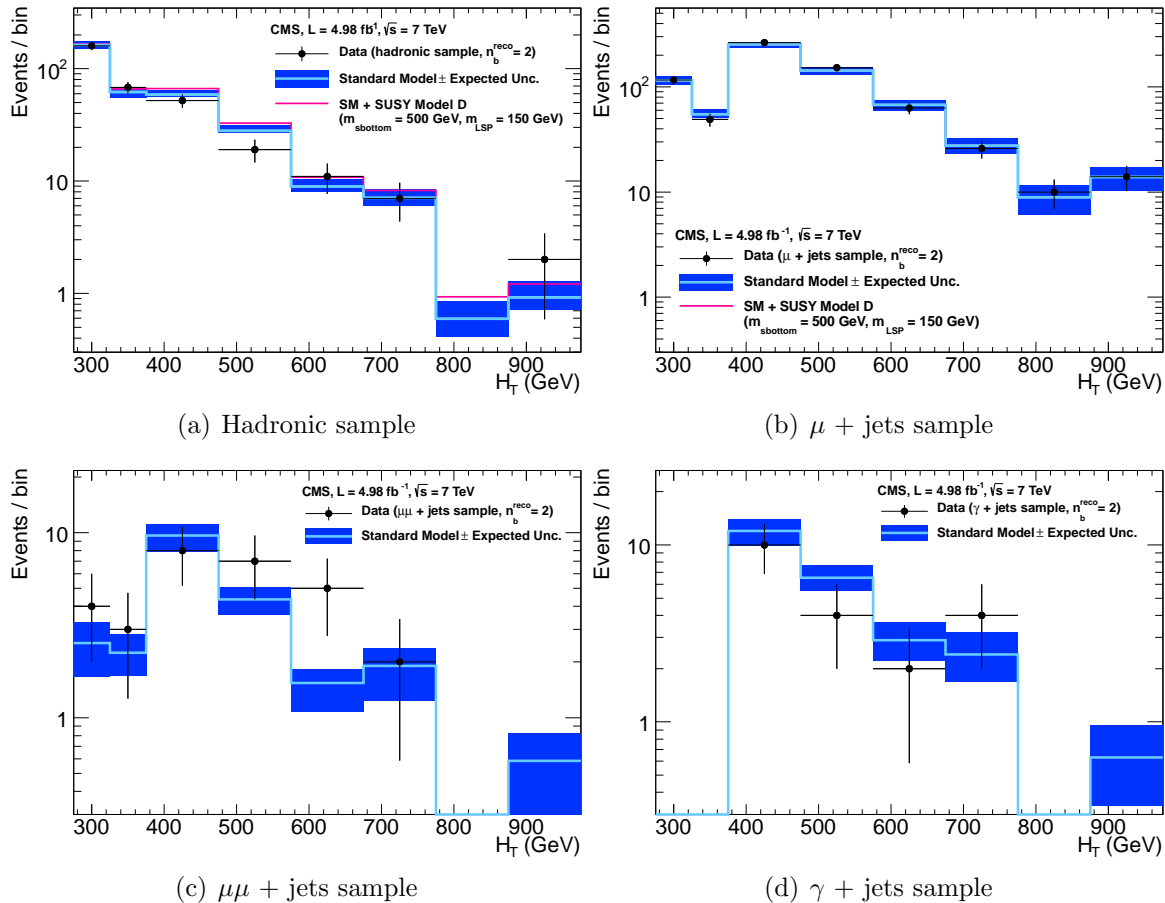


Figure 6.10.: Comparison of the observed yields and SM expectations given by the simultaneous fit in bins of H_T for the (a) hadronic, (b) $\mu + \text{Jets}$, (c) $\mu\mu + \text{Jets}$ and (d) $\gamma + \text{Jets}$ samples when requiring exactly two reconstructed b-jets. The observed event yields in data (black dots) and the expectations and their uncertainties, as determined by the simultaneous fit, for all SM processes (light blue solid line with dark blue bands) are shown. For illustrative purposes only, an example signal model is superimposed on the SM expectation (magenta solid line). The expected signal contamination in the control samples is negligible.

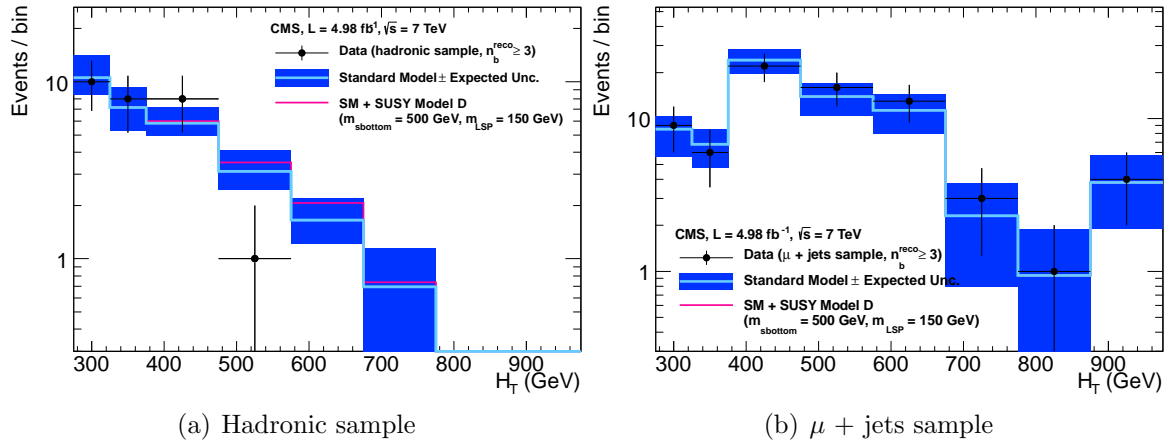


Figure 6.11.: Comparison of the observed yields and SM expectations given by the simultaneous fit in bins of H_T for the (a) hadronic and (b) $\mu +$ Jets samples when requiring at least three reconstructed b-jets. The observed event yields in data (black dots) and the expectations and their uncertainties, as determined by the simultaneous fit, for all SM processes (light blue solid line with dark blue bands) are shown. For illustrative purposes only, an example signal model is superimposed on the SM expectation (magenta solid line). The expected signal contamination in the $\mu +$ Jets control sample is negligible.

Chapter 7.

Interpretation

7.1. Signal Models

In the absence of a signal, the data may be used to constrain possible models of physics beyond the SM.

The SUSY model considered is the CMSSM[37] which is described in Section 2.2.1, the parameters chosen are $\tan \beta = 10$, $A_0 = 0$ GeV, $\mu > 0$ with the exclusion curve presented in the m_0 , $m_{1/2}$ plane. This model combines many production and decay topologies and is common to results shown by previous and contemporary experiments [79, 80, 81, 82, 83, 84, 85, 86, 87, 88, 89, 90, 91, 92]. The results are also presented in terms of SMS models, these are models with single production methods and a specified decay topology. The CMS terminology for the production methods are as follows: T1 models are gluino-gluino production, which then decay to four SM hadronic jets and two neutralinos. T2 models are squark-squark production with decays to two SM hadronic jets and two neutralinos. These topologies can be further specialised by enforcing the squarks or gluinos to decay to heavy flavour SM quarks, such as t, which promptly decay to jets containing b quarks or direct decays to b quarks. The limits on the SMS space are defined in terms of the mass splitting between the neutralino and the pair produced SUSY particle defining the model.

7.2. Signal Efficiency

7.2.1. CMSSM

The CMSSM signal scan is composed of eight sub-processes which define the production and decay topologies. At leading order the cross sections for these topologies are $\frac{1}{8} \times \sigma_{\text{Tot}}$, however at higher Next to Leading Order (NLO) the relative contribution from each subprocess changes from point to point in $m_0, m_{1/2}$, as does the production cross section. To obtain the final next to leading order cross sections a set of multiplicative \parallel -factors are applied to the individual process cross sections. To achieve the correct summation of the individual process efficiencies, the analysis is run over each sub process in turn with the final efficiency given by the weighted sum of the sub-process efficiencies, weighted by the relative contribution given at NLO. These \parallel -factors are calculated using centrally and used though out the CMS SUSY analysis groups. The yield per point is then given by $\epsilon \times \mathcal{L}$ for 5 fb^{-1} and the total yields are show in the appendix in Figure E.1. These yields are for the sum of the H_T analysis bins.

7.2.2. Simplified Models

The SMS models which are described in Section 2.2.2 contain only one production process and a set decay topology, making the interpretation in these models simpler, however the individual models are not representative of a more complete SUSY model. Instead these models allow the testing of specific facets of new physics models, without the ambiguity of the relative contributions of each sub process at a point which is seen when testing full models. The efficiency is measured for each of the models, with the yield per point given by $\epsilon \times \sigma \times \mathcal{L}$ where an upper limit on σ can be computed. Additionally assuming some σ from theory allows the setting of a limit in terms of the particle masses. The selection efficiencies for several such models are shown in the Appendix E. Table 7.1 lists which figure corresponds to which model, it is to be noted that the total efficiency summed over H_T bins is shown.

Table 7.1.: Production and decay modes for various simplified models.

Model	Production and decay modes	Figure showing efficiency
T1	$\tilde{g}\tilde{g} \rightarrow q\bar{q}\tilde{\chi}^0 q\bar{q}\tilde{\chi}^0$	E.2
T2	$\tilde{q}\tilde{q} \rightarrow q\tilde{\chi}^0 \bar{q}\tilde{\chi}^0$	E.3
T2tt	$\tilde{t}\tilde{t} \rightarrow t\tilde{\chi}^0 \bar{t}\tilde{\chi}^0$	E.4
T2bb	$\tilde{b}\tilde{b} \rightarrow b\tilde{\chi}^0 \bar{b}\tilde{\chi}^0$	E.5
T1tttt	$\tilde{g}\tilde{g} \rightarrow t\bar{t}\tilde{\chi}^0 t\bar{t}\tilde{\chi}^0$	E.6
T1bbbb	$\tilde{g}\tilde{g} \rightarrow b\bar{b}\tilde{\chi}^0 b\bar{b}\tilde{\chi}^0$	E.7

7.2.3. Signal Efficiency for the Background Selection

If the SUSY particles decay equally though standard model processes then the final states may involve muons which in the presence of a signal would over estimate the background from the control samples. To measure this, the background selection is applied to the signal models and the yields are taken into account in the final limit setting procedure. On average the background selection's efficiency on signal is $10\times$ lower than the efficiency in the hadronic signal region. This is shown for the model T1tttt in Figure E.8 where the largest number of muons of all the signal models are expected in the final state. The contamination in the n_b bins that drive the limit is on the order of 10 – 20%. Given the agreement with between the individual control samples this has the effect of adding an extra constraint on the data and improves the limit by around 3%.

7.3. Uncertainty on Signal Efficiency

The systematic uncertainty on the signal models due to the following are considered: choice of PDF at generator level, the PDF set used to generate the sample has effects on both the acceptance and the production cross section; the measurement of the integrated luminosity is accounted for in the signal yield; due to the signal models being created with CMS FastSim[93] rather than CMS FullSim[94] the acceptance differs between the signal and the background samples; The error on the jet energy scale is accounted for on the signal yield; Systematic errors from the cleaning cuts (R_{miss} and ECAL dead regions) and lepton/photon vetoes are also taken into account; Finally corrections to the b-tagging efficiency between the FullSim and the FastSim are applied as well as their errors.

Each of these uncertainties is expressed as a percentage change in the efficiency from the central value given by applying the full analysis to each signal model, the total systematic is given by summing the components in quadrature. In the following section the measurements of the error from each of these sources is detailed and summarised for the signal models considered at the end of the section.

The uncertainties for the CMSSM are determined in a band of ± 60 GeV in $m_{1/2}$ around the expected limit to confine the errors to the relevant part of the plane, in the very high $m_0, m_{1/2}$ area the jet energy scale causes large fluctuations due to the small mass splitting between the SUSY particles. For the SMS models two regions are defined, one “close” to the diagonal, which has small mass splitting and thus the effects of jet energy scale and PDF acceptance have a large impact on the analysis efficiency. A second “far” region is defined with large mass splitting and thus a small change on the analysis efficiency due to jet energy scale and PDF variations. The near and far regions are defined by:

$$m_{sq}(m_{gl}) - m_\chi > 350 \text{ GeV} \text{ and } m_{sq}(m_{gl}) > 475 \text{ GeV} \quad (7.1)$$

events passing these conditions are classified as being in the “far” region, those failing in the “close” region.

7.4. Choice of PDF set at generator level

The PDF set contains information on the interaction probabilities of the quark and gluons in the proton at different energies. The model used in the production of the Monte Carlo simulation has a direct impact on the kinematics of the final states, since the PDFs have been measured at lower energies than those found at the LHC the quark and gluon distributions have been extrapolated from the low energy regime, the uncertainty at high energy is thus significant. The uncertainties on acceptance due to the choice of PDF set used to generate the signal Monte Carlo are calculated in line with the PDF4LHC[95] working group recommendations. On the event level the individual weights are re-calculated by moving between PDF set, the weight is based on the energy at which the quarks or gluons interact and the form given by the PDF. This is done for the central value of the three considered PDF sets (CTEQ6.1[96], MSTW2008nlo68cl[40] and NNPDF2.0[97]) and for the variations of each of their errors. The change in analysis efficiency is measured per H_T bin, Figure 7.1 shows the deviation in efficiency per bin

for three example points in the CMSSM plane, the error bars represent the Root Mean Squared (RMS) of the spread of the efficiency inside each PDF set. It is to be noted that some bins show a large change in efficiency due to the choice of PDF set, however these are low efficiency bins where changes in yield of a few events has a large effect, the final result however is driven by the high efficiency bins, hence these large fluctuations can be ignored. The effects on the cross section are studied by re-calculating the NLO cross sections of each of the sub-processes for each choice of PDF set, this is done centrally by CMS, these changes in cross section are accounted for in the error band on the expected limit.

7.5. Effect of Jet Energy Scale Variations on Signal Efficiency

Section 5.1.1 describes the JEC and their uncertainties, which are derived in [58]. These uncertainties are dependent on the $|\eta|$ and E_T of the jet in question. To measure the impact of the individual jet energy corrections on signal acceptance, two additional selections are performed on the signal samples, the first with the energy of each jet in the event raised from the central value by 1σ of its uncertainty. The second with the energy decreased by 1σ , the relative change in efficiency with respect to the central value is then calculated for a signal point. The model dependent systematic is found from the 68th percentile of the 1D distribution of the absolute change in signal efficiency over each point in the model space. Figure F.1 shows the change in efficiency over the full $m_0, m_{1/2}$ plane for the CMSSM, at high $m_0, m_{1/2}$ the variation is large due to the primary production method of SUSY particles being Electroweak production of charginos in this region. These charginos then decay through a chain to the neutralino and SM particles. Due to the small mass splitting (compressed spectrum) between each of the charginos the jets produced are only just within the E_T acceptance. A small change of the individual jet E_T thus moves many jets in and out of acceptance causing a large change in analysis efficiency, hence only the region within ± 60 GeV around the expected limit in $m_{1/2}$ is considered when calculating the systematic for the CMSSM. The points close to the diagonal in the SMS models have compressed spectra and so are affected by the change in jet energy scale. Figures F.2 and F.3 show the effects of scaling the jet energies for the considered SMS models, Figures F.4 and F.5 show the 68% coverage of

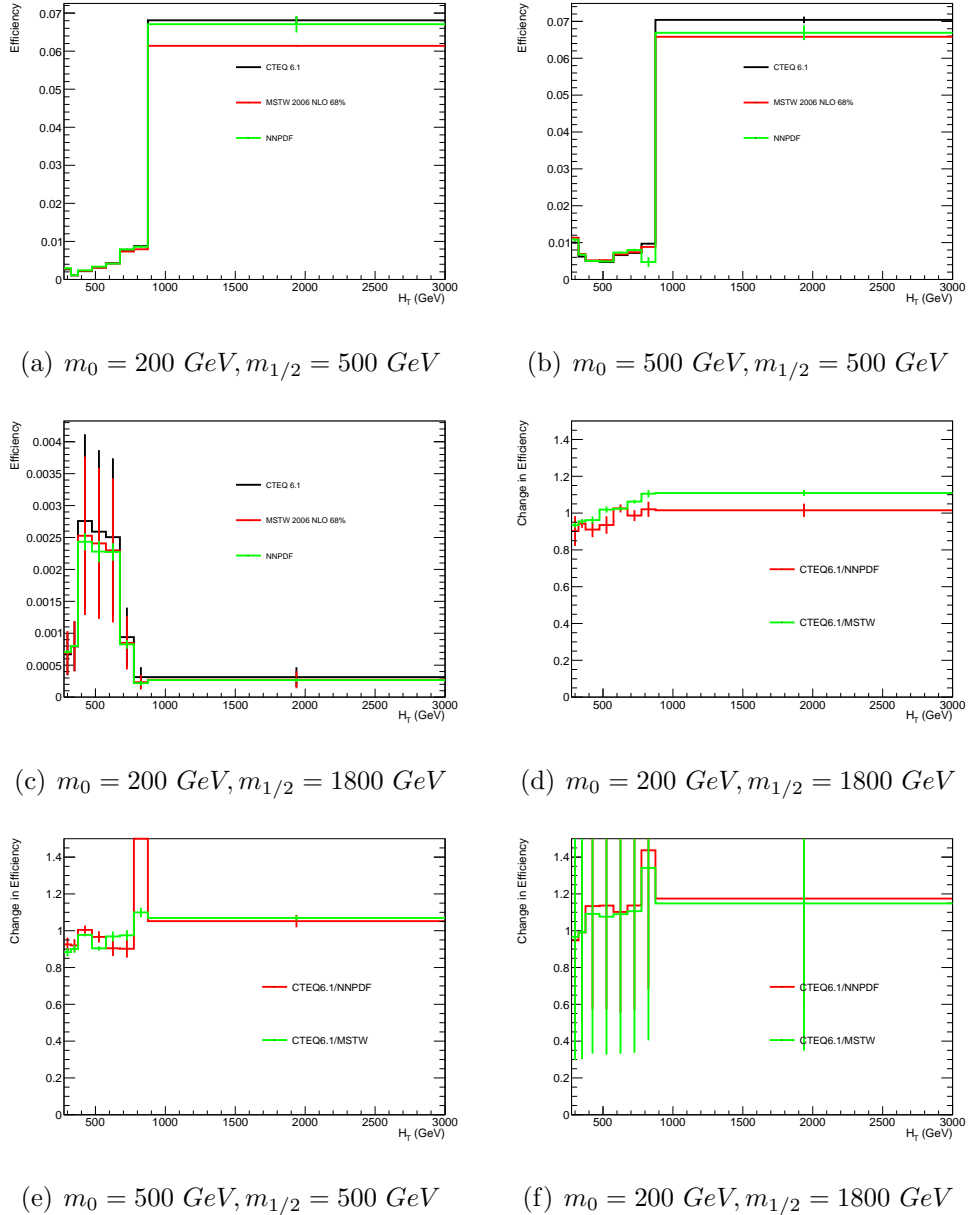


Figure 7.1.: Figures 7.1(a), 7.1(b) and 7.1(c) show the efficiency per H_T bin for the inclusive selection. The three coloured lines represent the analysis efficiency for a choice of PDF set, the error bars are the RMS of the change in efficiency per PDF set from varying the internal components by 1σ of their error. Figures 7.1(d), 7.1(e) and 7.1(f) show the ratio of the change in efficiency from the default PDF set (CTEQ6.1) for three illustrative points in the $m_0, m_{1/2}$ plane of the CMSSM. The change in efficiency in the high efficiency bins is of the order of 10% for all points.

the 1D distribution of the relative change in efficiency for the near and far regions from which the systematic is taken.

7.6. Systematic Uncertainty on Signal Yield from Cleaning Filters and Object Veto

For the cleaning cuts on R_{miss} and the Masked ECAL channel filter (`DeadECAL`) treatment which were described in Section 5.3, the systematic is given as the product of the ratio of normalised yields in the control samples, between data and Monte Carlo and the relative change in efficiency due to the cleaning filter for each individual signal model. The background sample is chosen before an α_T cut or any other cleaning cuts and is high in real \cancel{E}_T due to the selection of $W + \text{Jets}$ and $t\bar{t}$ events, meaning the efficiency of the R_{miss} cut should be high. Figure F.6 shows the accuracy of the R_{miss} modelling, at a cut value of $R_{miss} < 1.25$ the mis-modelling is at the level of 14%. Figures F.7, F.8 and F.9 show the change in selection efficiency due to the R_{miss} on the signal models.

As for the R_{miss} cut the background selection is performed on data and Monte Carlo and the accuracy of modelling the `DeadECAL` filter is measured, the ratio of the normalised cut efficiency on data and simulation shows a miss modelling at the level of 1.8%, this is taken as the uncertainty on the Monte Carlo model of the detector failures. Figures F.11, F.12 and F.13 show the relative change in efficiency due to the `DeadECAL` filter on the considered signal models.

Again regions with compressed spectra and many jet topologies are more effected by the cleaning cuts.

Finally the effects of the lepton vetoes on the signal efficiency are studied. A generator level filter is first applied removing any events with final state leptons or photons, thus measuring the effect of hadronic objects faking leptons or photons. The relative change in efficiency due to the application of the object vetoes is show in Figures F.15, F.17 and F.18, the inefficiency for each signal model are very small and are used directly as the systematic error.

7.7. Interpretation in terms of new physics models

Given the lack of a signal-like observation, limits are set on new physics models. The first of these is the CMSSM, at each point in the $m_0, m_{1/2}$ parameter space the SUSY particle spectrum is calculated using `SoftSUSY`[98], the signal events are generated at leading order using `Pythia 6.4`[99], the Next to Leading Order + Next Leading Log (NLO+NLL)

process dependent cross sections are calculated using PROSPINO[100] using the CTEQ6[96] PDF set. The previously measured errors on the background prediction, total collected luminosity and signal yield are included in the calculation of the limit. Although signal contributions from each data observation (hadronic, $\mu + \text{Jets}$, $\mu\mu + \text{Jets}$ and $\gamma + \text{Jets}$) are included, the only relevant signal contribution to the CMSSM is from the hadronic signal regions. Figure 7.2 shows the expected limit contour with its associated $\pm 1\sigma$ error band, which contains both statistical and systematic variations, as well as the observed limit. The limit is calculated using NLO+NLL cross sections using CL_s [101], the limit presented is for the 95% confidence level. For the choice of $\tan\beta = 10$, $A_0 = 0$ GeV, $\mu > 0$ and a top quark mass $m_{top} = 173.2$ GeV, squarks with masses below 1.25 TeV are excluded at 95% confidence, gluinos with a mass up to 1.25 TeV are also excluded when $m_0 < 600$ GeV. In the region $m_0 > 600$ GeV gluino masses below 700 GeV are excluded as are squarks with masses between 1.25-2.5 TeV, m_0 dependent. The limit in the low m_0 region is driven by topologies involving squark-squark production which causes two high E_T jets and large amounts of missing energy in the final state. The limit in the high m_0 region is along a line of constant gluino mass. At higher energies this curve would shift, keeping the same shape to higher values of m_0 and $m_{1/2}$.

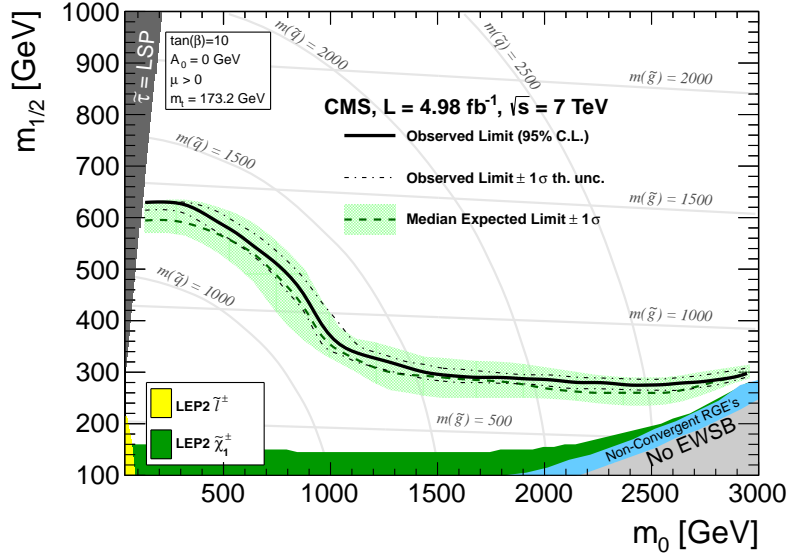


Figure 7.2.: Exclusion contours at 95% CL in the CMSSM ($m_0, m_{1/2}$) plane ($\tan\beta = 10, A_0 = 0, \mu > 0$) calculated with NLO+NLL SUSY production cross sections and the CL_s method. The solid black line indicates the observed exclusion region. The dotted-dashed black lines represent the observed excluded region when varying the cross section by its theoretical uncertainty. The expected median exclusion region (green dashed line) $\pm 1\sigma$ (green band) are also shown.

The observed yields are also used to set limits on SMS models. This allows interpretation of the results for a wide range of mass splittings and final states. Each SMS sample is characterised by the SUSY particle which is pair produced, either a squark or a gluino and the Lightest SUSY Particle (LSP) mass, the individual points are then defined by the mass difference between the pair produced particle and the LSP. The decay topologies are further specialised by enforcing the final state quarks to be heavy flavours, either top or bottom quarks. The decays of the models considered are summarised in Table 7.2.

As before the experimental uncertainties on the background estimation, collected luminosity, and the model dependent signal uncertainties are accounted for in the calculation of the limit.

In the regions $m_{\tilde{q}(\tilde{g})} - m_{LSP} < 200$ GeV and $m_{\tilde{q}(\tilde{g})} < 350$ GeV any selection efficiency is strongly dependent on the presence of initial state radiation which has a large associated uncertainty in the Monte Carlo simulation, hence these regions are not considered when setting limits in the SMS models. For the model **T1tttt** the ignored region is expanded to cover $m_{\tilde{g}} - m_{LSP} < 400$ GeV.

Figure 7.3 shows the observed limits at 95% confidence level obtained using CL_s as a function of $m_{\tilde{q}(\tilde{g})}$ and m_{LSP} . The solid black lines represent the observed median limit assuming NLO+NLL[100, 102] SUSY cross sections for squark pair production in the limit of de-coupled gluinos and vice versa for the gluino production models. The thin black lines represent the limit when this cross section is varied by $\pm 1\sigma$ of the theoretical uncertainty, the dashed purple lines represent the expected limit and its $\pm 1\sigma$ uncertainty.

The best limits are set on the mass of the pair produced sparticles are at low m_{LSP} due to the large mass splitting between the sparticles and the LSP producing high p_T final state objects. The limits degrade as the decay spectra become compressed, above a certain m_{LSP} no limit is set.

No exclusion on direct stop, stop production (**T2tt**) is expected assuming the NLO+NLL production cross section for $m_{LSP} > 50$ GeV. Figure 7.4 shows the observed upper limit at 95% confidence level on the cross section as a function of m_{stop} for an LSP with a mass of 50 GeV.

Table 7.2.: Production and decay modes for various simplified models.

Model	Production and decay modes	Figure showing limit
T1	$\tilde{g}\tilde{g} \rightarrow q\bar{q}\tilde{\chi}^0 q\bar{q}\tilde{\chi}^0$	7.3(a)
T2	$\tilde{q}\tilde{q} \rightarrow q\tilde{\chi}^0 \bar{q}\tilde{\chi}^0$	7.3(b)
T2tt	$\tilde{t}\tilde{t} \rightarrow t\tilde{\chi}^0 \bar{t}\tilde{\chi}^0$	7.3(c), 7.4
T2bb	$\tilde{b}\tilde{b} \rightarrow b\tilde{\chi}^0 \bar{b}\tilde{\chi}^0$	7.3(d)
T1tttt	$\tilde{g}\tilde{g} \rightarrow t\bar{t}\tilde{\chi}^0 t\bar{t}\tilde{\chi}^0$	7.3(e)
T1bbbb	$\tilde{g}\tilde{g} \rightarrow b\bar{b}\tilde{\chi}^0 b\bar{b}\tilde{\chi}^0$	7.3(f)

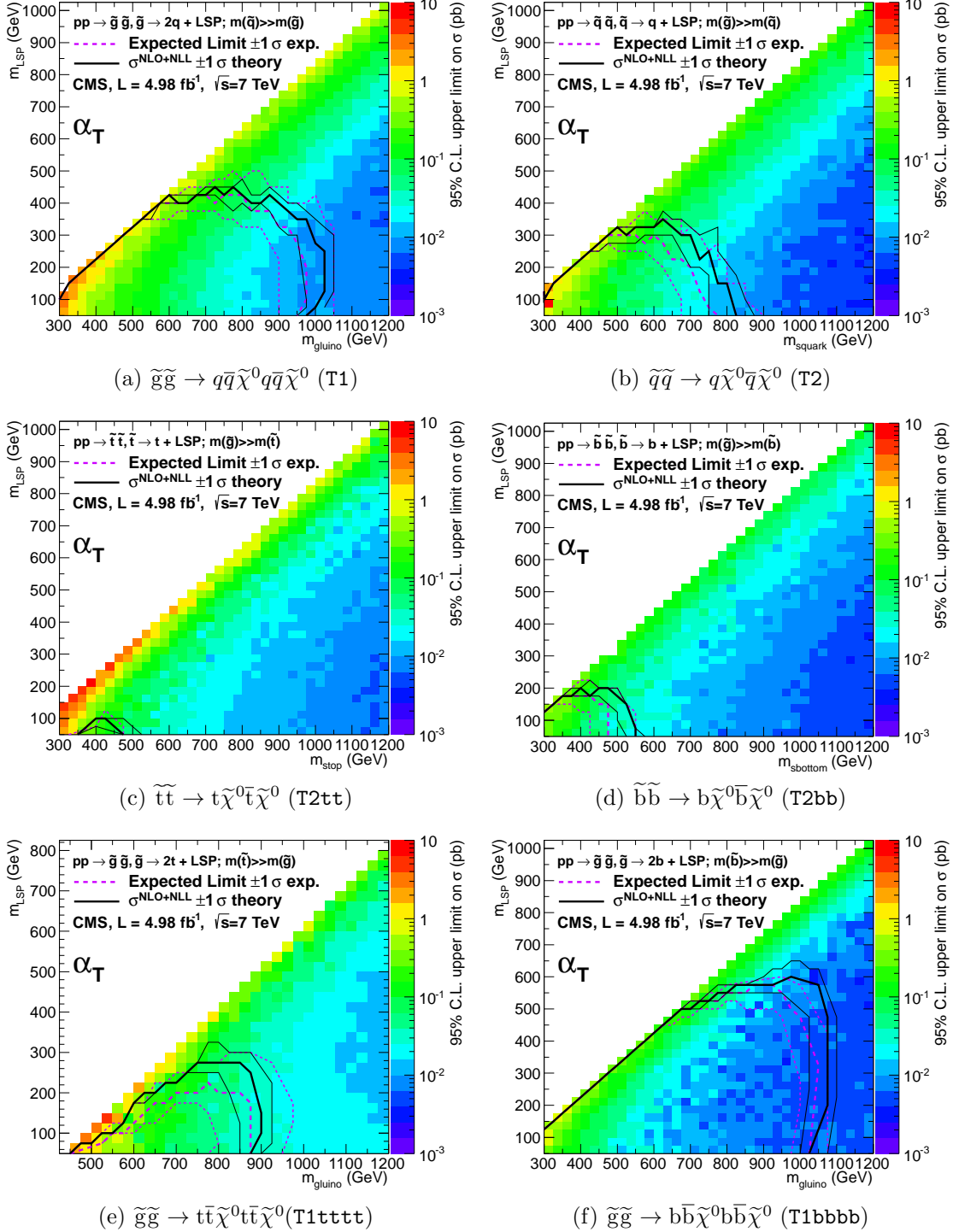


Figure 7.3.: Upper limit on cross section at 95% CL as a function of $m_{\tilde{g}}$ or $m_{\tilde{q}}$ and m_{LSP} for various simplified models. The solid thick black line indicates the observed exclusion region assuming NLO+NLL SUSY production cross section. The thin black lines represent the observed excluded region when varying the cross section by its theoretical uncertainty. The dashed purple lines indicate the median (thick line) $\pm 1\sigma$ (thin lines) expected exclusion regions.

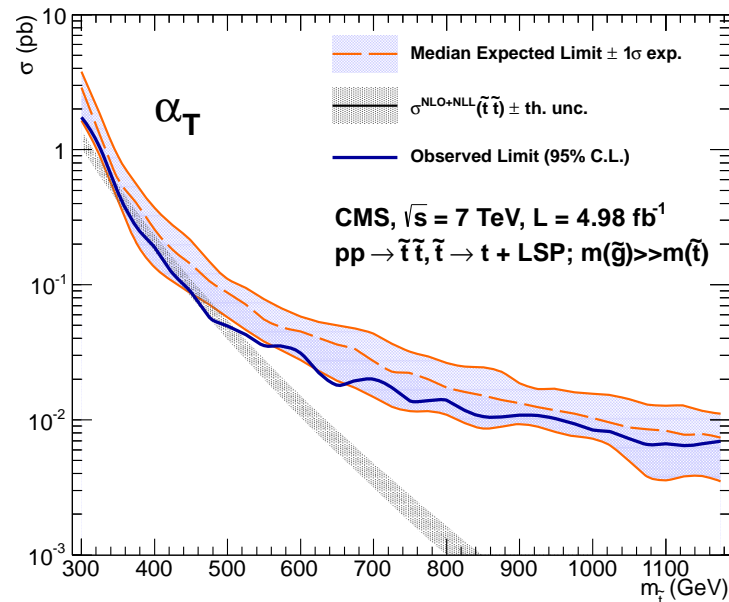


Figure 7.4.: Excluded cross section versus top squark mass for a model in which pair-produced top squarks decay to two top quarks and two neutralinos. The solid blue line indicates the observed cross section upper limit (95% CL) as a function of the top squark mass, $m_{\tilde{t}}$. The dashed orange line and blue band indicate the median expected excluded cross section with experimental uncertainties. The solid black line with grey band indicates the NLO+NLL SUSY top squark pair-production cross section and theoretical uncertainties.

Chapter 8.

Conclusion

A search for SUSY in the all hadronic channel using α_T has been presented. The measurement of the Level-1 trigger efficiencies relevant for an all hadronic SUSY search have been presented. In the region of interest these triggers have efficiencies greater than 95%. A suite of high level triggers are presented. These triggers are analysis specific cutting on the α_T variable and the sum of the hadronic energy in the event, H_T . This allows data collection at very low H_T compared to other HLT trigger paths, whilst maintaining a low trigger rate. The low H_T region is important for SUSY searches considering models with compressed spectra as the total visible energy in the event is small. The efficiencies of these triggers are measured to high precision and these efficiencies and the error on them are taken into account in the final search. Biases and errors due to theory, detector effects and analysis choices are quantified and the impact of these uncertainties is accounted for in the final interpretation. The total SM background is estimated from a data control sample and the final number of events in the signal selection does not deviate significantly from this prediction.

In the absence of a signal like excess the search is interpreted in two ways, firstly the compatibility with the SM only prediction, a high level of compatibility was observed. With a null result limits on the production cross section and masses of new physics models which involve a dark matter candidate are set, these results are summarised in Table 8.1 for the simplified models. In the case of the CMSSM squarks and gluinos with masses up to 1 TeV are excluded.

Table 8.1.: The first three columns define the production and decay modes for various simplified models. The last two columns indicate the search sensitivity for these models, where $m_{\tilde{q}(\tilde{g})}^{\text{best}}$ and $m_{\text{LSP}}^{\text{best}}$ represent the largest mass beyond which no limit can be set for squarks/gluinos and the LSP, respectively[56].

Model	Production and decay modes	Figure	$m_{\tilde{q}(\tilde{g})}^{\text{best}}$ (GeV)	$m_{\text{LSP}}^{\text{best}}$ (GeV)
A	$\text{pp} \rightarrow \tilde{g}\tilde{g} \rightarrow q\bar{q}\tilde{\chi}^0 q\bar{q}\tilde{\chi}^0$	7.3(a)	≈ 950	≈ 400
B	$\text{pp} \rightarrow \tilde{q}\tilde{q} \rightarrow q\tilde{\chi}^0 \bar{q}\tilde{\chi}^0$	7.3(b)	≈ 750	≈ 275
C	$\text{pp} \rightarrow \tilde{t}\tilde{t} \rightarrow t\tilde{\chi}^0 \bar{t}\tilde{\chi}^0$	7.3(c)	—	—
D	$\text{pp} \rightarrow \tilde{b}\tilde{b} \rightarrow b\tilde{\chi}^0 \bar{b}\tilde{\chi}^0$	7.3(d)	≈ 500	≈ 175
E	$\text{pp} \rightarrow \tilde{g}\tilde{g} \rightarrow t\bar{t}\tilde{\chi}^0 t\bar{t}\tilde{\chi}^0$	7.3(e)	≈ 850	≈ 250
F	$\text{pp} \rightarrow \tilde{g}\tilde{g} \rightarrow b\bar{b}\tilde{\chi}^0 b\bar{b}\tilde{\chi}^0$	7.3(f)	≈ 1025	≈ 550

Appendix A.

Maximum likelihood yields

Table A.1.: Comparison of the measured yields in the different H_T bins of the hadronic and control samples with the SM expectations and combined statistical and systematic uncertainties given by the simultaneous fit. Exactly zero b-tags per event are required.

H_T Bin (GeV)	275–325	325–375	375–475	475–575	575–675	675–775	775–875	875– ∞
SM hadronic	2933^{+56}_{-52}	1139^{+17}_{-40}	783^{+17}_{-27}	261^{+14}_{-8}	$81.5^{+6.5}_{-6.5}$	$34.2^{+4.0}_{-3.8}$	$10.4^{+2.8}_{-1.8}$	$5.3^{+1.7}_{-1.1}$
Data hadronic	2919	1166	769	255	91	31	10	4
SM μ +jets	940^{+26}_{-34}	466^{+25}_{-6}	262^{+9}_{-12}	$82.2^{+4.1}_{-6.6}$	$26.3^{+3.0}_{-3.2}$	$9.2^{+1.5}_{-1.6}$	$2.5^{+0.8}_{-0.7}$	$1.1^{+0.5}_{-0.4}$
Data μ +jets	949	444	281	77	23	11	5	0
SM $\mu\mu$ +jets	$93.1^{+6.6}_{-7.4}$	$54.9^{+4.4}_{-2.1}$	$36.8^{+1.8}_{-2.1}$	$13.6^{+0.7}_{-1.1}$	$7.0^{+0.3}_{-1.3}$	$2.5^{+0.2}_{-0.5}$	$0.1^{+0.0}_{-0.0}$	$0.9^{+0.2}_{-0.4}$
Data $\mu\mu$ +jets	95	53	35	11	4	1	0	1
SM γ +jets	—	—	913^{+33}_{-22}	314^{+13}_{-15}	112^{+9}_{-9}	$47.1^{+5.7}_{-5.4}$	$15.0^{+2.7}_{-3.5}$	$9.7^{+2.1}_{-2.6}$
Data γ +jets	—	—	909	328	109	50	13	12

Table A.2.: Comparison of the measured yields in the different H_T bins of the hadronic and control samples with the SM expectations and combined statistical and systematic uncertainties given by the simultaneous fit. Exactly one b-tag per event is required.

H_T Bin (GeV)	275–325	325–375	375–475	475–575	575–675	675–775	775–875	875– ∞
SM hadronic	630^{+26}_{-25}	271^{+10}_{-16}	202^{+10}_{-6}	$78.0^{+6.9}_{-1.9}$	$24.2^{+2.9}_{-2.0}$	$10.6^{+1.7}_{-1.3}$	$2.9^{+0.9}_{-0.5}$	$2.2^{+0.7}_{-0.4}$
Data hadronic	614	294	214	71	20	6	4	0
SM μ +jets	336^{+17}_{-19}	168^{+12}_{-7}	575^{+19}_{-22}	276^{+12}_{-17}	115^{+10}_{-9}	$42.6^{+5.5}_{-5.4}$	$24.0^{+4.6}_{-4.6}$	$26.8^{+4.7}_{-4.8}$
Data μ +jets	347	146	568	288	116	48	22	26
SM $\mu\mu$ +jets	$13.9^{+1.7}_{-2.2}$	$7.4^{+0.9}_{-0.8}$	$36.1^{+2.4}_{-3.0}$	$17.2^{+1.3}_{-1.6}$	$7.5^{+0.6}_{-1.5}$	$5.1^{+0.6}_{-1.2}$	$1.4^{+0.3}_{-0.5}$	$2.4^{+0.5}_{-0.9}$
Data $\mu\mu$ +jets	15	9	34	20	10	7	0	6
SM γ +jets	—	—	128^{+9}_{-8}	$50.7^{+4.1}_{-3.7}$	$18.5^{+2.8}_{-2.2}$	$7.8^{+1.6}_{-1.3}$	$2.8^{+0.8}_{-0.8}$	$2.6^{+0.8}_{-0.8}$
Data γ +jets	—	—	126	43	19	5	5	2

Table A.3.: Comparison of the measured yields in the different H_T bins of the hadronic and control samples with the SM expectations and combined statistical and systematic uncertainties given by the simultaneous fit. Exactly two b-tags per event are required.

H_T Bin (GeV)	275–325	325–375	375–475	475–575	575–675	675–775	775–875	875– ∞
SM hadronic	162^{+13}_{-12}	$61.8^{+4.8}_{-6.3}$	$58.8^{+4.8}_{-2.6}$	$28.0^{+3.5}_{-1.1}$	$9.0^{+1.4}_{-1.0}$	$7.1^{+1.4}_{-1.0}$	$0.6^{+0.3}_{-0.2}$	$0.9^{+0.4}_{-0.2}$
Data hadronic	160	68	52	19	11	7	0	2
SM μ +jets	116^{+10}_{-11}	$55.1^{+6.4}_{-4.5}$	254^{+13}_{-15}	143^{+10}_{-12}	$67.6^{+7.4}_{-7.6}$	$27.6^{+4.6}_{-4.6}$	$8.9^{+2.8}_{-2.8}$	$13.9^{+3.5}_{-3.5}$
Data μ +jets	116	49	264	152	63	26	10	14
SM $\mu\mu$ +jets	$2.5^{+0.8}_{-0.9}$	$2.2^{+0.6}_{-0.6}$	$9.7^{+1.5}_{-1.8}$	$4.4^{+0.7}_{-0.8}$	$1.5^{+0.3}_{-0.5}$	$1.9^{+0.5}_{-0.7}$	$0.2^{+0.1}_{-0.1}$	$0.6^{+0.2}_{-0.3}$
Data $\mu\mu$ +jets	4	3	8	7	5	2	0	0
SM γ +jets	—	—	$12.0^{+2.0}_{-2.1}$	$6.5^{+1.1}_{-1.1}$	$2.9^{+0.8}_{-0.7}$	$2.4^{+0.8}_{-0.7}$	$0.3^{+0.1}_{-0.1}$	$0.6^{+0.3}_{-0.3}$
Data γ +jets	—	—	10	4	2	4	0	0

Table A.4.: Comparison of the measured yields in the different H_T bins of the hadronic and control samples with the SM expectations and combined statistical and systematic uncertainties given by the simultaneous fit. At least three b-tags per event are required.

H_T Bin (GeV)	275–325	325–375	375–475	475–575	575–675	675–775	775–875	875– ∞
SM hadronic	$10.5^{+3.5}_{-2.2}$	$7.1^{+2.2}_{-1.8}$	$5.8^{+1.4}_{-0.9}$	$3.1^{+1.0}_{-0.7}$	$1.7^{+0.5}_{-0.4}$	$0.7^{+0.5}_{-0.4}$	$0.1^{+0.1}_{-0.1}$	$0.2^{+0.1}_{-0.1}$
Data hadronic	10	8	8	1	0	0	0	0
SM μ +jets	$8.5^{+1.8}_{-2.9}$	$6.8^{+1.7}_{-2.0}$	$24.1^{+4.1}_{-4.7}$	$13.9^{+3.1}_{-3.4}$	$11.3^{+3.2}_{-3.4}$	$2.3^{+1.5}_{-1.5}$	$0.9^{+0.9}_{-0.9}$	$3.8^{+1.9}_{-1.9}$
Data μ +jets	9	6	22	16	13	3	1	4

Offline H_T bin	Signal Trigger	Reference Trigger
275 GeV < H_T < 325 GeV	HLT-HT250_AlphaT0p53_v2	HLT_Mu15_HT200_v2
275 GeV < H_T < 325 GeV	HLT-HT250_AlphaT0p53_v3	HLT_Mu15_HT200_v3
275 GeV < H_T < 325 GeV	HLT-HT250_AlphaT0p53_v4	HLT_Mu15_HT200_v4
275 GeV < H_T < 325 GeV	HLT-HT250_AlphaT0p53_v5	HLT_Mu30_HT200_v1
275 GeV < H_T < 325 GeV	HLT-HT250_AlphaT0p55_v1	HLT_Mu5_HT200_v4
275 GeV < H_T < 325 GeV	HLT-HT250_AlphaT0p55_v2	HLT_Mu40_HT200_v4
275 GeV < H_T < 325 GeV	HLT-HT250_AlphaT0p58_v3	HLT_DoubleMu8_Mass8_HT200_v4
275 GeV < H_T < 325 GeV	HLT-HT250_AlphaT0p58_v3	HLT_DoubleMu8_Mass8_HT200_v5
275 GeV < H_T < 325 GeV	HLT-HT250_AlphaT0p60_v3	HLT_DoubleMu8_Mass8_HT200_v4
275 GeV < H_T < 325 GeV	HLT-HT250_AlphaT0p60_v3	HLT_DoubleMu8_Mass8_HT200_v5
325 GeV < H_T < 375 GeV	HLT-HT300_AlphaT0p52_v1	HLT_Mu5_HT200_v4
325 GeV < H_T < 375 GeV	HLT-HT300_AlphaT0p52_v2	HLT_Mu8_HT200_v4
325 GeV < H_T < 375 GeV	HLT-HT300_AlphaT0p52_v3	HLT_Mu15_HT200_v2
325 GeV < H_T < 375 GeV	HLT-HT300_AlphaT0p53_v3	HLT_Mu15_HT200_v3
325 GeV < H_T < 375 GeV	HLT-HT300_AlphaT0p53_v4	HLT_Mu15_HT200_v4
325 GeV < H_T < 375 GeV	HLT-HT300_AlphaT0p53_v5	HLT_Mu30_HT200_v1
325 GeV < H_T < 375 GeV	HLT-HT300_AlphaT0p53_v6	HLT_Mu40_HT200_v3
325 GeV < H_T < 375 GeV	HLT-HT300_AlphaT0p53_v6	HLT_Mu40_HT200_v4
325 GeV < H_T < 375 GeV	HLT-HT300_AlphaT0p54_v5	HLT_Mu40_HT300_v4
325 GeV < H_T < 375 GeV	HLT-HT300_AlphaT0p54_v5	HLT_Mu40_HT300_v5
325 GeV < H_T < 375 GeV	HLT-HT300_AlphaT0p55_v3	HLT_DoubleMu8_Mass8_HT200_v4
325 GeV < H_T < 375 GeV	HLT-HT300_AlphaT0p55_v3	HLT_DoubleMu8_Mass8_HT200_v5

Table B.1.: List of α_T triggers used in the lowest two offline H_T bins and the triggers used to collect the reference sample.

Offline H_T bin	Signal Trigger	Reference Trigger
375 GeV < H_T < 475 GeV	HLT-HT350_AlphaT0p51_v1	HLT_Mu5_HT200_v4
375 GeV < H_T < 475 GeV	HLT-HT350_AlphaT0p51_v2	HLT_Mu8_HT200_v4
375 GeV < H_T < 475 GeV	HLT-HT350_AlphaT0p51_v3	HLT_Mu15_HT200_v2
375 GeV < H_T < 475 GeV	HLT-HT350_AlphaT0p51_v4	HLT_Mu15_HT200_v3
375 GeV < H_T < 475 GeV	HLT-HT350_AlphaT0p51_v5	HLT_Mu15_HT200_v4
375 GeV < H_T < 475 GeV	HLT-HT350_AlphaT0p52_v1	HLT_Mu30_HT200_v1
375 GeV < H_T < 475 GeV	HLT-HT350_AlphaT0p52_v2	HLT_Mu40_HT200_v3
375 GeV < H_T < 475 GeV	HLT-HT350_AlphaT0p52_v2	HLT_Mu40_HT200_v4
375 GeV < H_T < 475 GeV	HLT-HT350_AlphaT0p53_v10	HLT_Mu40_HT300_v4
375 GeV < H_T < 475 GeV	HLT-HT350_AlphaT0p53_v10	HLT_Mu40_HT300_v5
475 GeV < H_T < 7 TeV	HLT-HT400_AlphaT0p51_v1	HLT_Mu5_HT200_v4
475 GeV < H_T < 7 TeV	HLT-HT400_AlphaT0p51_v2	HLT_Mu8_HT200_v4
475 GeV < H_T < 7 TeV	HLT-HT400_AlphaT0p51_v3	HLT_Mu15_HT200_v2
475 GeV < H_T < 7 TeV	HLT-HT400_AlphaT0p51_v4	HLT_Mu15_HT200_v3
475 GeV < H_T < 7 TeV	HLT-HT400_AlphaT0p51_v5	HLT_Mu15_HT200_v4
475 GeV < H_T < 7 TeV	HLT-HT400_AlphaT0p51_v6	HLT_Mu30_HT200_v1
475 GeV < H_T < 7 TeV	HLT-HT400_AlphaT0p51_v7	HLT_Mu40_HT200_v3
475 GeV < H_T < 7 TeV	HLT-HT400_AlphaT0p51_v7	HLT_Mu40_HT200_v4
475 GeV < H_T < 7 TeV	HLT-HT400_AlphaT0p51_v10	HLT_Mu40_HT300_v4
475 GeV < H_T < 7 TeV	HLT-HT400_AlphaT0p51_v10	HLT_Mu40_HT300_v5
475 GeV < H_T < 7 TeV	HLT-HT400_AlphaT0p52_v5	HLT_Mu40_HT300_v4
475 GeV < H_T < 7 TeV	HLT-HT400_AlphaT0p52_v5	HLT_Mu40_HT300_v5

Table B.2.: List of α_T triggers used in the $H_T > 375$ GeV bins and the triggers used to collect the reference sample.

H_T range	Trigger
275 GeV – 325 GeV	HLT-HT250_AlphaT0p55_v*
325 GeV – 375 GeV	HLT-HT300_AlphaT0p53_v*
375 GeV – 475 GeV	HLT-HT350_AlphaT0p52_v*
475 GeV – 8 TeV	HLT-HT400_AlphaT0p51_v*

Table B.3.: Triggers used to seed the analysis H_T bins during 2012 data taking.

Table B.4.: List of HT triggers used.

H_T bin (GeV)	Trigger
$275 < H_T < 325$	HLT-HT250_v*
$325 < H_T < 375$	HLT-HT300_v*
$375 < H_T < 475$	HLT-HT350_v*
$H_T > 475$	HLT-HT400_v*

Appendix B.

Additional information on triggers

Table B.5.: List of α_T triggers used.

$275 < H_T < 325 GeV$	$325 < H_T < 375 GeV$
HLT-HT250_AlphaT0p53_v*	HLT-HT300_AlphaT0p52_v*
HLT-HT250_AlphaT0p55_v*	HLT-HT300_AlphaT0p53_v*
HLT-HT250_AlphaT0p58_v*	HLT-HT300_AlphaT0p54_v*
HLT-HT250_AlphaT0p60_v*	HLT-HT300_AlphaT0p55_v*
$375 < H_T < 475 GeV$	$H_T > 475 GeV$
HLT-HT350_AlphaT0p51_v*	HLT-HT400_AlphaT0p51_v*
HLT-HT350_AlphaT0p52_v*	HLT-HT400_AlphaT0p52_v*
HLT-HT350_AlphaT0p52_v*	
HLT-HT350_AlphaT0p53_v*	

Table B.6.: List of Mu_T triggers used.

$H_T > 275 GeV$	$H_T > 375 GeV$
HLT_Mu5_HT200_v*	HLT_Mu5_HT200_v*
HLT_Mu8_HT200_v*	HLT_Mu8_HT200_v*
HLT_Mu15_HT200_v*	HLT_Mu15_HT200_v*
HLT_Mu30_HT200_v*	HLT_Mu30_HT200_v*
HLT_Mu40_HT200_v*	HLT_Mu40_HT200_v*
	HLT_Mu40_HT300_v*

Table B.7.: List of Photon triggers used.

$H_T > 375 GeV$
HLT_Photon75_CaloIdVL_v*
HLT_Photon75_CaloIdVL_IsoL_v*
HLT_Photon90_CaloIdVL_v*
HLT_Photon90_CaloIdVL_IsoL_v*
HLT_Photon125_v*
HLT_Photon135_v*

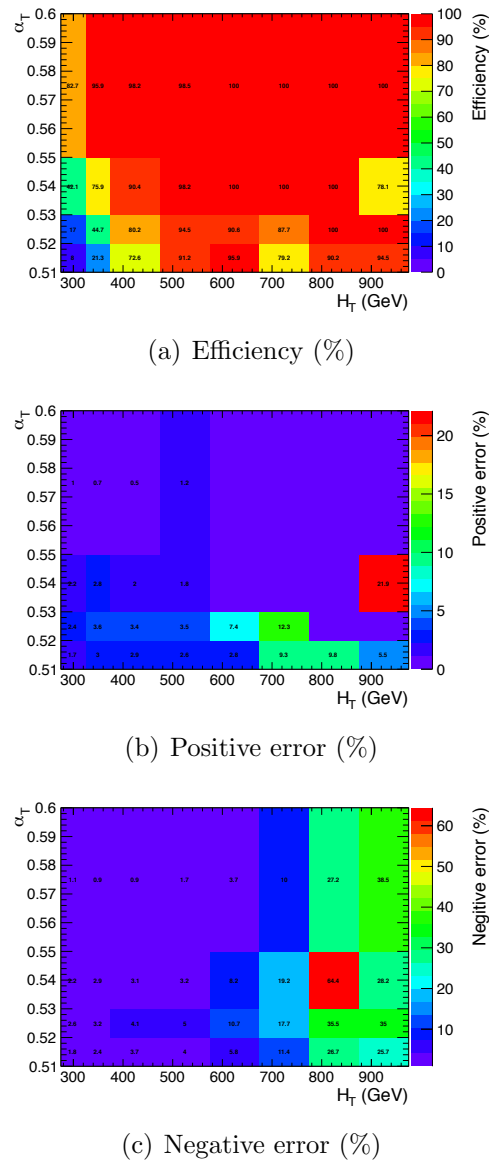


Figure B.1.: Efficiency and associated errors of the α_T trigger in offline bins of H_T and α_T .

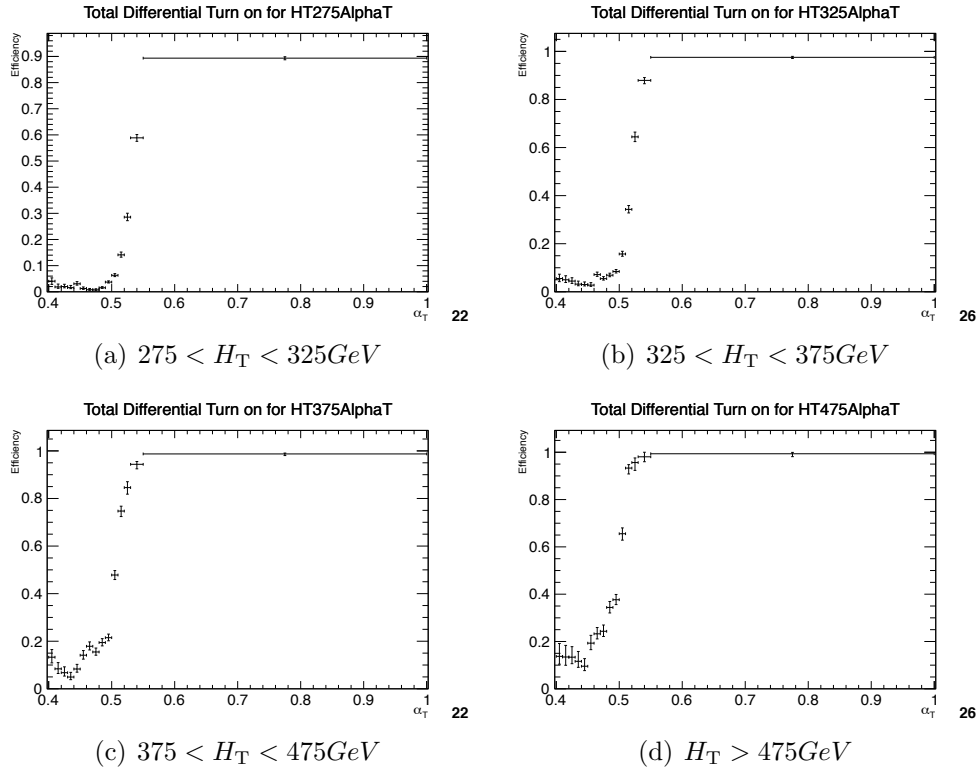


Figure B.2.: Efficiency turn-on curves for the α_T triggers used to collect events for four different H_T regions.

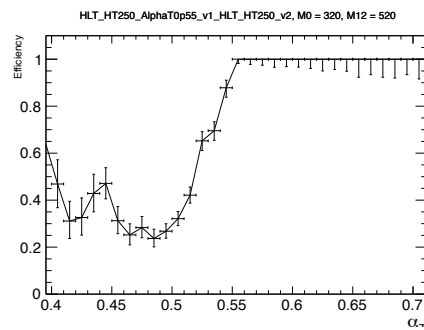


Figure B.3.: Efficiency turn-on curve for the representative model RM1, with $m_0 = 320 \text{ GeV}$ and $m_{1/2} = 520 \text{ GeV}$, using the α_T trigger with thresholds $H_T > 250 \text{ GeV}$ and $\alpha_T > 0.55$ and an offline signal region defined by $H_T > 275 \text{ GeV}$ and $\alpha_T > 0.55$.

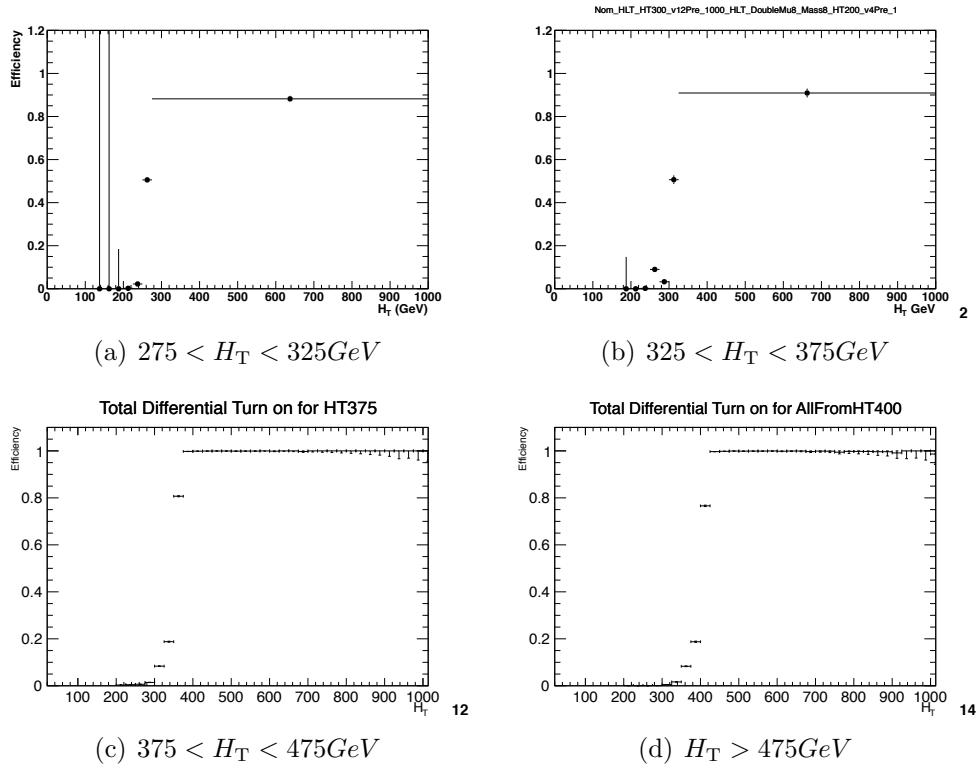


Figure B.4.: Efficiency turn-on curves for the H_T triggers used to collect events for four different HT regions.

Appendix C.

Addition information on background estimation methods

C.1. Determination of k_{QCD}

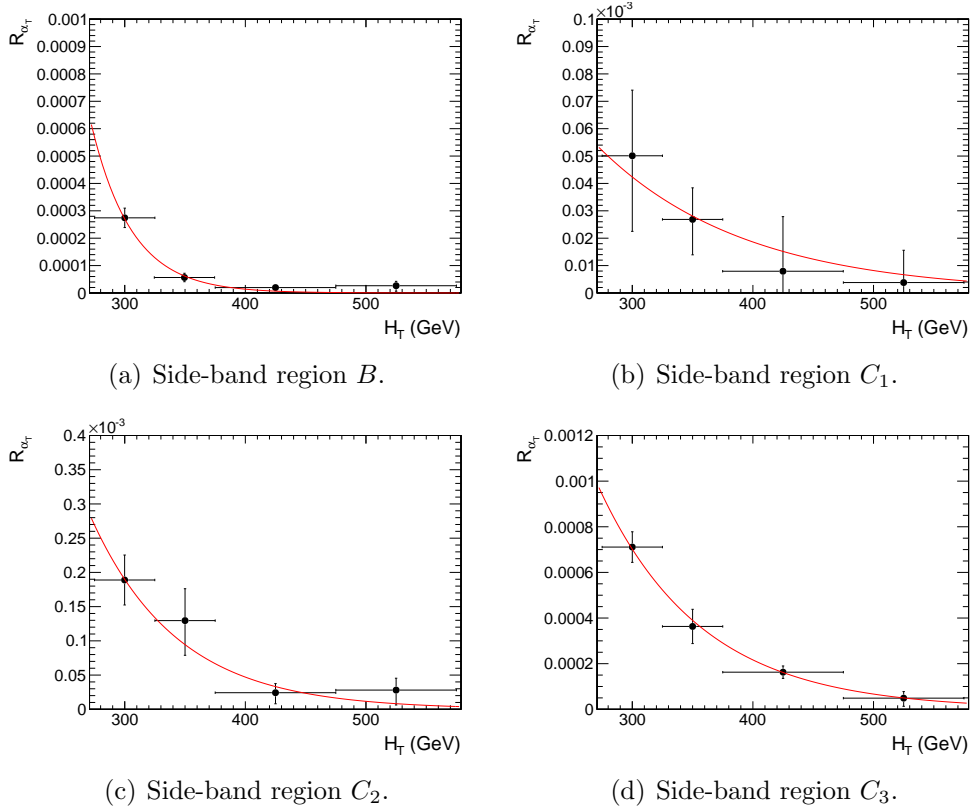


Figure C.1.: $R_{\alpha_T}(H_T)$ and exponential fit for various data side-bands. Linear y-axis scale.

Appendix D.

Closure tests and systematic uncertainties

D.1. Defining muon samples without an α_T requirement

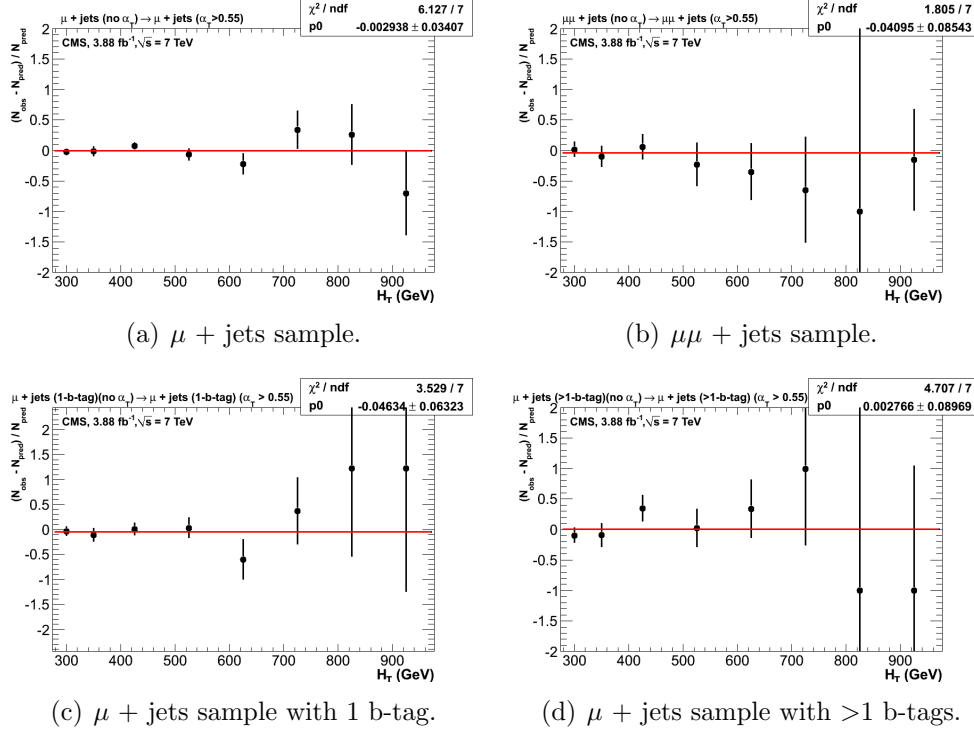


Figure D.1.: Closure tests that demonstrate the MC modelling of the α_T acceptance. The closure tests are performed for both the inclusive analysis with (a) the $\mu + \text{jets}$ sample and (b) the $\mu\mu + \text{jets}$ control sample. Similar tests are performed for the b-tag analysis using (a) the $\mu + \text{jets}$ sample and a requirement of exactly one b-tag, and (b) the $\mu + \text{jets}$ sample and a requirement of at least two b-tags. The red lines indicate the constant best fit value across all H_T bins.

D.2. Closure tests for inclusive analysis

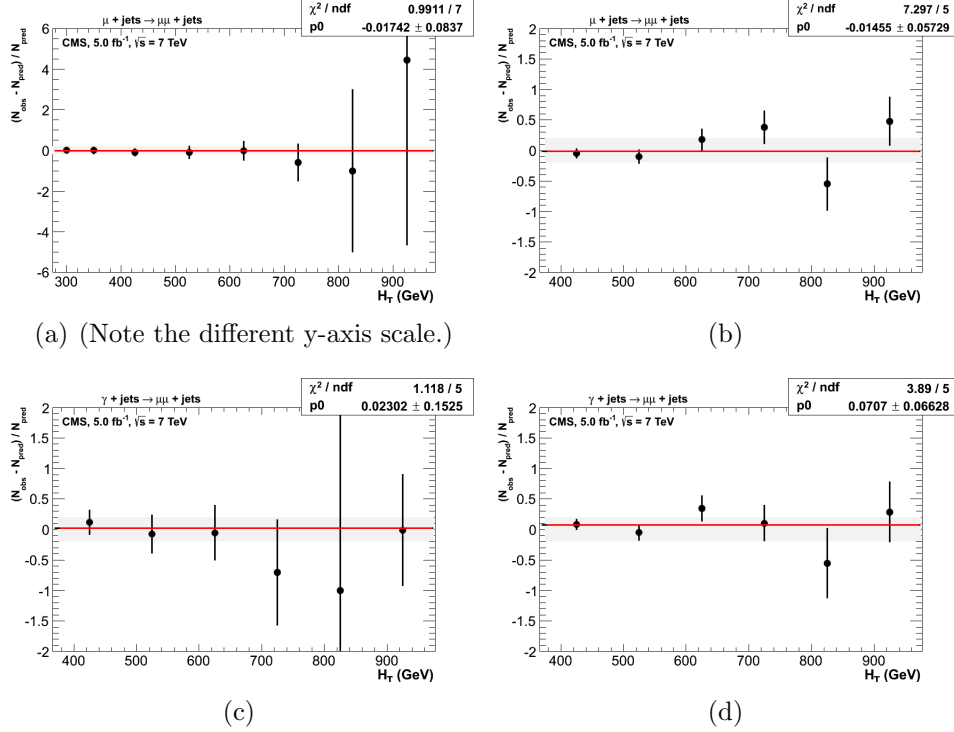
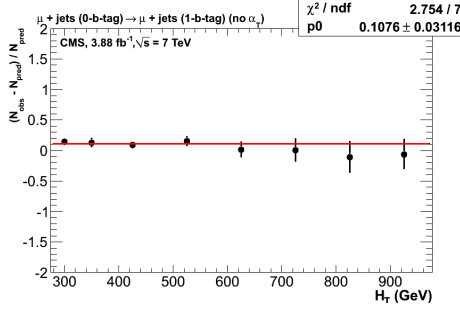


Figure D.2.: Closure tests using yields from one control to predict yields in another sample. The two plots on the left show closure tests which use “low stats” muon samples recorded with the `HT_AlphaT` triggers and defined by offline selection criteria that include an α_T requirement: (a) $\mu + \text{jets} \rightarrow \mu\mu + \text{jets}$ sample and (c) $\gamma + \text{jets} \rightarrow \mu\mu + \text{jets}$ sample. Similarly, the plots on the right show the same closure tests but using “high-stats” muon samples recorded with `Mu_HT` triggers and defined with no offline α_T requirement. The same tests are performed: (b) $\mu + \text{jets} \rightarrow \mu\mu + \text{jets}$ sample and (d) $\gamma + \text{jets} \rightarrow \mu\mu + \text{jets}$ sample. These closure tests are only possible for the six highest H_T bins due to the trigger conditions. The red lines indicate the constant best fit value across all H_T bins.

D.3. Closure tests for b-tag analysis



(a) 0 b-tags predicting 1 b-tag.

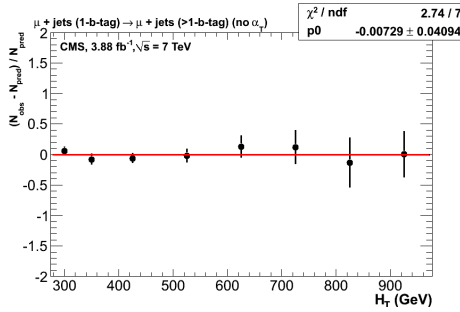
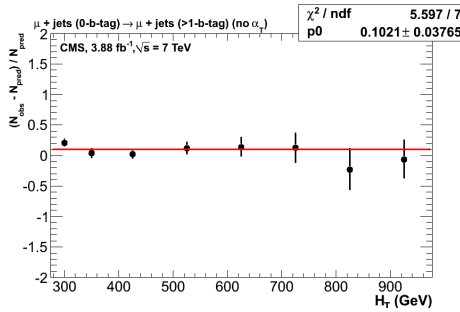
(b) 1 b-tag predicting >1 b-tags.(c) 0 b-tags predicting >1 b-tags.

Figure D.3.: Closure tests with the $\mu + \text{jets}$ sample that demonstrate the MC modelling of the b-tagging algorithm and of different sample compositions by for different b-tag multiplicities: (a) 0 b-tags \rightarrow 1 b-tag, (b) 1 b-tags \rightarrow ≥ 2 b-tags, (c) 0 b-tags \rightarrow ≥ 2 b-tags.

D.4. Closure tests concerning pile-up

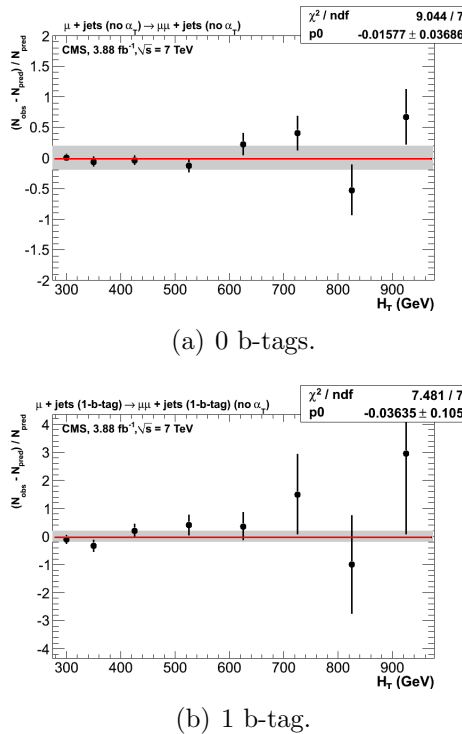


Figure D.4.: Closure tests using the $\mu + \text{jets}$ sample to predict the yields in a $\mu\mu + \text{jets}$ sample, for events with (a) exactly 0-b-tags and (b) exactly 1-b-tags.

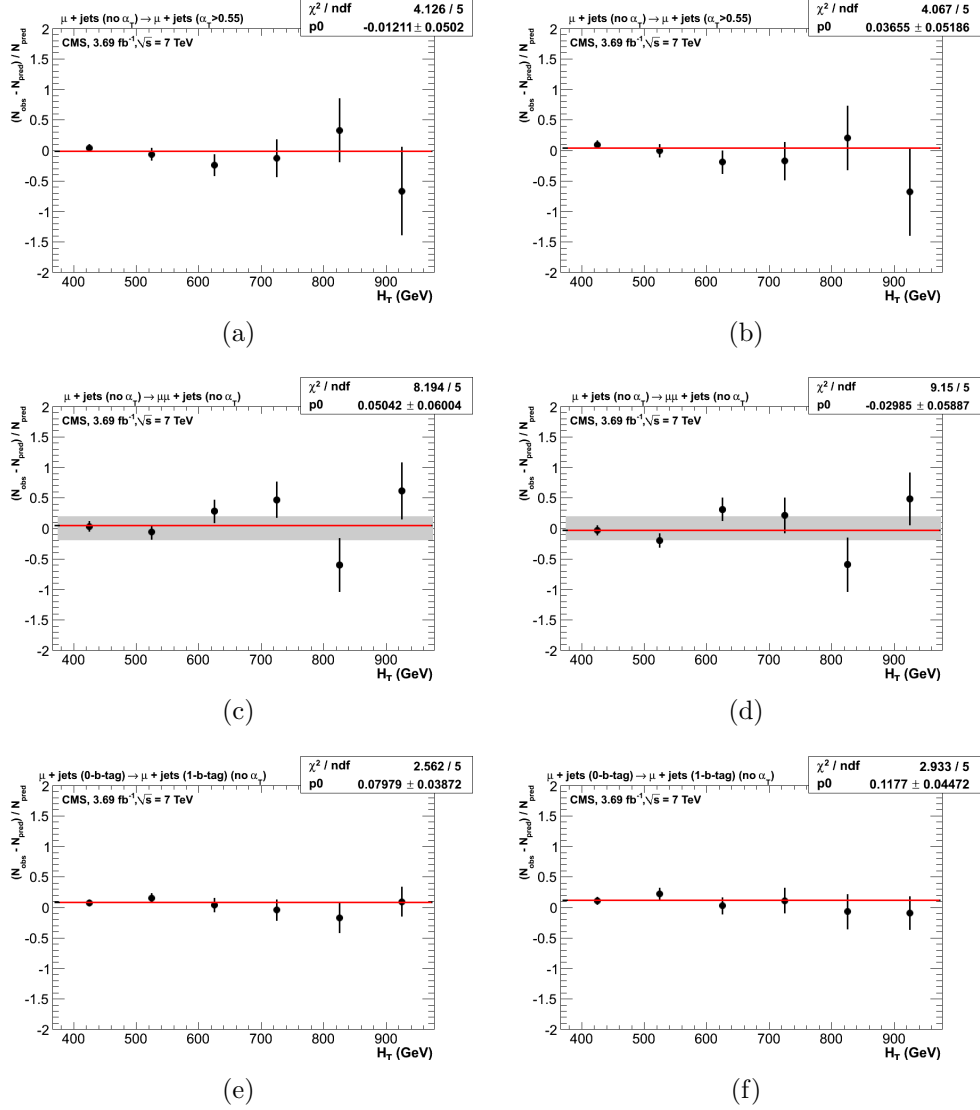


Figure D.5.: Closure tests using yields from one control to predict yields in another sample. The three plots on the left show closure tests from the inclusive analysis, which uses jets that are not corrected for the effects of pile-up. On the right, the jets in the analysis *are* corrected for pile-up effects by applying the L10offset jet energy correction. The three closure tests are: probing the MC modelling of the α_T acceptance with the $\mu + \text{jets}$ sample (a) without and (b) with L10offset jet energy corrections; using the $\mu + \text{jets}$ sample to predict yields in the $\mu\mu + \text{jets}$ sample (a) without and (b) with L10offset jet energy corrections; and using a 0 b-tagged $\mu + \text{jets}$ sample to predict yields in a 1 b-tagged $\mu + \text{jets}$ sample (a) without and (b) with L10offset jet energy corrections. The red lines indicate the constant best fit value across all H_T bins.

Appendix E.

Signal efficiency

Through out any missing spaces in the CMSSM plots are due to MC production failures. For the SMS models in the bins with high numbers of b jets the gaps are due to limited numbers of events being produced rather than failure of the MC production.

E.1. CMSSM

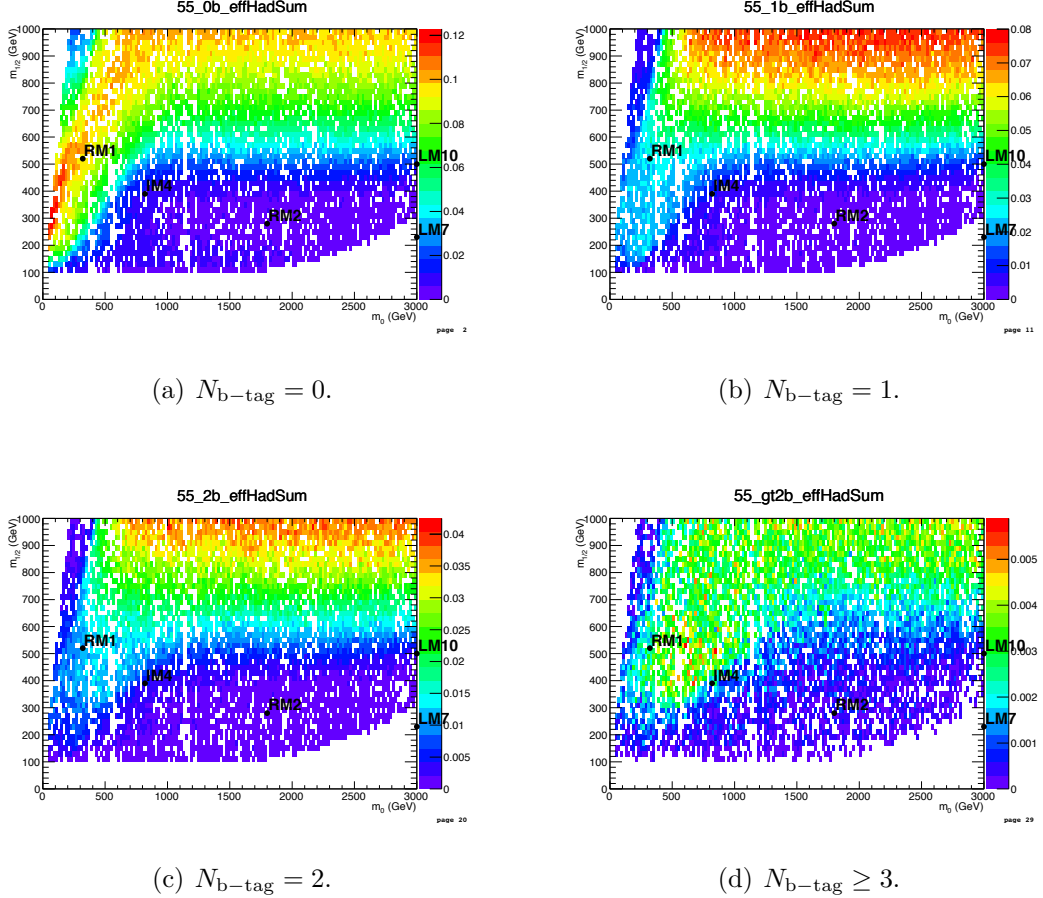


Figure E.1.: Signal efficiency in the $(m_0, m_{1/2})$ plane of the CMSSM, of the full hadronic signal selection, integrating over all eight H_T bins and requiring (a) exactly zero, (b) exactly one, (c) exactly two, and (d) at least three b-tags per event.

E.2. T1

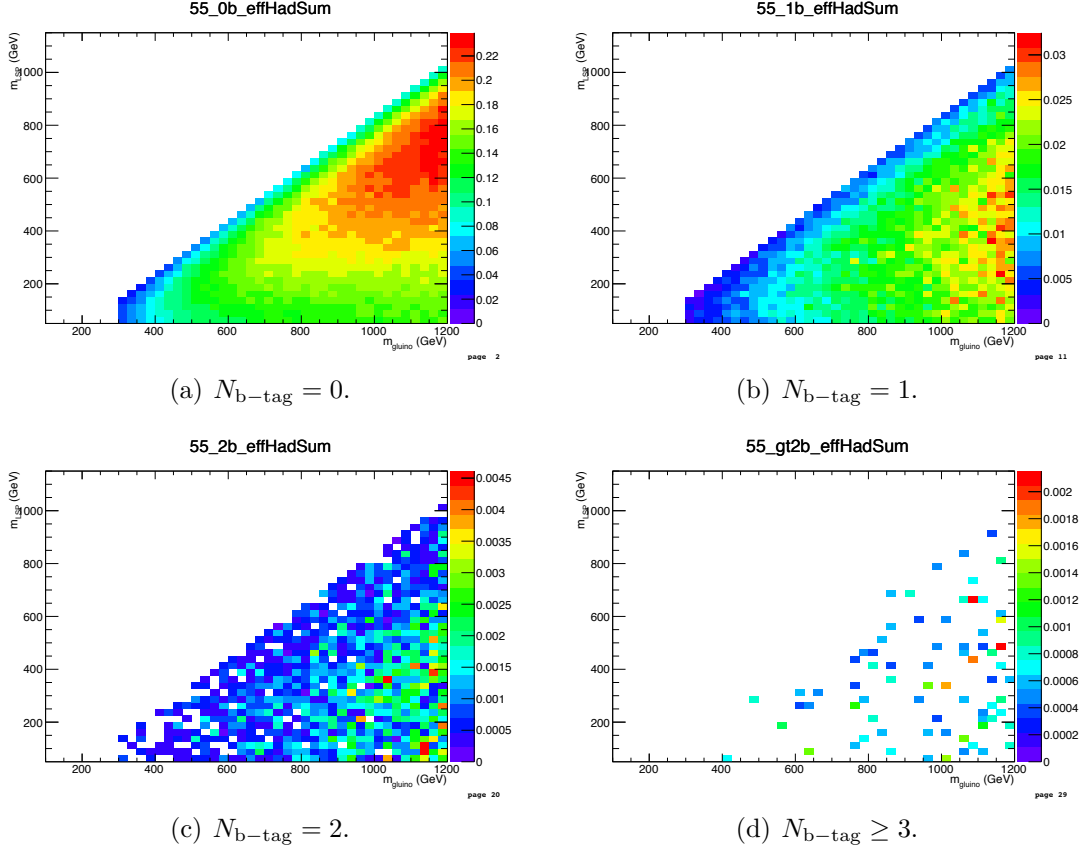


Figure E.2.: Signal efficiency in the $(m_{\text{glino}}, m_{\text{LSP}})$ plane of the T1 simplified model, of the full hadronic signal selection, integrating over all eight H_T bins and requiring (a) exactly zero, (b) exactly one, (c) exactly two, and (d) at least three b-tags per event.

E.3. T2

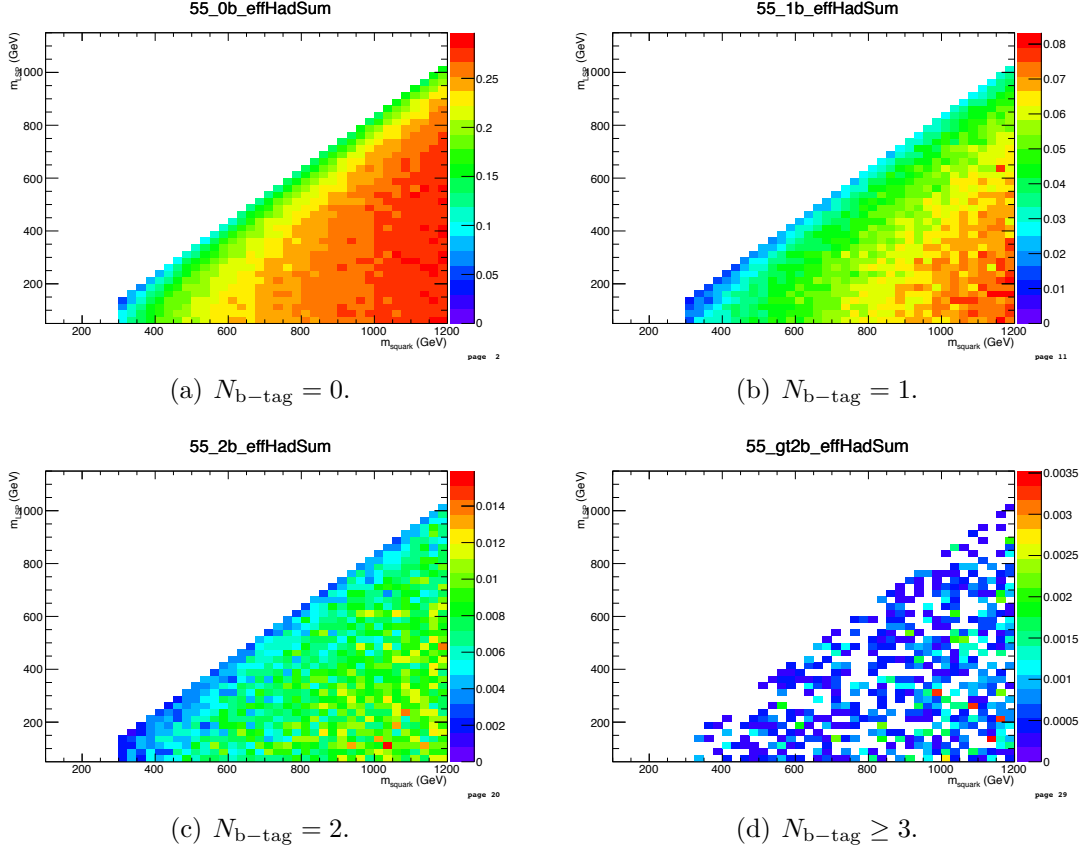


Figure E.3.: Signal efficiency in the $(m_{\text{sq}}, m_{\text{LSP}})$ plane of the T2 simplified model, of the full hadronic signal selection, integrating over all eight H_T bins and requiring (a) exactly zero, (b) exactly one, (c) exactly two, and (d) at least three b-tags per event.

E.4. T2tt

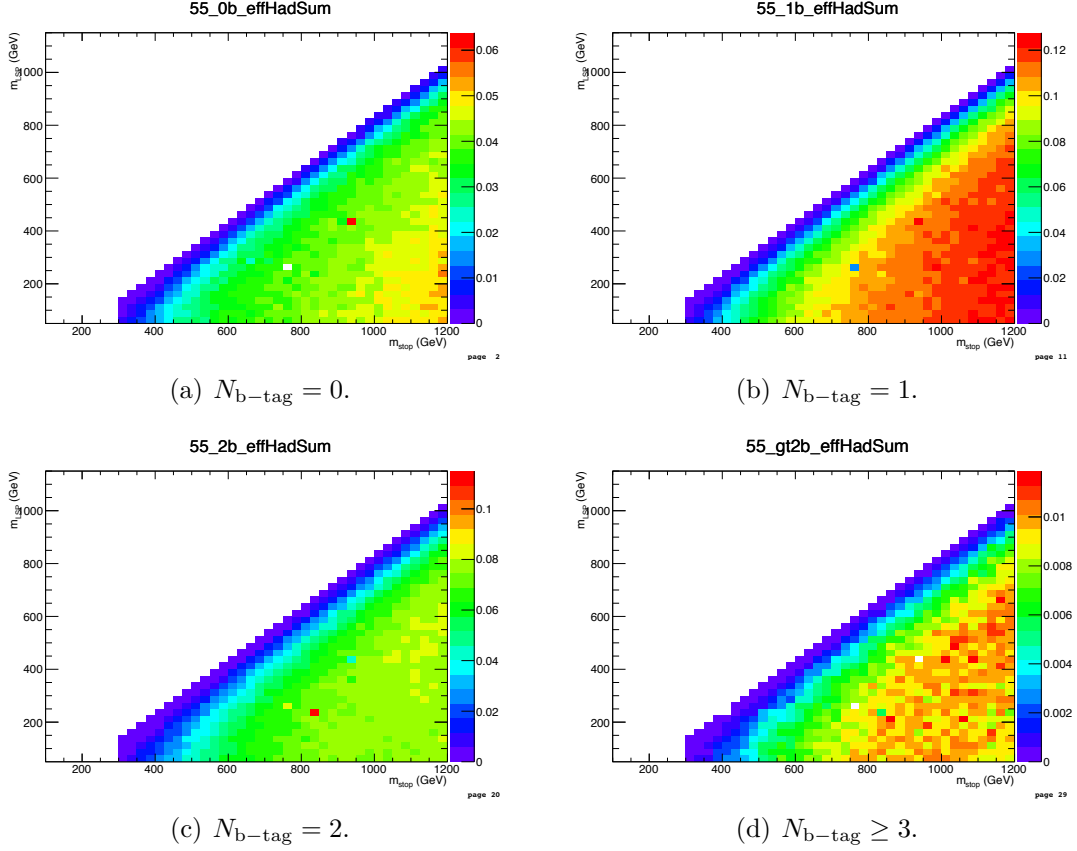


Figure E.4.: Signal efficiency in the (m_{sq}, m_{LSP}) plane of the T2tt simplified model, of the full hadronic signal selection, integrating over all eight H_T bins and requiring (a) exactly zero, (b) exactly one, (c) exactly two, and (d) at least three b-tags per event.

E.5. T2bb

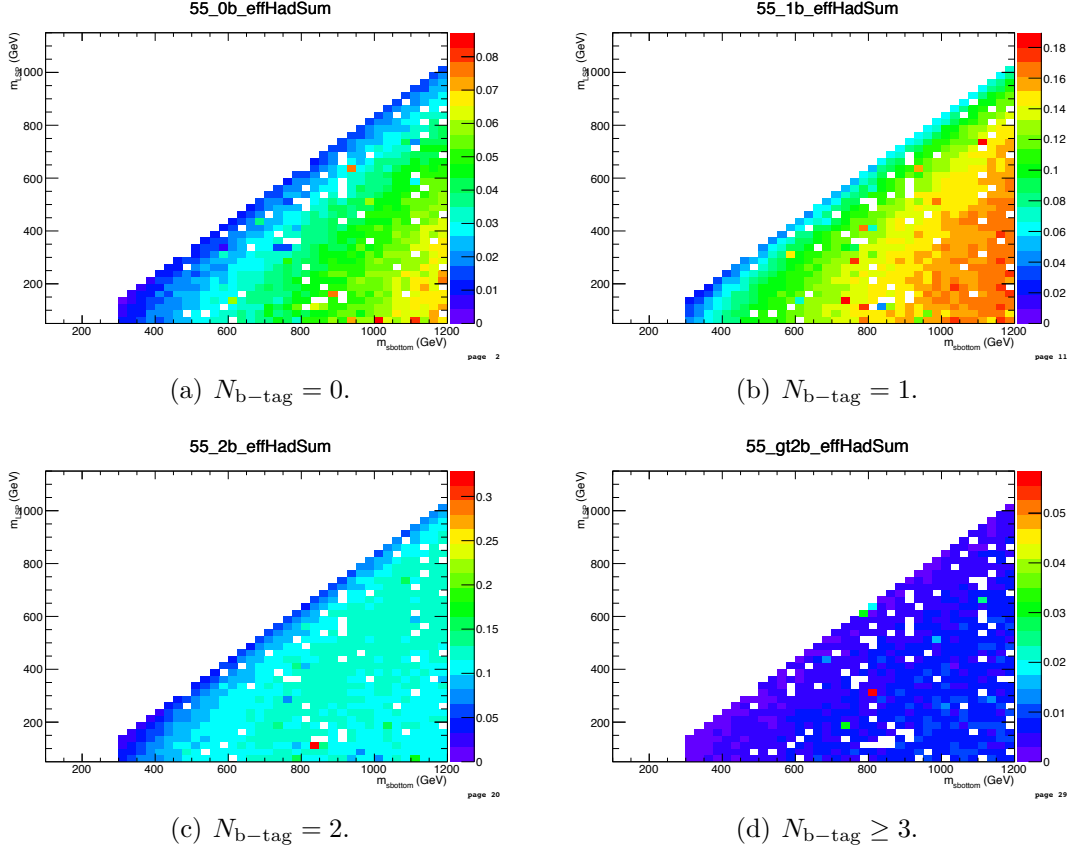


Figure E.5.: Signal efficiency in the (m_{sq}, m_{LSP}) plane of the T2bb simplified model, of the full hadronic signal selection, integrating over all eight H_T bins and requiring (a) exactly zero, (b) exactly one, (c) exactly two, and (d) at least three b-tags per event.

E.6. T1tttt

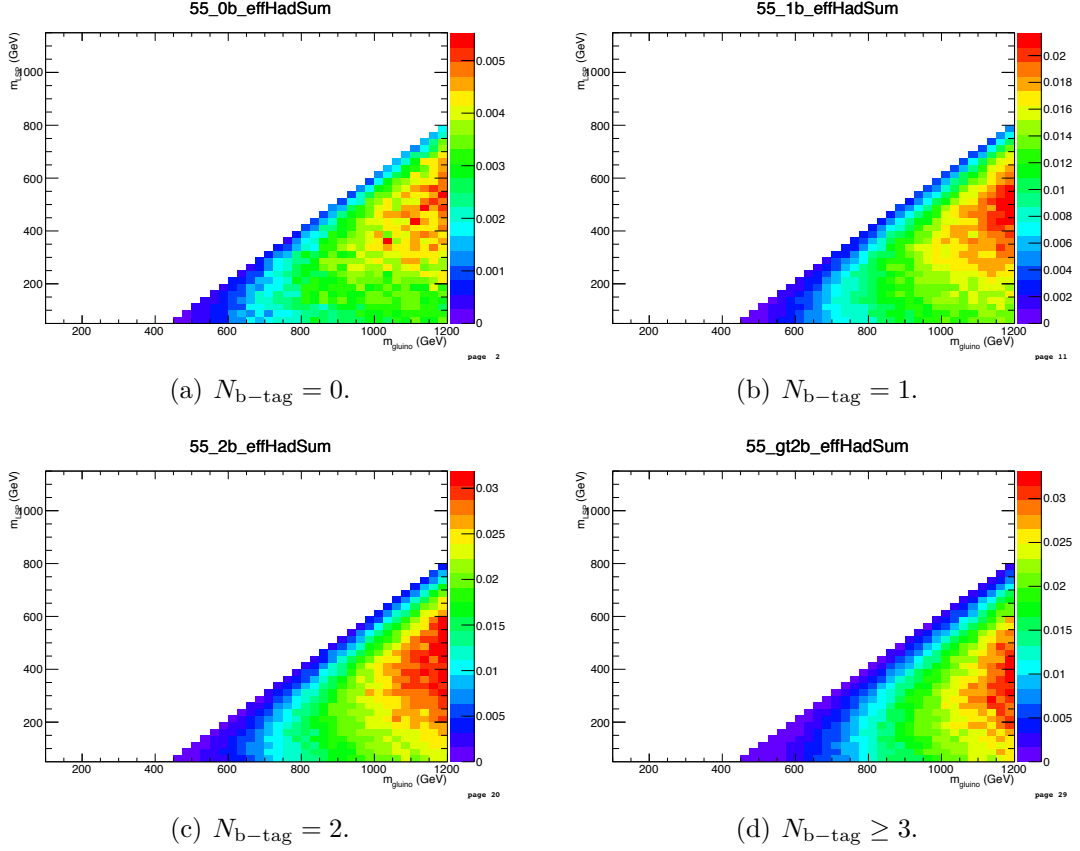


Figure E.6.: Signal efficiency in the $(m_{\text{glino}}, m_{\text{LSP}})$ plane of the T1tttt simplified model, of the full hadronic signal selection, integrating over all eight H_T bins and requiring (a) exactly zero, (b) exactly one, (c) exactly two, and (d) at least three b-tags per event.

E.7. T1bbbb

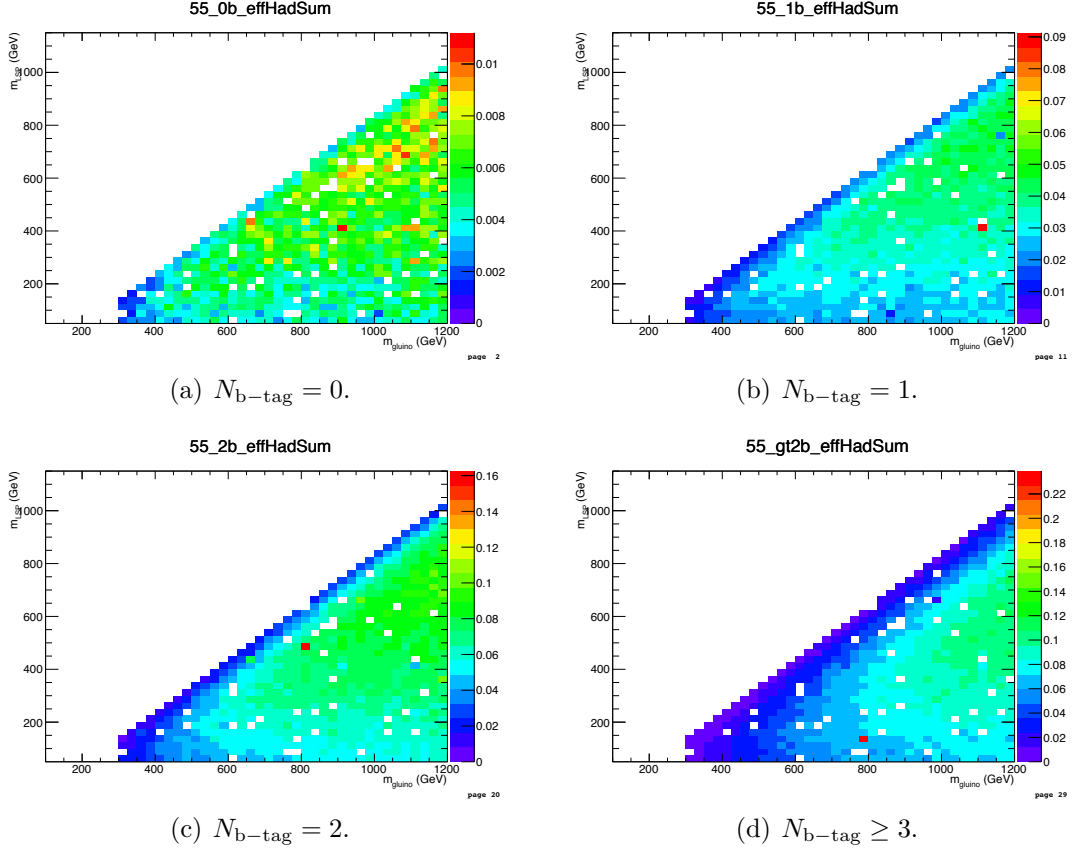


Figure E.7.: Signal efficiency in the $(m_{\text{glino}}, m_{\text{LSP}})$ plane of the T1bbbb simplified model, of the full hadronic signal selection, integrating over all eight H_T bins and requiring (a) exactly zero, (b) exactly one, (c) exactly two, and (d) at least three b-tags per event.

E.8. Signal contamination for T1tttt

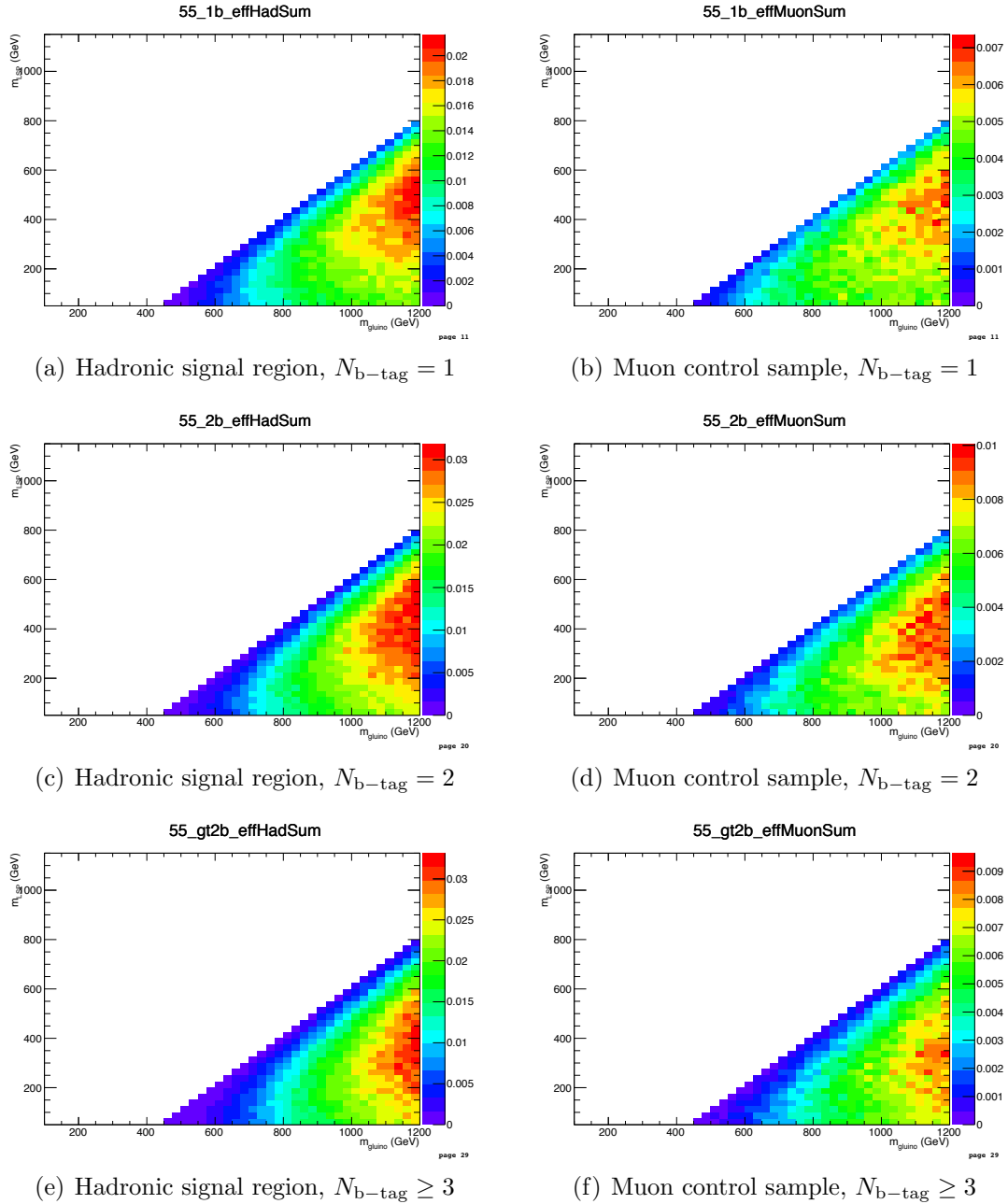


Figure E.8.: Signal efficiency in the planes of simplified model T1tttt, of the (left) hadronic signal sample selection or (right) single muon control sample selection, integrating over all eight H_T bins and requiring (top) exactly one, (middle) exactly two, or (bottom) at least three b-tags per event.

Appendix F.

Experimental uncertainties on signal efficiency times acceptance

F.1. Systematics due to jet energy scale uncertainties

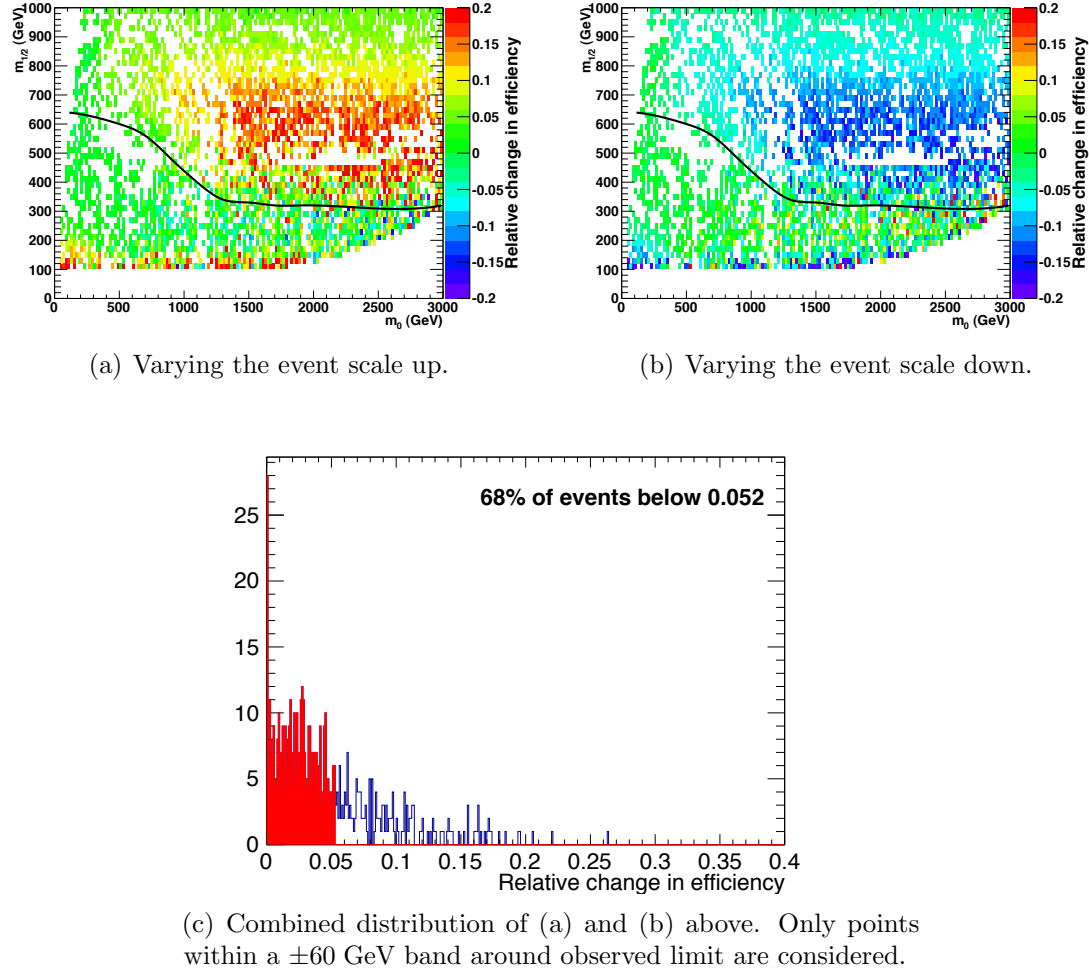


Figure F.1.: The effect of jet energy scale variations on signal efficiency in the CMSSM plane. All plots show the relative change in efficiency. No requirement is made on the number of reconstructed b jets. The red shaded area is bounded by the 68th percentile.

F.2. Systematics due to the MHT/MET cut

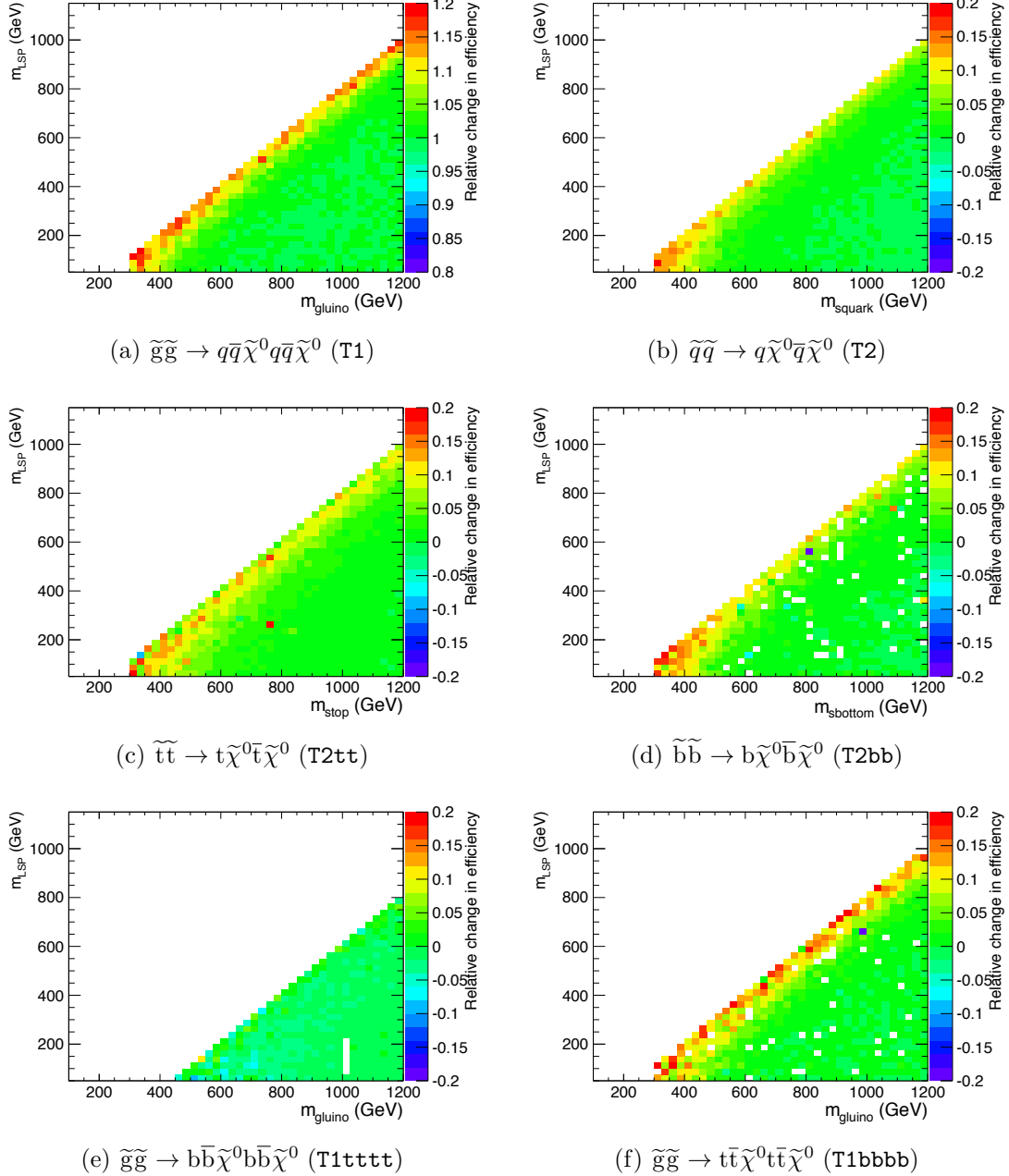


Figure F.2.: The fractional change in signal efficiency due to systematically increasing all jet energies, for various topologies. No requirement is made on the number of reconstructed b jets.

F.3. Systematics due to the dead ECAL cut

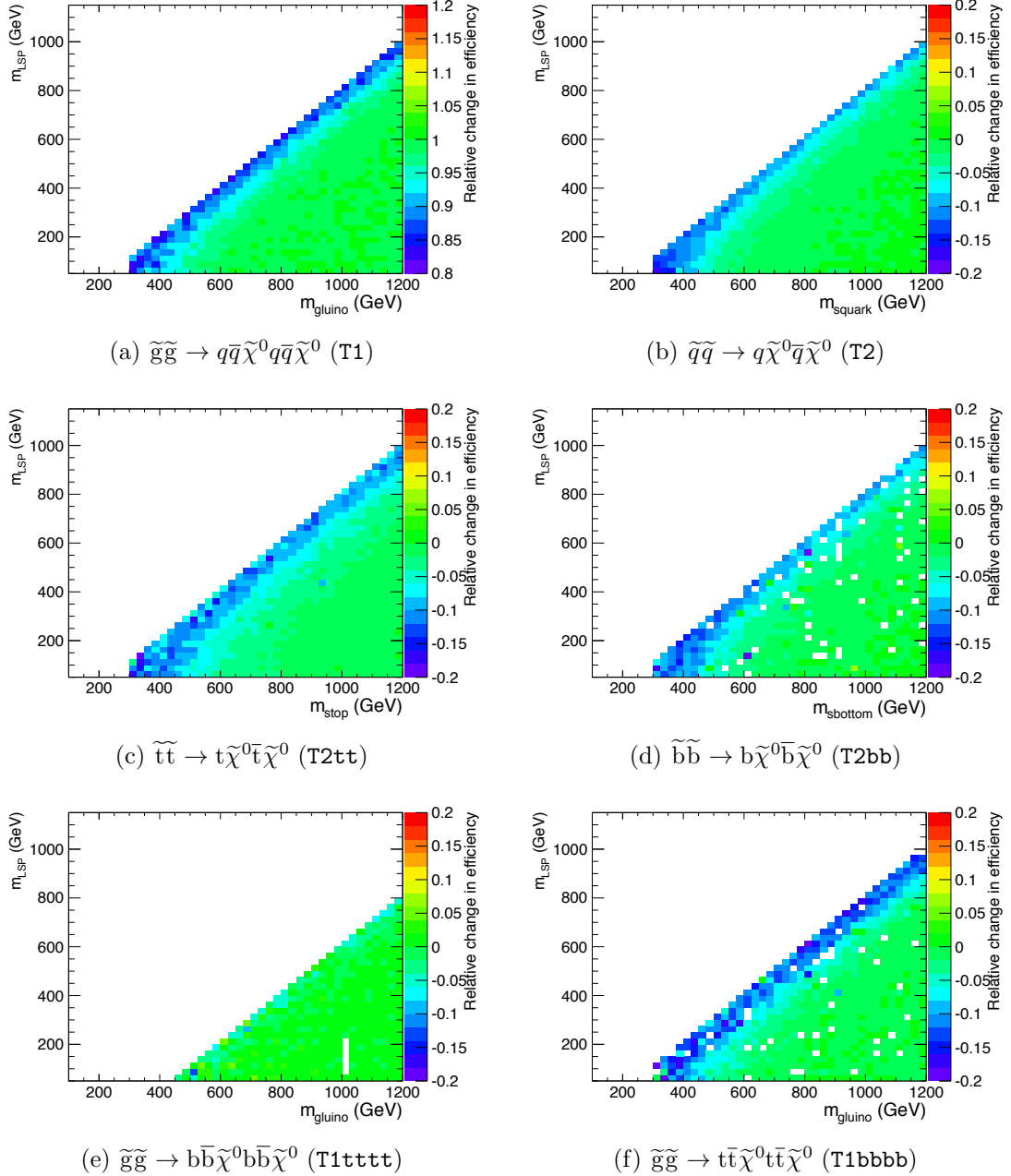


Figure F.3.: The fractional change in signal efficiency due to systematically decreasing all jet energies, for various topologies. No requirement is made on the number of reconstructed b jets.

F.4. Systematics due to the lepton and photon vetoes

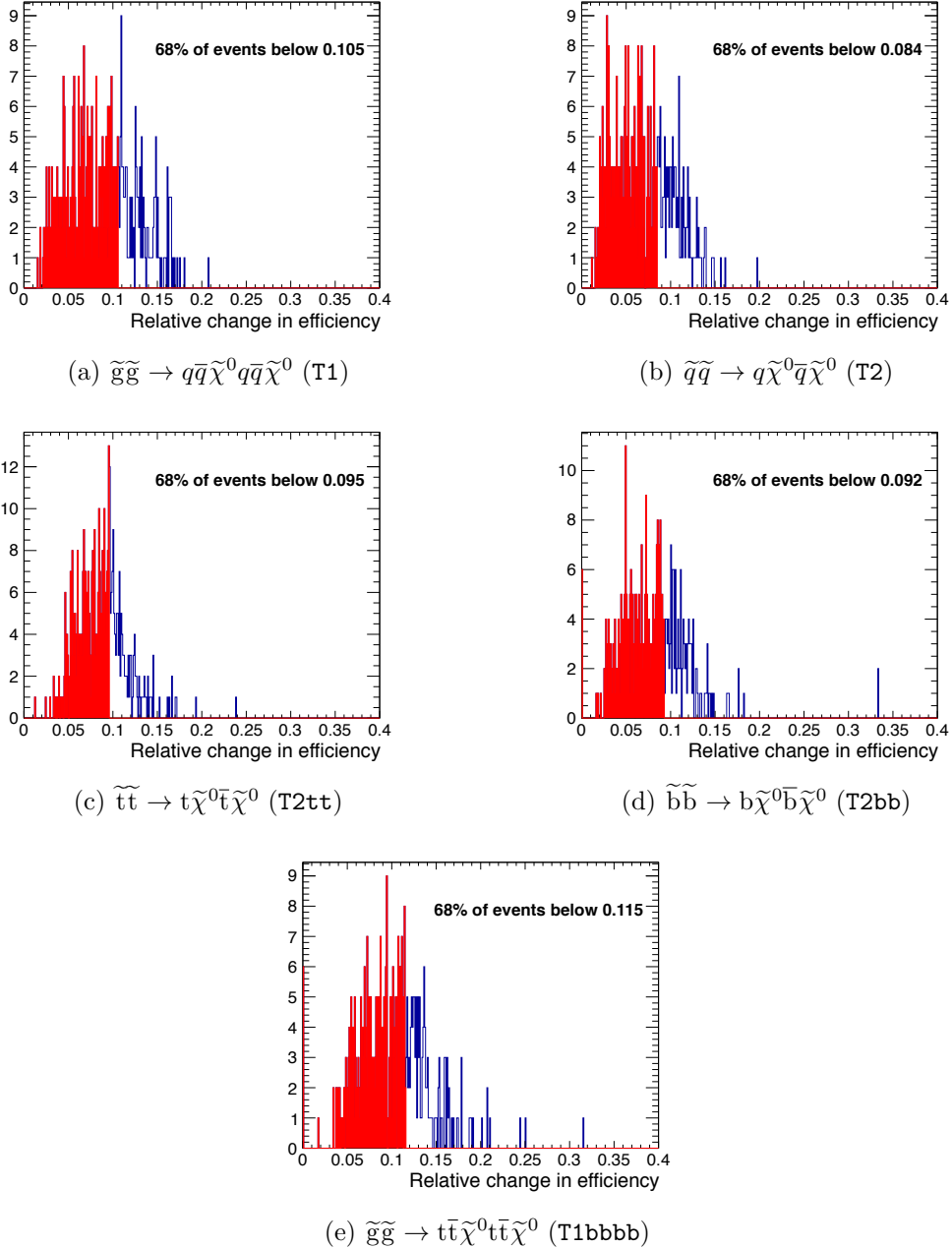


Figure F.4.: The fractional change in signal efficiency near to the diagonal due to systematically increasing or decreasing all jet energies, for various topologies. No requirement is made on the number of reconstructed b jets.

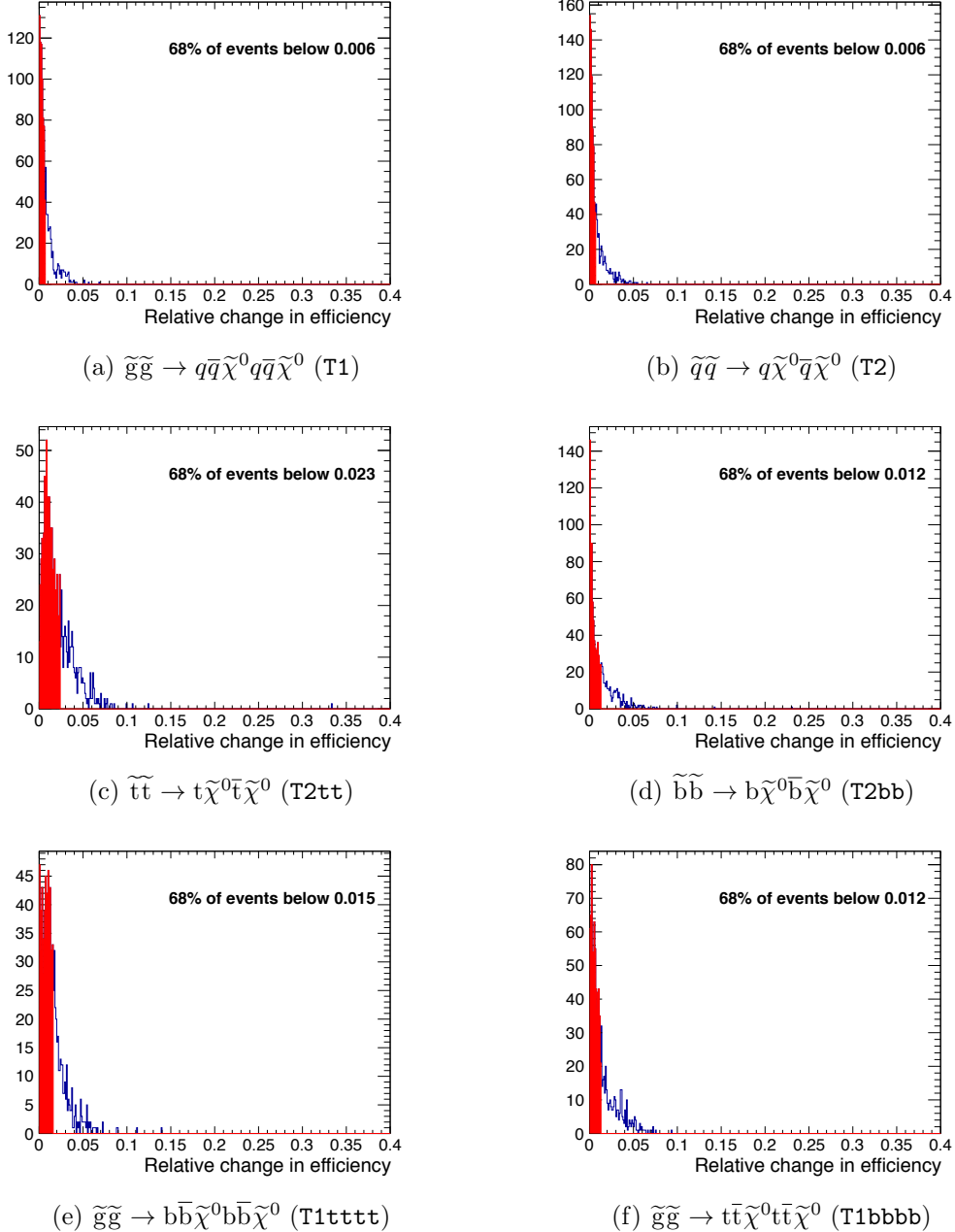


Figure F.5.: The fractional change in signal efficiency far from the diagonal due to systematically increasing or decreasing all jet energies, for various topologies. No requirement is made on the number of reconstructed b jets.

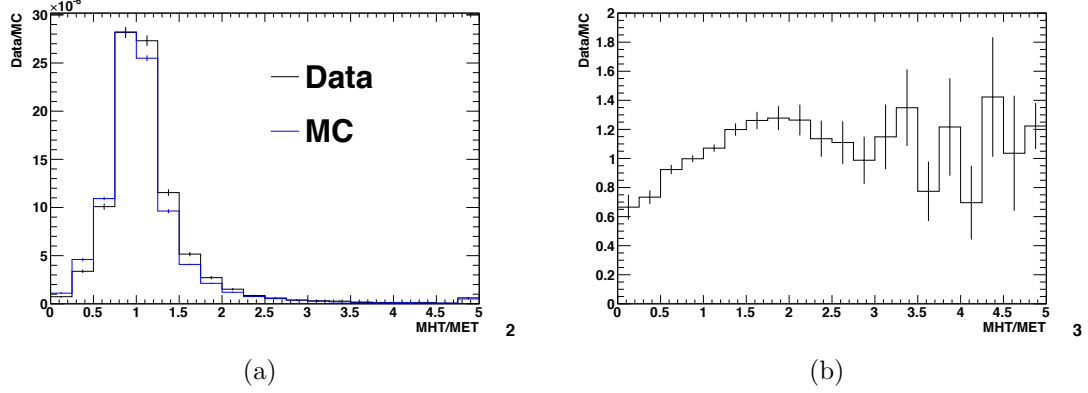
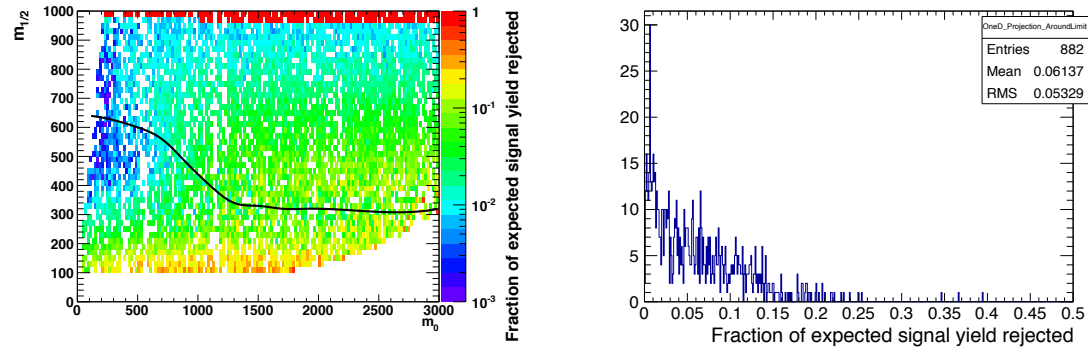


Figure F.6.: (a) Comparison of the MHT/MET distributions from data and MC, and (b) the ratio of the distributions, data/MC, as a function of the MHT/MET cut value.



(a) Fraction of expected signal yield rejected. (b) Fraction of expected signal yield rejected in a ± 60 GeV band around the observed limit.

Figure F.7.: The fraction of expected signal yield that is rejected by the MHT/MET cut in the CMSSM plane. No requirement is made on the number of reconstructed b jets.

Table F.1.: Conservative estimates of inefficiency (%) for the MHT/MET cut when considering model points in the region near to the diagonal (i.e. small mass splitting and compressed spectra) for various simplified models.

	T1	T2	T2tt	T2bb	T1tttt	T1bbbb
Near	10.9	3.5	20.4	3.9	-	10.8
Far	3.2	0.9	3.1	1.2	32.4	3.7

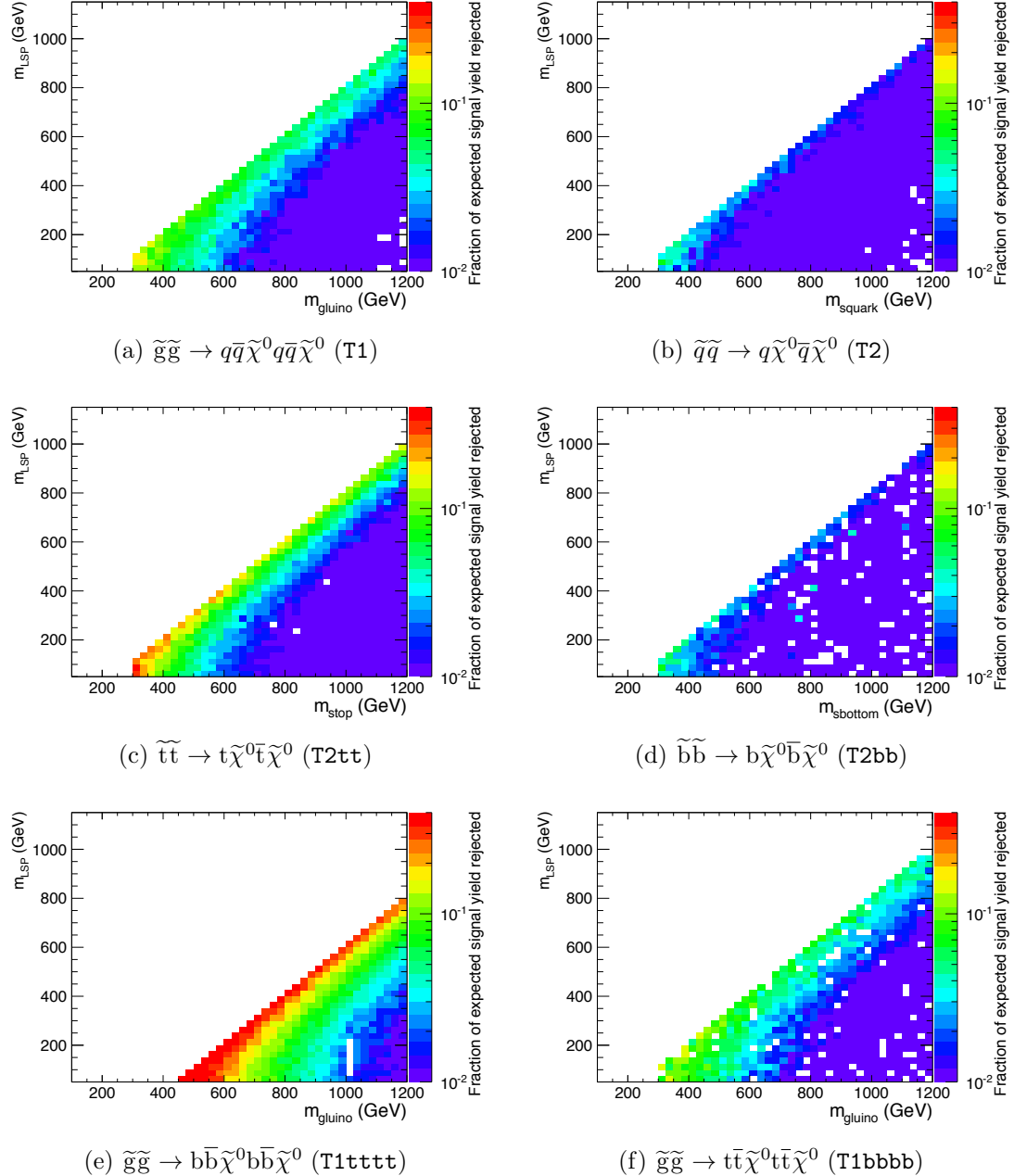


Figure F.8.: The fraction of expected signal yield that is rejected by the MHT/MET cleaning cut, for various topologies. No requirement is made on the number of reconstructed b jets.

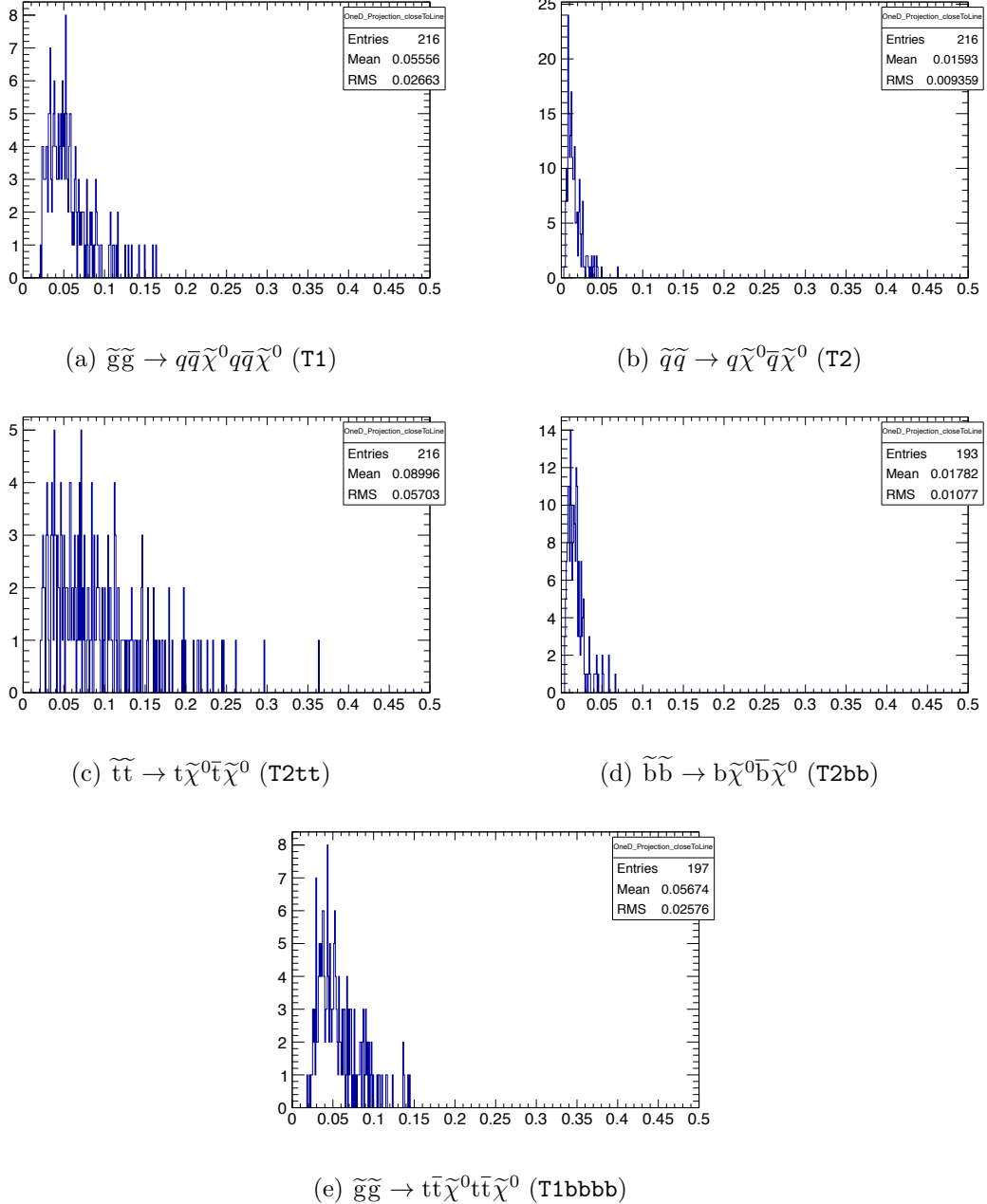


Figure F.9.: The fraction of expected signal yield that is rejected by the MHT/MET cleaning cut, near to the diagonal, for various topologies. No requirement is made on the number of reconstructed b jets.

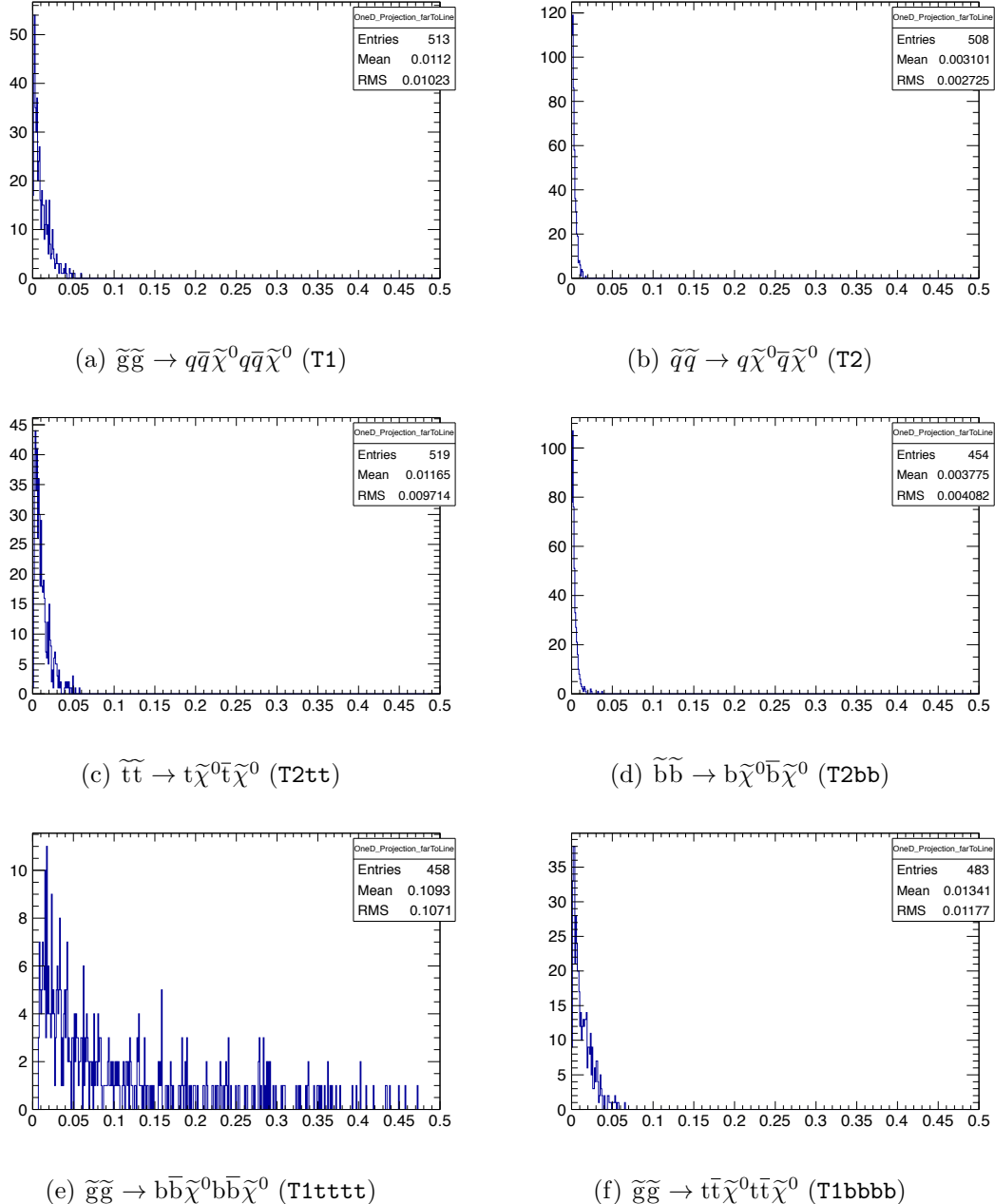
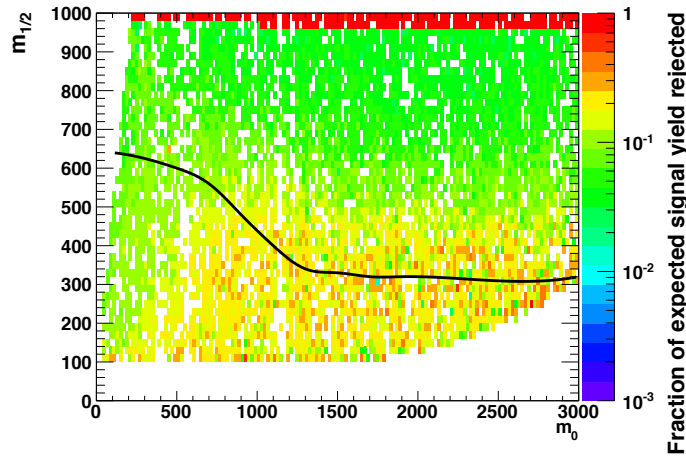


Figure F.10.: The fraction of expected signal yield that is rejected by the MHT/MET cleaning cut, far from the diagonal, for various topologies. No requirement is made on the number of reconstructed b jets.



(a) Fraction of expected signal yield rejected.

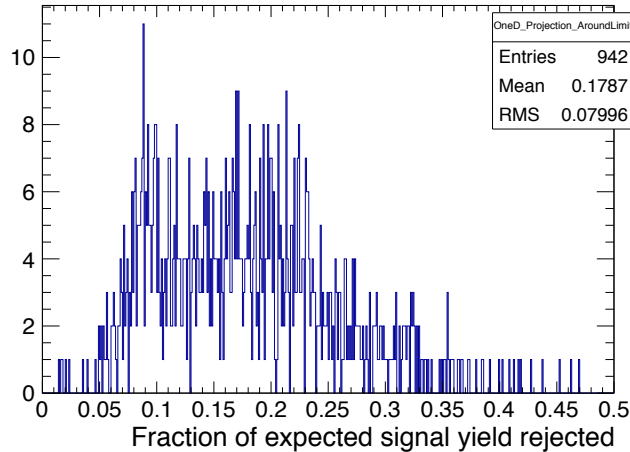
(b) Fraction of expected signal yield rejected in a ± 60 GeV band around the observed limit.

Figure F.11.: The fraction of expected signal yield that is rejected by the dead ECAL cut in the CMSSM plane. No requirement is made on the number of reconstructed b jets.

Table F.2.: Conservative estimates of inefficiency (%) for the dead ECAL cut when considering model points in the region near to the diagonal (i.e. small mass splitting and compressed spectra) for various simplified models.

	T1	T2	T2tt	T2bb	T1tttt	T1bbbb
Near	13.3	6.4	23.7	7.5	-	16.4
Far	13.6	5.8	9.4	6.2	27.6	13.9

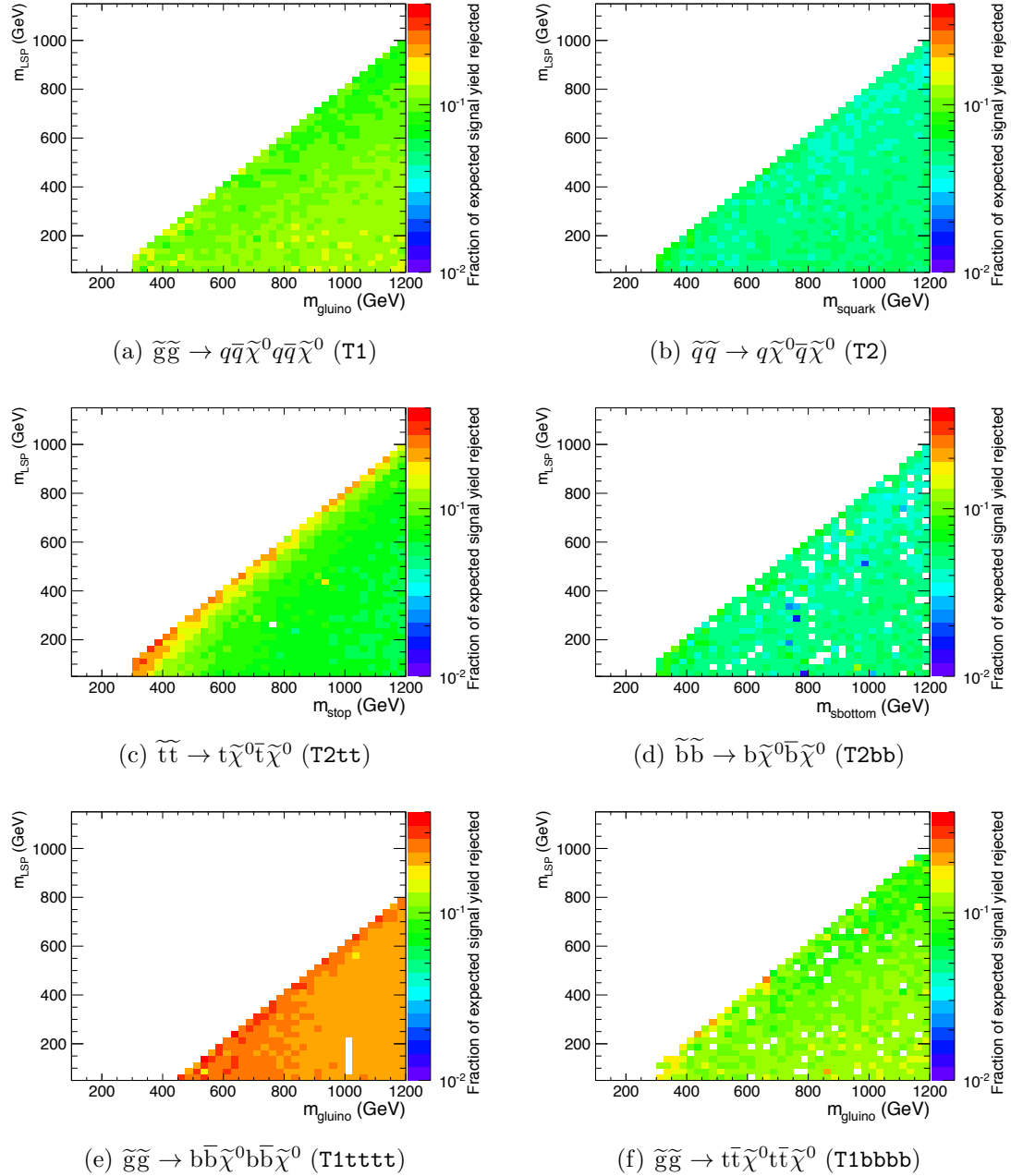


Figure F.12.: The fraction of expected signal yield that is rejected by the dead ECAL cleaning cut, for various topologies. No requirement is made on the number of reconstructed b jets.

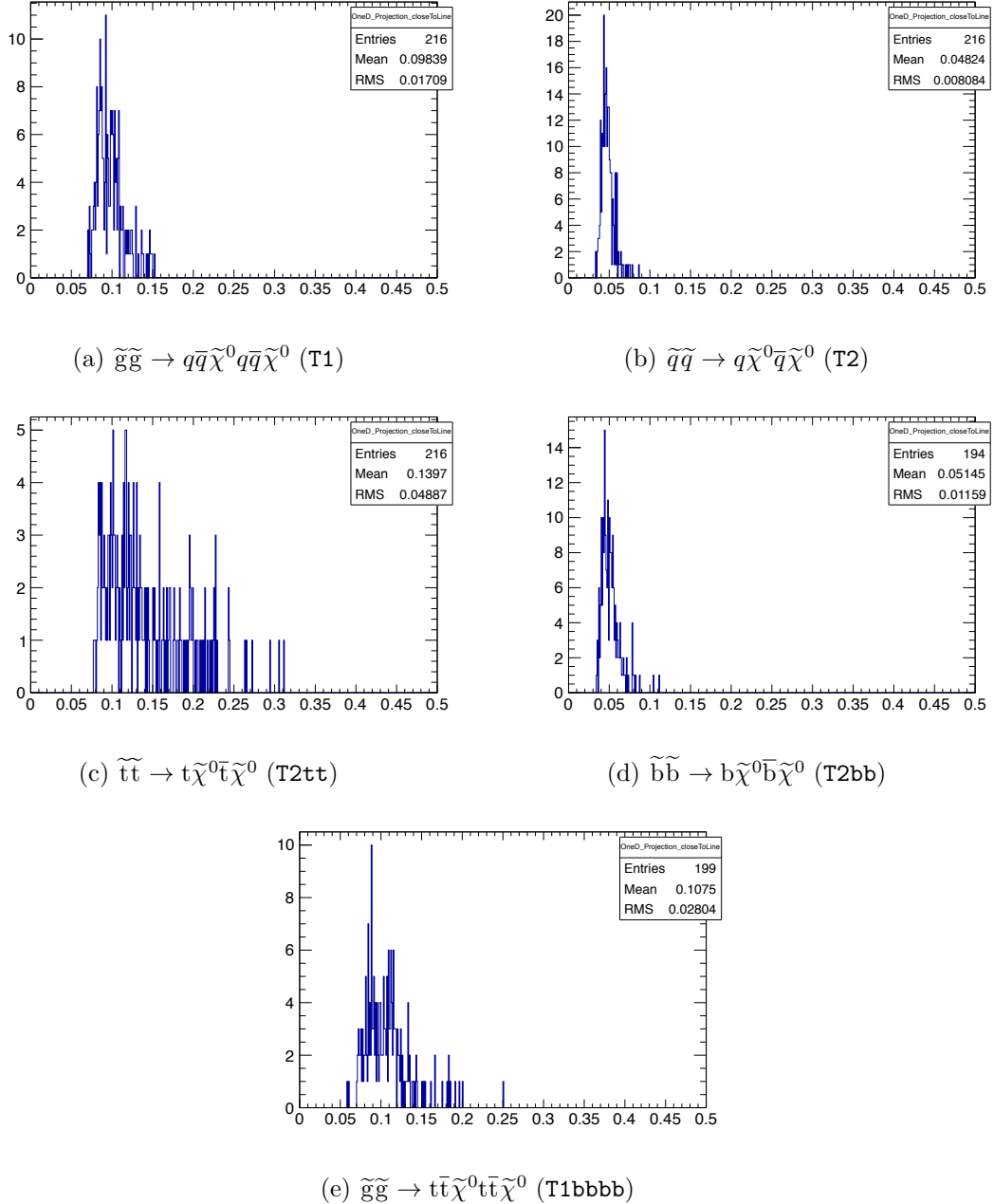


Figure F.13.: The fraction of expected signal yield that is rejected by the dead ECAL cleaning cut, near to the diagonal, for various topologies. No requirement is made on the number of reconstructed b jets.

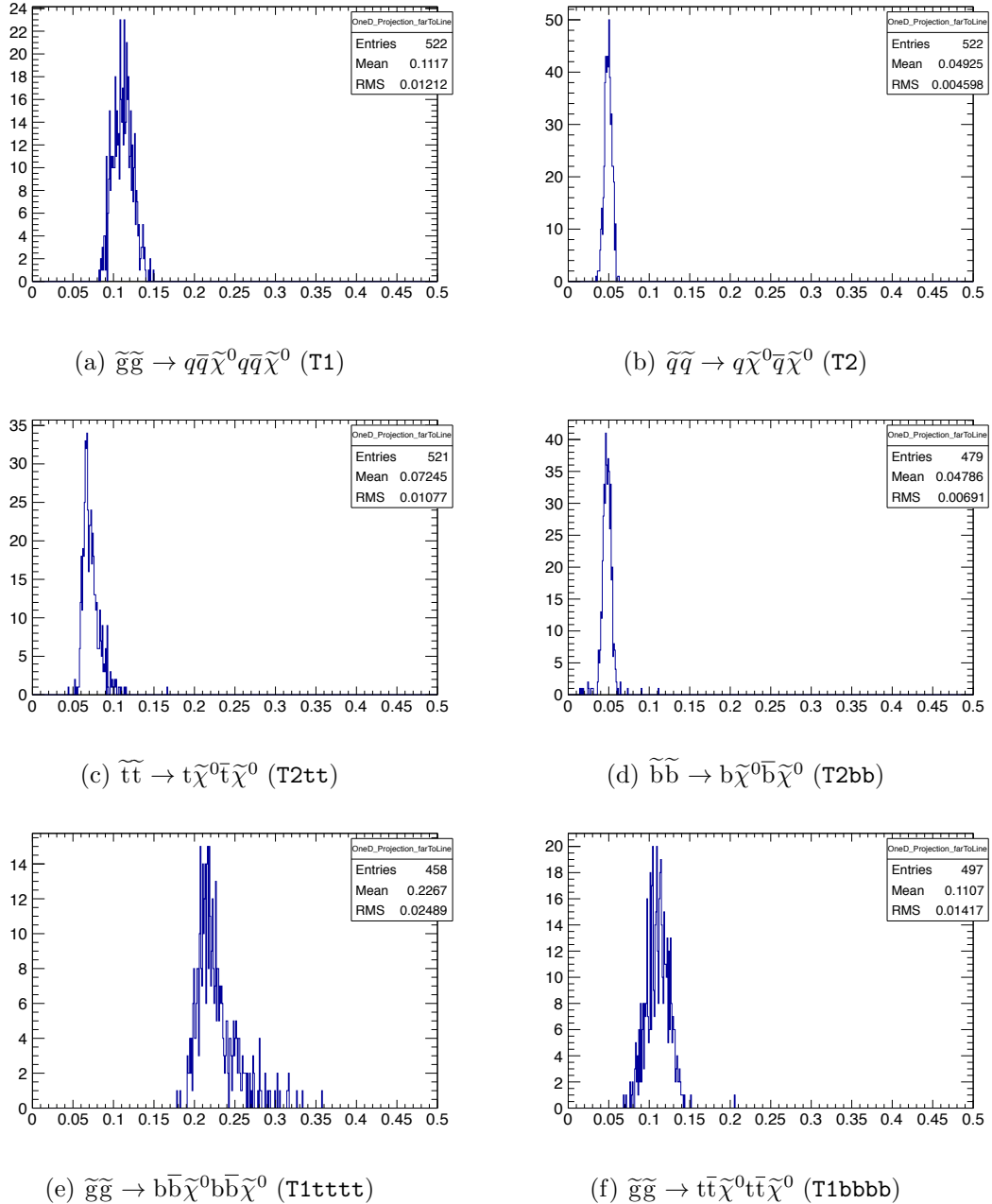
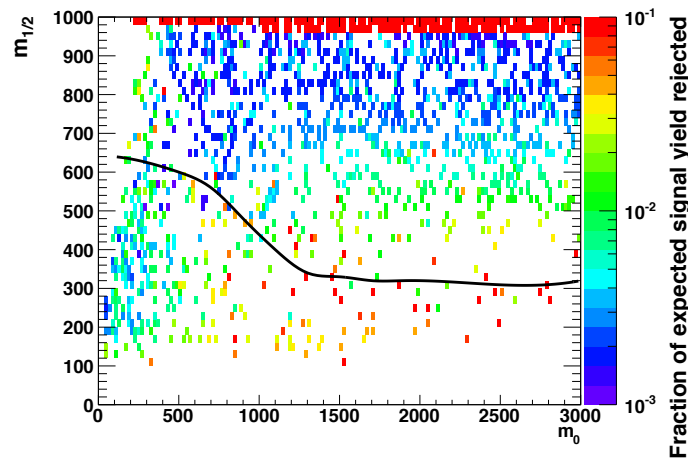


Figure F.14.: The fraction of expected signal yield that is rejected by the dead ECAL cleaning cut, far from the diagonal, for various topologies. No requirement is made on the number of reconstructed b jets.



(a) Fraction of expected signal yield rejected.

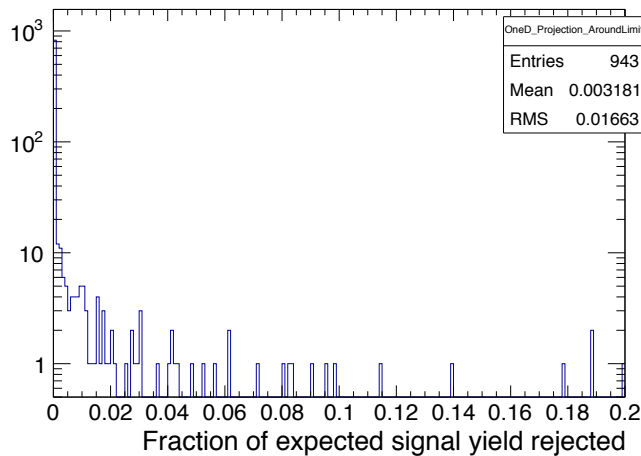
(b) Fraction of expected signal yield rejected in a ± 60 GeV band around the observed limit.

Figure F.15.: The fraction of expected signal yield that is rejected by the dead ECAL cut in the CMSSM plane. No requirement is made on the number of reconstructed b jets.

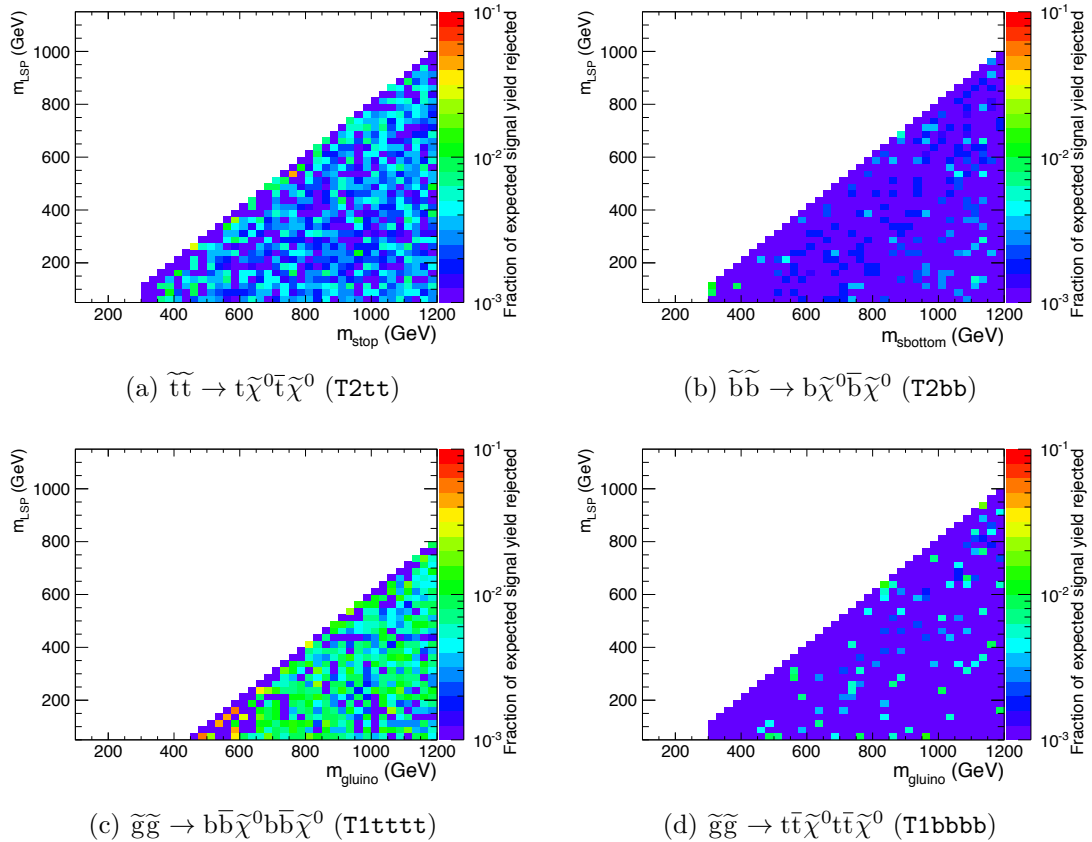


Figure F.16.: The fraction of expected signal yield that is rejected by the lepton and photon vetoes, for various topologies. No requirement is made on the number of reconstructed b jets.

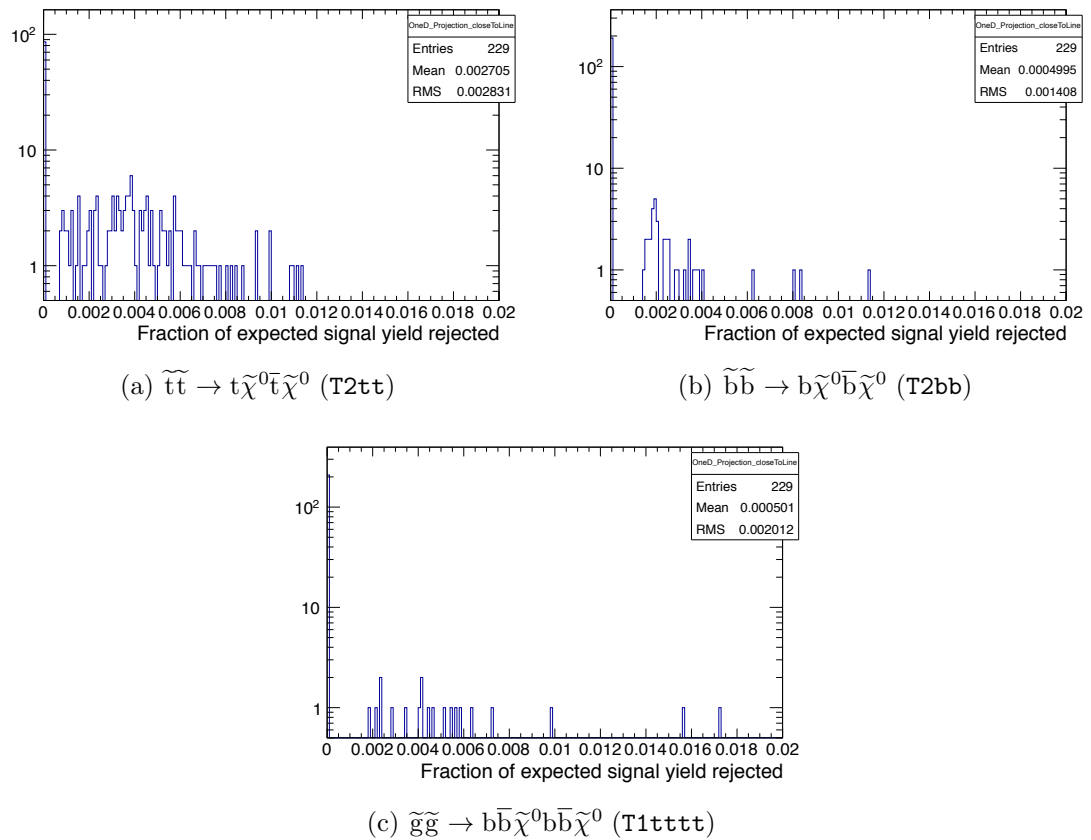


Figure F.17.: The fraction of expected signal yield that is rejected by the lepton and photon vetoes, near to the diagonal, for various topologies. No requirement is made on the number of reconstructed b jets.

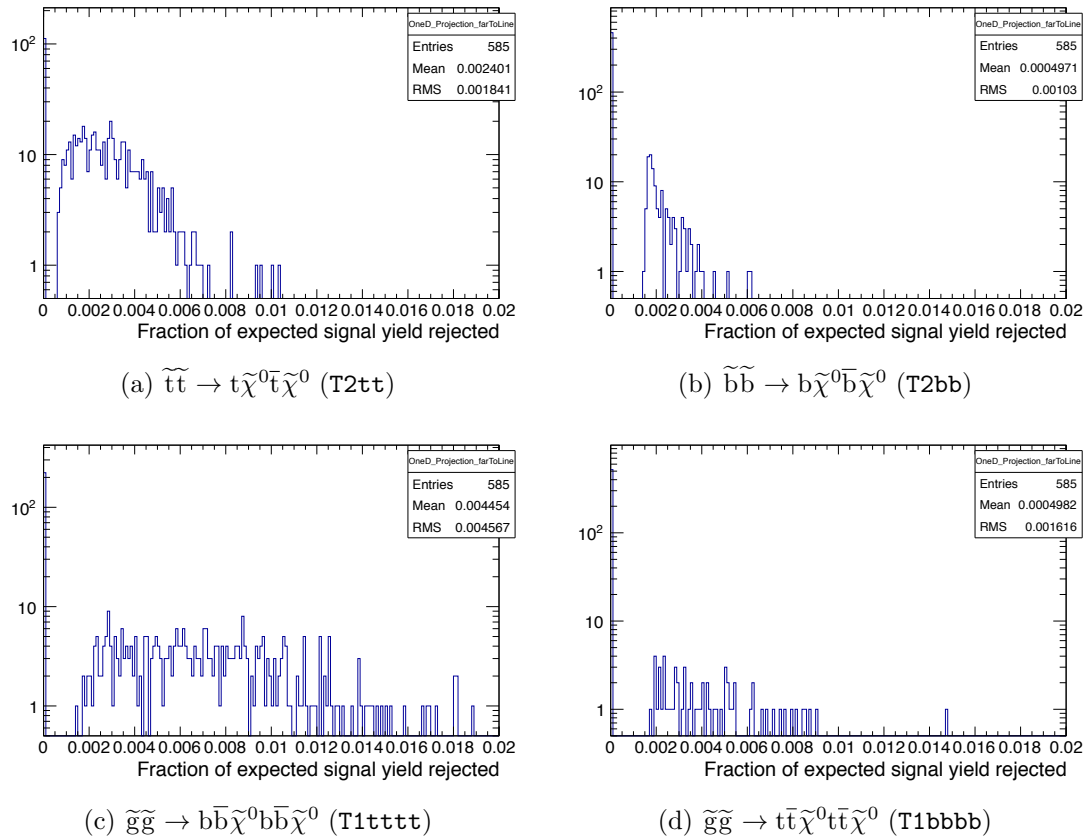


Figure F.18.: The fraction of expected signal yield that is rejected by the lepton and photon vetoes, far from the diagonal, for various topologies. No requirement is made on the number of reconstructed b jets.

Bibliography

- [1] E. Corbelli and P. Salucci, “The extended rotation curve and the dark matter halo of m33,” 1999.
- [2] M. Jeitler, “Trigger systems at LHC experiments,” *Nuclear Instruments and Methods in Physics Research Section A: Accelerators, Spectrometers, Detectors and Associated Equipment*, vol. 598, no. 1, pp. 305 – 311, 2009.
- [3] The ATLAS Collaboration, “The ATLAS Experiment at the CERN Large Hadron Collider,” *JINST 3 S08003*, 2008.
- [4] The CMS Collaboration, “The CMS experiment at the CERN LHC,” *JINST 3 S08004*, 2008.
- [5] The LHCb Collaboration, “The LHCb experiment at the CERN LHC,” *JINST 3 S08005*, 2008.
- [6] The ALICE Collaboration, “The ALICE experiment at the CERN LHC,” *JINST 3 S08002*, 2008.
- [7] J. Beringer et al., “Review of particle physics,” *Phys. Rev. D*, vol. 86, p. 010001, 2012.
- [8] The CMS Collaboration, “Observation of a new boson at a mass of 125 GeV with the CMS experiment at the LHC,” *Physics Letters B*, vol. 716, no. 1, pp. 30 – 61, 2012.
- [9] S. L. mo, “Partial-symmetries of weak interactions,” *Nuclear Physics*, vol. 22, no. 4, pp. 579 – 588, 1961.
- [10] S. Weinberg, “A model of leptons,” *Phys. Rev. Lett.*, vol. 19, pp. 1264–1266, 1967.
- [11] G. ’t Hooft and M. Veltman, “Regularization and renormalization of gauge fields,” *Nuclear Physics B*, vol. 44, no. 1, pp. 189 – 213, 1972.

- [12] A. Salam, “Weak and Electromagnetic Interactions,” *Conf. Proc.*, vol. C680519, pp. 367–377, 1968.
- [13] F. Englert and R. Brout, “Broken symmetry and the mass of gauge vector mesons,” *Phys. Rev. Lett.*, vol. 13, pp. 321–323, 1964.
- [14] P. Higgs, “Broken symmetries, massless particles and gauge fields,” *Physics Letters*, vol. 12, no. 2, pp. 132 – 133, 1964.
- [15] P. Higgs, “Broken symmetries and the masses of gauge bosons,” *Phys. Rev. Lett.*, vol. 13, pp. 508–509, 1964.
- [16] G. S. Guralnik, C. R. Hagen, and T. W. B. Kibble, “Global conservation laws and massless particles,” *Phys. Rev. Lett.*, vol. 13, pp. 585–587, 1964.
- [17] P. Higgs, “Spontaneous symmetry breakdown without massless bosons,” *Phys. Rev.*, vol. 145, pp. 1156–1163, 1966.
- [18] T. W. B. Kibble, “Symmetry breaking in non-abelian gauge theories,” *Phys. Rev.*, vol. 155, pp. 1554–1561, 1967.
- [19] “<http://en.wikipedia.org/wiki/image:interactions.png>,” 2008.
- [20] D. Griffiths, *Introduction to elementary particles*. Wiley-VCH, 2008.
- [21] G. Hooft, “Renormalizable lagrangians for massive yang-mills fields,” *Nuclear Physics B*, vol. 35, no. 1, pp. 167 – 188, 1971.
- [22] UA1 Collaboration, “Experimental observation of isolated large transverse energy electrons with associated missing energy at $\sqrt{s} = 540\text{gev}$,” *Physics Letters B*, vol. 122, no. 1, pp. 103 – 116, 1983.
- [23] The Delphi Collaboration, “Measurement of the mass and width of the $z0$ particle from multihadronic final states produced in $e + e-$ annihilations,” *Physics Letters B*, vol. 231, no. 4, pp. 539 – 547, 1989.
- [24] P. Higgs, “Spontaneous Symmetry Breakdown without Massless Bosons,” *Physical Review*, vol. 145, no. 4, pp. 1156–1163, 1966.
- [25] P. Higgs, “Broken Symmetres and the Masses of Gauge Bosons,” *Physical Review Letters*, vol. 13, no. 16, pp. 508–509, 1964.
- [26] The ATLAS Collaboration, “Observation of a new particle in the search for the

- Standard Model Higgs boson with the ATLAS detector at the LHC,” *Physics Letters B*, vol. 716, no. 1, pp. 1 – 29, 2012.
- [27] S. P. Martin, “A Supersymmetry Primer,” *arXiv*, vol. hep-ph, Sept. 1997.
 - [28] Y. A. Golfand and E. P. Likhtman, “Extension of the Algebra of Poincaré Group Generators and Violation of p Invariance,” *JETP Lett.*, vol. 13, p. 323, 1971.
 - [29] J. Wess and B. Zumino, “Supergauge transformations in four dimensions,” *Nucl. Phys. B*, vol. 70, p. 39, 1974.
 - [30] H. P. Nilles, “Supersymmetry, Supergravity and Particle Physics,” *Phys. Reports*, vol. 110, p. 1, 1984.
 - [31] H. Haber and G. Kane, “The Search for Supersymmetry: Probing Physics Beyond the Standard Model,” *Phys. Reports*, vol. 117, p. 75, 1987.
 - [32] R. Barbieri, S. Ferrara, and C. A. Savoy, “Gauge Models with Spontaneously Broken Local Supersymmetry,” *Phys. Lett. B*, vol. 119, p. 343, 1982.
 - [33] S. Dawson, E. Eichten, and C. Quigg, “Search for Supersymmetric Particles in Hadron - Hadron Collisions,” *Phys. Rev. D*, vol. 31, p. 1581, 1985.
 - [34] E. Witten, “Dynamical Breaking of Supersymmetry,” *Nucl. Phys. B*, vol. 188, p. 513, 1981.
 - [35] S. Dimopoulos and H. Georgi, “Softly Broken Supersymmetry and SU(5),” *Nucl. Phys. B*, vol. 193, p. 150, 1981.
 - [36] S. Coleman and J. Mandula, “All possible symmetries of the s matrix,” *Phys. Rev.*, vol. 159, pp. 1251–1256, 1967.
 - [37] G.L.Kane et al., “Study of constrained minimal supersymmetry,” *Phys. Rev. D*, vol. 49, p. 6173, 1994.
 - [38] O. Buchmueller, R. Cavanaugh, D. Colling, A. de Roeck, M. J. Dolan, J. R. Ellis, H. Flacher, S. Heinemeyer, G. Isidori, K. Olive, S. Rogerson, F. Ronga, and G. Weiglein, “Implications of Initial LHC Searches for Supersymmetry,” *arXiv*, vol. hep-ph, 2011.
 - [39] N. Arkani-Hamed, P. Schuster, N. Toro, J. Thaler, and L.-T. e. a. Wang, “MAR-MOSET: The Path from LHC Data to the New Standard Model via On-Shell Effective Theories,” 2007.

- [40] Martin, A.D. and Stirling, W.J. and Thorne, R.S. and Watt, G., “Parton distributions for the LHC,” *Eur.Phys.J.*, vol. C63, pp. 189–285, 2009.
- [41] T. Sakuma, “3d sketchup images of the cms detector (120918),” 2012.
- [42] The CMS Collaboration, “CMS Tracking Performance Results from Early LHC Operation,” *Eur. Phys. J. C*, vol. 70, no. arXiv:1007.1988. CERN-PH-EP-2010-019. CMS-TRK-10-001, p. 1165. 29 p, 2010.
- [43] *The CMS electromagnetic calorimeter project: Technical Design Report*. Technical Design Report CMS, Geneva: CERN, 1997.
- [44] W. Smith, P. Busson, S. Dasu, J. Hauser, G. Heath, J. Krolikowski, J. Varela, A. Taurok, G. Wrochna, and P. Zotto, “CMS Phyiscs Technical Design Report: The Trigger System,” vol. 1, pp. 1–630, 2000.
- [45] The CMS Collaboration, “Ecal performance plots, 2012 data, cms-dp-2012-015,” 2012.
- [46] The CMS Collaboration, “Ecal performance on 2011 data, cms-dp-2012-002,” 2012.
- [47] The CMS Collaboration, “Hcal performance from first collisions data, cms-dp-2010-025,” 2010.
- [48] The CMS collaboration, “Performance of cms muon reconstruction in pp collision events at $s = 7$ tev,” *Journal of Instrumentation*, vol. 7, no. 10, p. P10002, 2012.
- [49] The CMS Collaboration, “The Trigger and Data Acquisition Project Technical Design Report, Volume 1, The Level-1 Trigger,” *CERN/LHCC 2000-038, CMS TDR 6.1*, 2000.
- [50] J. Marrouche et al., “Commissioning the CMS Global Calorimeter Trigger,” *CMS IN*, vol. 2010/029, 2010.
- [51] G.Iles et al., “Revised CMS Global Calorimeter Trigger Functionality and Algorithms,” *Proceedings of the 12th Workshop on Electronics for LHC and Future Experimentsm 25-29 September 2006, Valencia, Spain*.
- [52] The CMS Collaboration, “Jet energy corrections determination at 7 tev,” CMS Physics Analysis Summary JME-10-010, 2010.
- [53] G. P. S. M. Cacciari and G. Soyez, “Fastjet user manual,” *Eur. Phys. J. C*, vol. 72, 2012.

- [54] J. Brooke, “Performance of the cms level-1 trigger,” *ICHEP 2012 Melbourne*, 2012.
- [55] The CMS Collaboration, “Calorimeter jet quality criteria for the first cms collision data and preparations for calibrating their efficiencies..”
- [56] The CMS Collaboration, “Search for supersymmetry in final states with missing transverse energy and 0, 1, 2, or at least 3 b-quark jets in 7 TeV pp collisions using the variable alphaT,” *JHEP*, vol. 1301, p. 077, 2013.
- [57] M. Cacciari, G. Salam, and G. Soyez, “The anti-kt jet clustering algorithm,” *Journal of High Energy Physics*, 2008.
- [58] The CMS Collaboration, “Determination of Jet Energy Calibration and Transverse Momentum Resolution in CMS,” *arXiv*, vol. 6, p. P11002, 2011.
- [59] The CMS Collaboration, “Determination of jet energy calibration and transverse momentum resolution in cms,” *Journal of Instrumentation*, vol. 6, no. 11, p. P11002, 2011.
- [60] M. Cacciari and G. P. Salam, “Dispelling the n^3 myth for the k_t jet-finder,” *Phys Letters B*.
- [61] The CMS Collaboration, “Cms physics technical design report, volume ii: Physics performance,” *Journal of Physics G: Nuclear and Particle Physics*, vol. 34, no. 6, p. 995, 2007.
- [62] W. Adam, R. Frhwirth, A. Strandlie, and T. Todorov, “Reconstruction of electrons with the Gaussian-sum filter in the CMS tracker at the LHC,” *Journal of Physics G: Nuclear and Particle Physics*, vol. 31, no. 9, p. N9, 2005.
- [63] The CMS Collaboration, “Electron reconstruction and identification at $\sqrt{s} = 7$ TeV,” tech. rep., 2010.
- [64] The CMS Collaboration, “Performance of muon identification in pp collisions at $\sqrt{s} = 7$ TeV,” tech. rep., 2010.
- [65] The CMS Collaboration, “Isolated Photon Reconstruction and Identification at $\sqrt{s} = 7$ TeV,” tech. rep., 2010.
- [66] L. Randall and D. Tucker-Smith, “Dijet Searches for Supersymmetry at the LHC,” *Phys.Rev.Lett.*, vol. 101, p. 221803, 2008.
- [67] The CMS Collaboration, “SUSY searches with dijet events, CMS-PAS-SUS-08005,”

- tech. rep., 2008.
- [68] The CMS Collaboration, “Search strategy for exclusive multi-jet events from supersymmetry at CMS,” CMS-PAS-SUS-09001, tech. rep., 2009.
- [69] “Search for supersymmetry in final states with missing transverse energy and 0, 1, 2, 3, or at least 4 b-quark jets in 8 tev pp collisions using the variable alphat,” no. CMS-PAS-SUS-12-028, 2012.
- [70] The CMS Collaboration, “CMS b-tagging performance database, Internal Reference,” tech. rep.
- [71] The CMS Collaboration, “CMS PAS BTV 09 001 Algorithms for b-Jet identification in CMS.”
- [72] “Search for supersymmetry with the α_t variable in the 7 tev dataset of 2011,” no. CMS-AN-11-517, 2011.
- [73] “Updated measurements of the inclusive w and z cross sections at 7 tev,” no. CMS-AN-10-264, 2010.
- [74] The CMS Collaboration, “Data-Driven Estimation of the Invisible Z Background to the SUSY MET Plus Jets Search,” tech. rep., 2008.
- [75] Z. Bern, G. Diana, L. J. Dixon, F. Febres Cordero, and S. e. a. Hoche, “Driving Missing Data at Next-to-Leading Order,” *arXiv*, vol. D84, p. 114002, 2011.
- [76] E. M. Laird, “A Search for Squarks and Gluinos with the CMS Detector,” 2012.
- [77] Moneta, Belasco, Cranmer et al., “The roostats project,” *Proceedings of Science*, 2010.
- [78] F. James, “MINUIT Reference Manual,” *CERN Program Library Writeup*, vol. D506.
- [79] The CMS Collaboration, “Search for Supersymmetry at the LHC in Events with Jets and Missing Transverse Energy,” *Phys. Rev. Lett.*, vol. 107, p. 221804, 2011.
- [80] The CMS Collaboration, “Search for Supersymmetry in pp Collisions at 7 TeV in Events with Jets and Missing Transverse Energy,” *Phys. Lett.*, vol. B698, pp. 196–218, 2011.
- [81] The CMS Collaboration, “Search for new physics with jets and missing transverse

- momentum in pp collisions at $\sqrt{s} = 7$ tev,” *JHEP*, vol. 08, p. 155, 2011.
- [82] The CMS Collaboration, “Inclusive search for squarks and gluinos in pp collisions at $\sqrt{s} = 7$ tev,” *Phys. Rev. D*, vol. 85, p. 012004, 2012.
- [83] The CMS Collaboration, “Search for supersymmetry in events with b jets and missing transverse momentum at the LHC,” *JHEP*, vol. 07, p. 113, 2011.
- [84] The ATLAS Collaboration, “Search for squarks and gluinos using final states with jets and missing transverse momentum with the atlas detector in proton-proton collisions,” *Phys. Lett. B*, vol. 710, p. 67, 2012.
- [85] The ATLAS Collaboration, “Search for new phenomena in final states with large jet multiplicities and missing transverse momentum using $\sqrt{s} = 7$ tev pp collisions with the atlas detector,” *JHEP*, vol. 11, p. 099, 2011.
- [86] The ATLAS Collaboration, “Search for scalar bottom quark pair production with the atlas detector in pp collisions at $\sqrt{s} = 7$ tev,” *Phys. Rev. Lett.*, vol. 108, p. 181802, 2012.
- [87] The ATLAS Collaboration, “Search for squarks and gluinos using final states with jets and missing transverse momentum with the atlas detector in proton-proton collisions,” *Phys. Lett. B*, vol. 701, p. 186, 2011.
- [88] The D0 Collaboration, “Search for squarks and gluinos in events with jets and missing transverse energy using 2.1 fb^{-1} of $p\bar{p}$ collision data at $\sqrt{s} = 1.96 \text{ tev}$,” *Phys. Lett.*, vol. B 660, p. 449, 2008.
- [89] The CDF Collaboration, “The cdf exclusion region in the $m_{1/2}$ vs. m_0 plane,” *Phys. Rev. Lett.*, vol. 102, p. 121801, 2009.
- [90] LEPSUSYWG, “Joint SUSY Working Group,” *LEPSUSYWG/02-06-2*.
<http://lepsusy.web.cern.ch/lepsusy>.
- [91] The UA1 Collaboration, “Events with large missing transverse energy at the cern collider 3: Mass limits on supersymmetric particles,” *Phys. Lett.*, vol. B 198, p. 261, 1987.
- [92] The UA2 Collaboration, “Search for exotic processes at the cern $p\bar{p}$ collider,” *Phys. Lett.*, vol. B 195, p. 613, 1987.
- [93] The CMS collaboration, “Fast simulation of the cms detector,” *Journal of Physics:*

- Conference Series*, vol. 219, no. 3, p. 032053, 2010.
- [94] The CMS Collaboration, “Validation and Tuning of the CMS Full Simulation,” *Journal of Physics: Conference Series*, vol. 331, no. 3, p. 032015, 2011.
- [95] M, Botje et al., “The PDF4LHC Working Group Interim Recommendations,” *arXiv.org*, vol. hep-ph, 2011.
- [96] D. Stump, J. Huston, J. Pumplin, W.-K. Tung, and H. e. a. Lai, “Inclusive jet production, parton distributions, and the search for new physics,” *JHEP*, vol. 0310, p. 046, 2003.
- [97] M. Ubiali et al, “Combined PDF and strong coupling uncertainties at the LHC with NNPDF2.0,” 2010.
- [98] B. C. Allanach, “SOFTSUSY: a program for calculating supersymmetric spectra,” *Comput. Phys. Commun.*, vol. 143, p. 305, 2002.
- [99] T. Sjöstrand, S. Mrenna and P. Z. Skands, “PYTHIA 6.4 Physics and Manual,” *JHEP*, vol. 05, p. 026, 2006.
- [100] W. Beenakker et al., “Squark and gluino production at hadron colliders,” *Nucl. Phys. B*, vol. 492, p. 51, 1997.
- [101] K. Nakamura, “Review of particle physics,” *J. Phys. G*, vol. 37, p. 075021, 2010.
- [102] M, Kramer et al, “Supersymmetry production cross sections in pp collisions at $\sqrt{s} = 7$ TeV,” *arXiv*.